6-30-2022

Novel Materials and Devices for Terahertz Detection and Emission for Sensing, Imaging and Communication

Naznin Akter
Florida International University, nakte001@fiu.edu

FLORIDA INTERNATIONAL UNIVERSITY

Miami, Florida

NOVEL MATERIALS AND DEVICES FOR TERAHERTZ DETECTION AND EMISSION FOR SENSING, IMAGING AND COMMUNICATION

A dissertation submitted in partial fulfillment of

the requirements for the degree of

DOCTOR OF PHILOSOPHY

in

ELECTRICAL AND COMPUTER ENGINEERING

by

Naznin Akter

2022

To: Dean John L. Volakis
College of Engineering and Computing

This dissertation, written by Naznin Akter, and entitled Novel Materials and Devices for Terahertz Detection and Emission for Sensing, Imaging and Communication, having been approved with respect to style and intellectual content, is referred to you for judgment.

We have read this dissertation and recommend that it be approved.

_____
Shekhar Bhansali

_____
Jean H. Andrian

_____
Jessica Ramella-Roman

_____
Chunlei Wang, Co-Major Professor

_____
Nezih Pala, Co-Major Professor

Date of Defense: June 30, 2022

The dissertation of Naznin Akter is approved.

_____
Dean John L. Volakis
College of Engineering and Computing

_____
Andrés G. Gil
Vice President for Research and Economic Development
and Dean of the University Graduate School

Florida International University, 2022

DEDICATION

To my husband (Dr. Siddiquee), my parents, my two elder brothers (Mohammad Badsha & Mohammad Rabiul Hossain), my niece (Inaya Zafrin), and nephew (Izayan Al Arsh).

ACKNOWLEDGMENTS

I am grateful to my supervisor, Nezih Pala, for his superb supervision and assistance. His knowledge and competence in the field of device technology enriched my graduation experience significantly. I would want to express my gratitude for his excellent assistance and mentorship. I also appreciate his support and encouragement in helping me enhance my research skills and attitude.

I would like to express my gratitude to the members of my dissertation committee, Dr. Shekhar Bhansali, Dr. Jean H. Andrian, Dr. Jessica Ramella-Roman, and Dr. Chunlei Wang, for agreeing to serve on my committee and for their substantial contributions to my dissertation research.

I would want to use this occasion to express my gratitude to all members of the INSYST Lab, especially Mustafa Abi, Steward from AMERI cleanroom and our collaborators, Dr. Shur and Yuhui Zhang, for their advice and guidance.

I am thankful to my parents, especially my mother, who is a constant source of inspiration and role model for me. I am grateful to my two elder brothers (Mohammad Badsha & Mohammad Rabiul Hossain), my sisters-in-laws (Farzana Akter Nizu & Sharmin Moushomi), my niece (Inaya Zafrin) and nephew (Izayan Al Arsh), and my in-laws for the encouragement and constant supports.

I want to express my deep love and gratitude to my husband, Dr. Masudur R. Siddiquee for his unwavering support and companionship throughout the years.

ABSTRACT OF THE DISSERTATION

NOVEL MATERIALS AND DEVICES FOR TERAHERTZ DETECTION AND EMISSION FOR SENSING, IMAGING AND COMMUNICATION

by

Naznin Akter

Florida International University, 2022

Miami, Florida

Professor Nezih Pala, Co-Major Professor

Professor Chunlei Wang, Co-Major Professor

Technical advancement is required to attain a high data transmission rate, which entails expanding beyond the currently available bandwidth and establishing a new standard for the highest data rates, which mandates a higher frequency range and larger bandwidth. The THz spectrum (0.1-10 THz) has been considered as an emerging next frontier for the future 5G and beyond technology. THz frequencies also offer unique characteristics, such as penetrating most dielectric materials like fabric, plastic, and leather, making them appealing for imaging and sensing applications. Therefore, employing a high-power room temperature, tunable THz emitters, and a high responsivity THz detector is essential.

Dyakonov-theory Shur's was applied in this dissertation to achieve tunable THz detection and emission by plasma waves in high carrier density channels of field-effect devices. The first major contribution of this dissertation is developing graphene-based THz plasmonics detector with high responsivity. An upside-down free-standing graphene in a field effect transistor based resonant room temperature THz detector device with significantly improved mobility and gate control has been presented. The highest

achieved responsivity is ~3.1kV/W, which is more than 10 times higher than any THz detector reported till now. The active region is predominantly single-layer graphene with multi-grains, even though the fabricated graphene THz detector has the highest responsivity. The challenges encountered during the fabrication and measurement of the graphene-based detector have been described, along with a strategy to overcome them while preserving high graphene mobility. In our new design, a monolayer of hBN underneath the graphene layer has been deposited to increase the mobility and electron concentration rate further.

We also investigated the diamond-based FETs for their potential characteristics as a THz emitters and detectors. Diamond's wide bandgap, high breakdown field, and high thermal conductivity attributes make it a potential semiconductor material for high voltage, high power, and high-temperature operation. Diamond is a good choice for THz and sub-THz applications because of its high optical phonon scattering and high momentum relaxation time. Numerical and analytical studies of diamond materials, including p-diamond and n-diamond materials, are presented, indicating their effectiveness as a prospective contender for high temperature and high power-based terahertz applications

These detectors are expected to be a strong competitor for future THz on-chip applications due to their high sensitivity, low noise, tunability, compact size, mobility, faster response time, room temperature operation, and lower cost. Furthermore, when plasma wave instabilities are induced with the proper biasing, the same devices can be employed as THz emitters, which are expected to have a higher emission power.

TABLE OF CONTENTS

CHAPTER ……. PAGE

CHAPTER 1 INTRODUCTION TO TERAHERTZ TECHNOLOGIES 1
1.1 Introduction 1
1.2 Motivation 4
1.2.1 State-of-art Terahertz Detectors 4
1.2.2 State-of-art Terahertz Sources 7
1.3 Contribution of this Dissertation 8

CHAPTER 2 THEORETICAL BACKGRAOUND AND NUMERICAL ANALYSIS . 11
2.1 Introduction 11
2.2 Plasma waves in Field-effect transistor (FET) 11
2.3 Terahertz detection mechanism in Field-effect transistor (FET) 14
2.4 Numerical Methods 17
2.4.1 Finite-Difference Time-Domain (FDTD) Method 17
2.4.2 Finite Element Method (FEM) 18

CHAPTER 3 GRAPHENE TERAHERTZ DETECTOR 19
3.1 Introduction 19
3.2 Graphene and its role in Terahertz Detection 19
3.3 Hexagonal Boron Nitride (h-BN) 21
3.4 Novel Broadband Antenna 21
3.1 Experimental Design 22
3.1.1 Device Design: 22
3.1.2 Fabrication Recipes: 23
3.2 Device Characterization Results and Discussion 24
3.2.1 Electrical Characterization: 24
3.2.2 Optical Characterization: 25
3.2.3 Material Characterization: 27
3.3 Conclusion 28

CHAPTER 4 DIAMOND TERAHETZ DETECTOR 30

4.1 Introduction 30
4.2 Diamond as a candidate of terahertz detection 30
4.3 Numerical Analysis 31
4.3.1 Terahertz detector response without viscosity 33
4.3.2 Terahertz detector response with temperature dependent viscosity 35
4.4 Materials and Methods 38
4.5 Results and Discussion 40
4.6 Conclusion 44

CHAPTER 5 AI POWERED TERAHERTZ VLSI TESTING TECHNOLOGY 45
5.1 Introduction 45
5.2 Related Works 46
5.3 Terahertz experimental setup for image scanning 49
5.4 Data Augmentation for Image Data Processing 52
5.4.1 Multiplication by Trigonometric function 52
5.4.2 Random noise creation 53
5.4.3 Rotation 54
5.4.4 Flip 54
5.4.5 Resize 54
5.5 Convolution Neural Network 54
5.6 Transfer Learning Model 56
5.7 Results and Discussion 56
5.8 Conclusion 61

CHAPTER 6 TERAHERTZ METAMATERIALS AND FREQUENCY SELECTIVE SURFACE 63
6.1 Introduction 63
6.2 Toroidal Dipole and related works of Toroidal Response in Terahertz range ... 65
6.3 Materials and Methods for Hybrid Toroidal Resonance Response in Planar Core-Shell Structure 66
6.4 Results and Discussion for Hybrid Toroidal Resonance Response in Planar Core-Shell Terahertz Metasurfaces 67
6.5 Toroidal Hybridization Concepts of the Proposed Planar Core-Shell Terahertz Metasurfaces 70

6.6 Frequency selective surface-based Terahertz bandpass filter 73
6.7 Materials and Methods for Terahertz bandpass filter..... 74
6.8 Results and Discussion for Terahertz bandpass filter 76
6.9 Conclusion..... 79

CHAPTER 7 FUTURE DIRECTIONS 81

References 82

VITA 110

LIST OF TABLES

TABLE	….	PAGE
Table 1.1	State-of-the-art THz detectors	4
Table 1.2	State-of-the-art THz sources	7
Table 4.1	Material parameters for p-Diamond	39
Table 4.2	Material parameters for n-Diamond	39
Table 5.1	General description of the used CNN and transfer learning models	57
Table 5.2	Overall comparison of each deep leaning model's performance.	60
Table 6.1	Terahertz bandpass filter parameters	76

LIST OF FIGURES

FIGURE	….....	PAGE
Figure 1.1	The electromagnetic frequency spectrum represents the terahertz range.	1
Figure 1.2	The bandwidth versus distance curve represents the state-of-the-art THz detectors and targeted detectors.	6
Figure 2.1	Schematic representation of the plasma waves in different regimes.	15
Figure 3.1	(a) Schematic of graphene and h-BN heterostructure field effect transistor and (b) SEM image showing the suspended and unsuspended graphene.	23
Figure 3.2	I-V Characteristics (a) Drain current as a function of source-drain voltage. (b) Drain current as a function of gate voltage.	25
Figure 3.3	Temperature dependent responsivity of grating gate devices.	26
Figure 3.4	(a) Responsivity of dual grating gate device at room temperature and (b) Temperature dependent responsivity response at different frequencies.	26
Figure 3.5	(a) Responsivity (V=R=(x2+y2)1/2 of signal) as a function of channel current at different frequencies. (b) Responsivity and channel current as a function of channel voltage at 368.8 GHz resonant mode.	27
Figure 3.6	Raman measurements for the same at different reference point (a) Ratio of 2D/G<1.6 confirms multilayer graphene presence and (b) Ratio of 2D/G>1.6 confirms monolayer graphene presence.	28
Figure 4.1	Schematic of diamond FET.	38
Figure 4.2	(a) p- and (b) n-diamond without viscosity effect for 50nm gate as a function of temperature.	40
Figure 4.3	(a) p- and (b) n-diamond with viscosity effect for 50nm gate as a function of temperature.	41
Figure 4.4	Comparison between with viscosity and without viscosity for (a) p- and (b) n-diamond as a function of gate length at 300K temperature.	41
Figure 4.5	Comparison of viscosity and without viscosity effect of (a) p- and (b) n-diamond for 50nm gate.	42

Figure 4.6	High temperature (300K, 500K and 800K) response of p- and n-diamond FET detector.	43
Figure 5.1	Experimental setup for terahertz IC scanning (a) Experimental setup using a IMPATT diode as a terahertz source. (b) Schematic presentation of the terahertz scanning setup using a Virginia Diodes 0.3-THz source for generating spatial terahertz response map for AI based image processing.	49
Figure 5.2	Position dependent DC response at a selected pin of the tested IC while a THz beam was swept in 2D for undamaged samples.	51
Figure 5.3	Position dependent DC response at a selected pin of the tested IC while a THz beam was swept in 2D for damaged samples.	51
Figure 5.4	Algorithm for data augmentation. (a)Algorithm 1, (a) Algorithm 2, and (a)Algorithm 3 labelled as Secure Image dataset and (d) Algorithm 4 labelled as Unsecure Image dataset.	53
Figure 5.5	Basic framework of Transfer learning model.	55
Figure 5.6	Training progress chart for (a) CNN, (b) Alex Net, (c) VGG16, (d) VGG19, (e) ResNet50, (f) ResNet10, (g) GoogLeNet, and (h) MobileNet-v2.	58
Figure 5.7	Confusion Matrix for (a) CNN, (b) Alex Net, (c) VGG16, (d) VGG19, (e) ResNet50, (f) ResNet10, (g) GoogLeNet, and (h) MobileNet-v2.	59
Figure 6.1	(a) Schematic representation with specified geometrical parameters, (b) 3D rendering view with the polarization of the incident THz beam (m—showing the direction of magnetic moment; E & H—electric and magnetic field of incident THz beam; and T—toroidal moment), and (c) SEM image of toroidal metamolecule.	66
Figure 6.2	(a) Simulated and experimental transmission versus frequency spectra, (b) vectorial B field, and (c) surface current distribution (j) for core at 0.259 THz. (d) Simulated and experimental transmission versus frequency spectra, (e) vectorial B field, and (f) surface current distribution (j) for shell at 0.212 THz. The red arrows in (c) and (f) show the direction of the current (j) in the center strip of the resonators.	68
Figure 6.3	(a) Simulated and experimental transmission versus frequency spectra for core-shell, (b) vectorial B field, and (c) surface current distribution (j) for core-shell at 0.202 THz, and (d) vectorial B field, and (e) surface current distribution (j) for core-shell at 0.308 THz	70

Figure. 6.4 (a) Experimental transmission spectra for core-shell, core, and shell structures and (b) an energy level diagram, describing the interaction between the core and shell plasmon resonances based on the surface current distribution, resulting in the hybrid plasmon resonance of a concentric core-shell nanomatryoshka structure. 71

Figure 6.5 Schematic representation of the (a) unit cell of the THz bandpass filter structure and specified geometrical parameters and (b) Transmission spectrum of the proposed filter structure from 100 to 1000 GHz based on the periodicity P=420μm, 390μm, 360μm, 330μm, 300μm, 270μm, 240μm, 210μm, 180μm, 150μm, 120μm, 90μm and 60μm. 75

Figure 6.6 Transmission spectrum of the proposed filter structure from 100 to 3000 GHz based on the periodicity P=420μm, 390μm, 360μm, 330μm, 300μm, 270μm, 240μm, 210μm, 180μm, 150μm, 120μm, 90μm, 60μm and 30 μm (a) without embedded au nanoparticles and (b) with embedded au nanoparticles. 77

LIST OF ACRONYMS AND ABBREVIATIONS

THz	Terahertz
GHz	Gigahertz
Hz	Hertz
WiFi	Wireless Fidelity
Tbps	Tera bit per second
CISCO	Commercial & Industrial Security Corporation
FET	Field Effect Transistor
TeraFET	Terhertz Field Effect Transistor
NEP	Noise Equivalent Power
CMOS	Complementary Metal Oxide Semiconductor
MOSFET	Metal Oxide Semiconductor Field Effect Transistor
FinFET	Fin-shaped Field-Effect Transistor
HEMT	High Electron Mobility Transistor
SNR	Signal to Noise Ratio
BW	Bandwidth
CW	Continuous Wave
h-BN	Hexagonal Boron Nitride
IC	Integrated Circuit
MMIC	Monolithic Microwave Integrated Circuits
VLSI	Very Large Scale Integration

ULSI	Ultra Large-Scale Integration
2DEG	2 Dimensional Electron Gas
FDTD	Finite Difference Time Domain Finite
FEM	Element Method
mid-IR	mid-Infrared
EBL	Electron Beam Lithography
EBE	Electron Beam Evaporation
ALD	Atomic Layer Deposition
SPA	Semiconductor Parameter Analyzer
BWO	Backward Wave Oscillator
TDS	Time Domain Spectrometer
GaN	Gallium Nitride
SAM	Scanning Acoustic Microscopy
SAW	Surface Acoustic wave
LTEM	Laser Terahertz-Emission Microscope
EOS	Electrical Overstress
ESD	Electrostatic Discharge Convolutional
CNN	Neural Network Alternating Current
AC	Direct Current
DC	Perfectly Matching Layer
PML	

SEM	Scanning Electron Microscope
FSS	Frequency Selective Surface
EM	Electromagnetic Wave
PDMS	poly(dimethylsiloxane)
PEDOT: PSS	poly (3,4-ethylene dioxythiophene) polystyrene sulfonate
HDPE	High-Density PolyEthylene
PET	PolyEthylene Terephthalate
FWHM	Full Width Half Maximum

CHAPTER 1 INTRODUCTION TO TERAHERTZ TECHNOLOGIES

1.1 Introduction

The terahertz (10^{12} Hz) frequency range extends around 100 GHz to 10 THz, which is in between the infrared and microwave regions in the electromagnetic spectrum. Terahertz technology could be used in various applications, including communication, imaging, and sensing [1]. Figure 1.1 illustrates the electromagnetic spectrum of Terahertz frequencies.

Terahertz frequency has minimal energy and is insufficient to ionize or disrupt the bonds of biological tissues [2]. Terahertz radiation can pass through soft materials like paper, cloth, plastic, and leather but not metal or the human body, making them ideal for security screening for hidden weapons and hardware cybersecurity. The Terahertz spectrum has a resolution advantage over millimeter waves in security monitoring, which is limited by the imaging wavelength. The wavelengths of terahertz frequencies range from tens to hundreds of microns, providing for higher resolution. THz frequencies

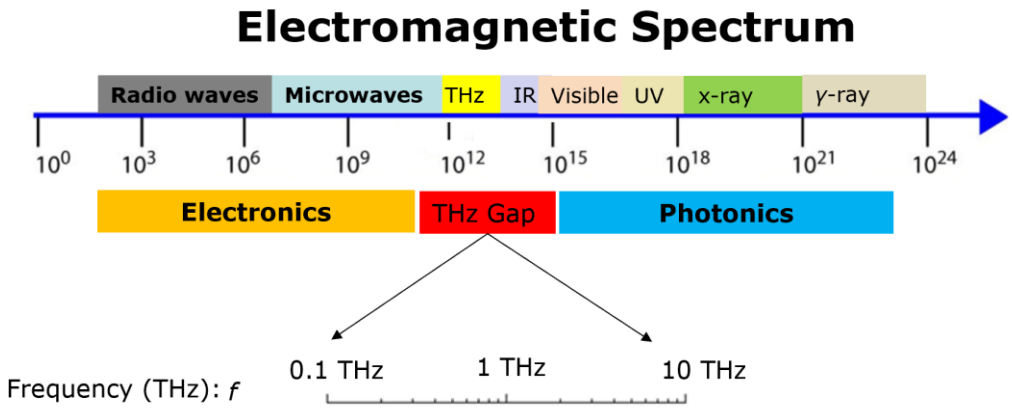

Figure 1.1 The electromagnetic frequency spectrum represents the terahertz range.

resemble the energy levels of DNA [3], protein [4], other organic molecules, and explosives [5]. These could yield unique fingerprints for identifying biological tissues in a spectrum region that hasn't been studied for medical uses before or detect and identify trace amounts of explosives. The terahertz wavelength is sensitive to hydration state [6] and can display tissue conditions because of their sensitivity to water and show absorption peaks. THz radiation has also been employed in the testing and failure analysis of VLSI circuits [7], [8] and to characterize semiconductor materials [6], [9], [10]. With the promise of improving network speed by up to 100 times and minimizing latency by a factor of 20, the emerging 5G and beyond (6G) WiFi technology will open plenty of new possibilities. Virtual reality for remote surgeries, intense high-resolution video communications, and connecting a considerably higher number of devices, such as sensors for the Internet of Things, are only a few of these uses [11]. Compared to nearby frequency bands, the 0.1–10 THz range has been suggested to be the most favorable for achieving Terabit per second (Tbps) data rates, especially for compact transceivers [12]. With the initial applications for transmission from a fiber to a curb, the millimeter-wave and photonics communities have already begun to explore the next frontier, going from 28 GHz 5G communications to the 240–320 GHz spectrum with a window for THz absorption in the atmosphere [13]. The atmospheric window between 500 and 600 GHz also is worth noting. Due to rising demand, the upper THz band (1–10 THz) is projected to be dedicated to indoor wireless communication networks soon [14]. Data traveling next few years, anticipated by CISCO Systems to move from 22 Exabytes in 2019 to around 50 in 2021 [15], [16], demonstrates the necessity for a greater communication frequency and broader bandwidth addressed by expanding beyond 5G.

THz spectrum can enable Terbit per second (Tbps) communication over large distances, from thousands of miles in space to submicron on semiconductors. In addition to its immense potential, Terahertz radiation faces several challenges, including signal strength loss due to atmospheric absorption/penetration and substantial path loss. The fundamental problem with employing THz frequency bands for wireless communications is the lack of devices for generating and detecting them. Innovative solutions are required to overcome these devices and communication problems [12], [17]. THz spectrum can enable Terbit per second (Tbps) communication over large distances, from thousands of miles in space to submicron on semiconductors.

In addition to its immense potential, Terahertz radiation faces several challenges, including signal strength loss due to atmospheric absorption/penetration and substantial path loss. The fundamental problem with employing THz frequency bands for wireless communications is the lack of devices for generating and detecting them. Innovative solutions are required to overcome these devices and communication problems [12], [17]. Small and high output power sources and high-responsivity/low-noise detectors working in the THz region are required to overcome the significant path loss at these frequencies. Tbps data rates in wireless communication beyond 5G are enabled by such devices, spanning the infamous "THz-gap" and enabling new THz technologies, including THz security, medical imaging, and high-resolution automobile radar for autonomous driving. THz communication technology will be essential in the post-COVID19 pandemic due to the significant growth in internet applications.

1.2 Motivation

1.2.1 State-of-art Terahertz Detectors

Table 1.1 State-of-the-art THz Detectors

Material and device type	Responsivity (V/W)	NEP ($pW/Hz^{1/2}$)	Operation Temperature	Frequency (THz)	Modes	Ref
GaN/AlGaN HFETs (or HEMTs)	15000	25-31	RT	0.49-0.65	Broadband	[18]
		0.48	RT	0.14	Broadband	[19]
GaAs HEMTs	70–80	15-1000	RT	0.24	Broadband	[20]
InP HEMTs	22700	0.48	RT	0.2	Resonant	[21]
65nm-Si CMOS	140	100	RT	0.7-1.1	Broadband	[22]
65nm-Si CMOS	2200	14	RT	0.724	Resonant	[23]
150nm-Si CMOS	350, 50, 5	42, 487	295K	0.595, 2.9, 4.1	Resonant	[24]
90nm-Si CMOS	75	20, 59, 63, 85, 110, 404	RT	0.59, 0.216, 2.52, 3.11, 4.25, 4.75	Resonant	[25], [26]
90nm-Si CMOS	220	48-70	RT	0.6-1.5	Broadband	[27]
Si MOSFET (single pixel)	19000	535	RT	0.2	Broadband	[28]
10 × 10 Si CMOS FPA	16400	216×10^3	RT	0.2	Broadband	[28]
Graphene FETs	14	515	300K	0.6	Broadband	[29]
	0.01	3×10^4, 2×10^5		0.3		
Black phosphorous FETs	0.15	40000	RT	0.298		[30]
MoS2	2[a]		RT	2.52		[31]

Short channel FETs (also known as TeraFETs) that enable decaying or resonant plasma waves have the potential to extend high-frequency electronics into the THz spectrum by generating efficient THz and sub-THz detectors and generators [32]. TeraFET detectors can operate in the 0.1 THz to 22 THz range [33] with Noise Equivalent Power (NEP) as low as 0.5 $pW/Hz^{1/2}$ [34] based on silicon complementary metal-oxide semiconductor (CMOS) FETs [35], Si FinFET [36], Silicon-on-Insulator MOSFETs [37], InGaAs HEMTs [38], AlGaN/GaN HEMTs [39], and graphene [40]. P-diamond has recently been shown to have advantages in the development of TeraFETs

operating in the 240 GHz to 320 GHz range for functioning beyond 5G WIFI [41]. THz detectors with high responsivity, selectivity, and broad bandwidth, as well as small and efficient THz sources, are required for THz technology for sensing, imaging, and communications.

The plasma wave electronics detectors based on various material systems have shown exceptional performance, with responsivities in the 10 kV/W range and NEP in the sub-pW/$Hz^{1/2}$ range. Plasma wave electronics detectors have the advantage of being tunable by bias voltage and modulable at extremely high frequencies (up to 200 GHz) [42]. Plasma wave electronics detectors can be tunable by bias voltage and modulated at extremely high frequencies (up to 200 GHz and beyond) [42].

Responsivity and sensitivity are two typical figures of merit used to evaluate a detector's performance. The detector response voltage or current ratio to the incident THz signal power is the responsivity of a detector, and it indicates how strongly a detector can respond to a THz signal. The noise equivalent power (NEP), which is typically used to characterize sensitivity, is a measurement of a detector's ability to discriminate a weak signal from background noise. It is defined as the smallest detectable signal strength required to produce unity in the signal-to-noise ratio (SNR=1) within a 1 Hz bandwidth. Another crucial parameter is the response time, which indicates how quickly a detector can react to a THz signal.

Submicron FETs based on plasma wave propagation could operate in the plasma mode with frequencies orders of magnitude higher than the cut-off frequency for the transit-time limited operation regime [43], due to the faster plasma wave velocity (on the order of 10^8 cm/s) than the carrier drift velocity. Dyakonov and Shur proposed and

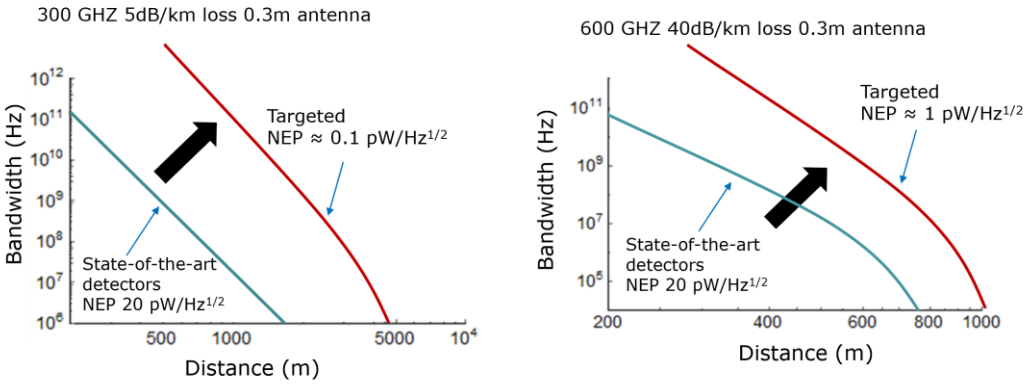

Figure 1.2. The bandwidth versus distance curve represents the state-of-the-art THz detectors and targeted detectors [46].

developed THz radiation detection using nonlinear features of the plasma wave created in the channel [43]–[45]. THz plasmonic devices have the potential to enhance NEP of the detectors. Figure 1.2 represents [46] the bandwidth versus distance curve of the state-of-the-art THz detectors and targeted detectors. For the next generation terahertz detector, the targeted NEP is 0.1 pW/Hz$^{1/2}$. The relationship between the bandwidth and the NEP can be expressed in terms of signal-to-noise ratio (SNR) and Friis Transmission [47],

$$BW = \frac{P_r^2}{SN^2NEP^2}$$

$$P_r = \frac{c^2 G_r G_t P_t}{A(4\pi R f)^2}$$

Where, c is the speed of light, Gr is the rceiving antenna gain, G_t is the transmitting antenna gain, A is the propagation loss, R is the communication distance, and f is the communication frequency.

In Table 1.1, we present a summary of the performance of plasmonic detectors recently published in the literature.

1.2.2 State-of-art Terahertz Sources

Table 1.2 State-of-the-art THz Sources

Emitter	Frequency Range (THz)	Power (W)	Temp	Condition	Ref
Gunn diode devices	0.3-0.4	10^{-2}	RT	Tunable- Small/medium	[48]
Resonant Tunneling Diodes (RTD)	0.1-1	7×10^{-4}-7×10^{-7}	RT	Not tunable	[49], [50]
Backward wave oscillator (BWO)	0.341-0.351	1	RT	Tabletop	[51]
Gas Laser	0.5-5	1×10^{-3} - 30×10^{-3}	RT	Discrete Lines- Table Top	
Quantum Cascade laser	1.2-5.9 2.06-4.35	2.87×10^{-4} 4.2×10^{-6}	110K RT	Tunable- Small	[52], [53]
Optical parameter conversion	0.5-5	50×10^{3}	RT	Tunable- Bulky	[54]
Optical rectification	1.5	~7.4×10^{-9} and ~3.6×10^{-9}	RT	Tunable- Bulky	[55]
Plasma radiation	0.1-5	700×10^{3}	RT	Tunable- Bulky	
Coherent radiation	0.5-5	7.5×10^{6}	RT	Tunable- Bulky	
Gyrotron	0.1-2.5	700×10^{3}	RT	Tunable- Bulky	
Free electron lasers	0.5-5	10^{6}	RT	Tunable- Bulky	
Frequency multiplication devices	0.7-1.1	0.016	RT	Tunable- Small	[56]
Difference frequency generation using 2 MIR QCLs	3.5-5	0.0019-10^{-9}	RT	Tunable- Small	

THz generation can be divided into two categories: optical and electrical. Heterodyne photomixers, optical parametric converters, gas lasers, free-electron lasers, and other optical technologies are often large, complex, high power, and expensive. It is commonly acknowledged that pure photonic sources and detectors will not be the preferred technology for next-generation terahertz communications [57].

Solid state sources in the THz range [58] are challenging to fabricate because the size is so small that the power available is so low. The efficiency of the sources decreases dramatically as the THz range increases [59] in comparison to microwave frequency transmissions, the carrier travel time becomes extremely short. Despite showing outstanding performance, charge transfer limits THz sources based on electronic technologies like CMOS, SiGe BiCMOS, and field effect transistors of III-V materials (e.g. GaN, InP), requiring the use of multipliers to reach even lower THz bands. Furthermore, because their output power diminishes quickly with the square of the frequency, they are ineffective of compensating for large attenuation in the ambient environment. Except for resonant tunneling diodes, which oscillate at roughly 700 GHz, there is currently no single electrical device capable of oscillating in the 1–10 THz bandwidth. Gunn diodes and IMPATT diodes are active microwave and millimeter-wave devices that cannot operate at frequencies higher than 400–500 GHz [60]. A summary of current terahertz sources is shown in table 1.2, demonstrating the critical need for research into miniaturized CW terahertz sources that operate at room temperature and deliver a few mW outputs powers.

1.3 Contribution of this Dissertation

This study investigates novel materials, such as graphene and diamond, with the potential for compact and high output power terahertz emitters, as well as high-sensitivity and low-noise detectors, using the less explored but promising approach of plasma wave oscillations based Dyakonov-Shur theories and models in high carrier-density material systems.

The novelties of this dissertation work are listed below:

I. We designed, developed, fabricated, and analyzed graphene-based FET detector with a high responsivity. We have designed and fabricated several multi-size and multi-geometry detectors using a stack of monolayer graphene on top of hexagonal boron nitride (h-BN) and experimentally showed frequency dependent terahertz detection. These detectors are compact, tunable, can operate at room temperature with a high responsivity.

II. We have implemented both simulated and analytical approach of solving the hydrodynamic equation using temperature dependent viscosity response for diamond materials. We have investigated n-diamond materials along with p-diamond. And we have also shown the high temperatures (300K, 500K and 800K) response of both p-diamond and n-diamond materials.

III. We have implemented a novel terahertz response-based introduce a new terahertz testing method for non-destructive and unobtrusive identification of counterfeit, damaged, forged or defective monolithic microwave integrated circuits (MMICs), Very Large Scale Integration (VLSI) and Ultra large-scale integration (ULSI) circuits by measuring their response to incident terahertz and sub-terahertz radiation at the circuit pins and analyzing the response using the deep learning convolution neural network techniques. This work is highly important to ensure the hardware-based cybersecurity.

Additionally, we have shown a planar nanomatryoshka type core-shell resonator exhibiting hybrid toroidal resonance modes at THz frequencies, both physically and

numerically. The relevance of our research lies in the identification of unique characteristics as a result of the development of hybrid toroidal moments in a spatially limited planar core-shell structure. We have also shown a frequency selective surface-based tunable and stretchable terahertz bandpass filter structure. Both structures have the potential to expand the range of applications for advanced THz photonics, including precise bio-sensing (or immunobiosensing), quick switching, narrow-band filters and modulation, diagnostic tools, and so on.

CHAPTER 2 THEORETICAL BACKGRAOUND AND NUMERICAL ANALYSIS

2.1 Introduction

Plasma waves can be resonated in the channel of a field-effect transistor (FET). The plasma frequency of this resonator is specified by its dimensions, and it can reach the terahertz (THz) range for gate lengths of a micron and sub-micron (nanometer) scale. In the early 1990s [61], Dyakonov and Shur suggested the concept of employing field-effect transistors (FETs) for THz applications. According to their theoretical work, a steady current flow in an asymmetric FET channel can induce instabilities against the spontaneous formation of plasma waves (electron density oscillations in space and time). The emission of electromagnetic radiation at the plasma wave frequency can be caused by these instabilities, now known as Dyakonov-Shur (DS). They later demonstrated that THz radiation could be detected and mixed using the nonlinear features of 2D plasma in FET channels [62].

2.2 Plasma waves in Field-effect transistor (FET)

Plasma waves are oscillations of the electron density in time and space, with attributes controlled by the electron density and the size and geometry of the electronic system. The In the three-dimensional system, plasma oscillation frequency is nearly independent of wavelength whereas, in a gated two-dimensional electron gas (2DEG), plasma waves follow a linear dispersion equation comparable to light in vacuum, sound waves, or shallow water waves. The gate bias can easily control the plasma wave velocity, s, and is determined by the square root of the electron sheet density.

Here, a general overview of plasma waves will be presented, followed by an investigation of THz detection in various modalities, considering a low-dimensional structure with a FET channel and the frequency constraints that limits plasma modes. It is feasible to determine the dispersion relations for plasma waves in systems of various dimensions using the average drift velocity, v, and ignoring collisions. The small signal equation of motion and the continuity equation are neglected in this case.

$$\frac{\partial \mathbf{j}}{\partial t} = \mathbf{E}\frac{e^2 n}{m} \qquad \text{Eq. 2-1}$$

$$\frac{\partial \rho}{\partial t} + \nabla . \mathbf{j} = 0 \qquad \text{Eq. 2-2}$$

Here, current density, **j**=env. Where, e is the electron charge, n is the electron density, m is the electronic effective mass, and ρ is a small-signal charge density related to a deviation of n from its equilibrium value, E is the small signal electric field. Differentiating Eq. 1-2 with respect to time and using Eq. 2-1, we have,

$$\frac{\partial^2 \rho}{\partial t^2} + \frac{e^2 n}{m}\nabla \cdot \mathbf{E} = 0 \qquad \text{Eq. 2-3}$$

These equations hold true regardless of the problem's dimensionality. In the 3D scenario, the j, n, and ρ are current per unit area, electron concentration, and electric charge per unit volume, respectively satisfying the relation

$$\nabla \cdot \mathbf{E} = \rho/\varepsilon \qquad \text{Eq. 2-4}$$

where ε is the dielectric constant of the material. When Eq. 2-4 is substituted for Eq. 2-3, a harmonic oscillator equation for the charge density with the bulk plasma frequency is obtained.

$$\omega_p = \sqrt{\frac{e^2 n}{\varepsilon m}} \qquad \text{Eq. 2-5}$$

The electric field vector, E, in Eq. 2-1 and Eq. 2-3 should be interpreted as the in-plane electric field having only two components, Ex and Ey, for the 2D case, which represents the channel of a FET. The third component of the electric field (which is perpendicular to the plane, xy, of the 2DEG) does not contribute to the in-plane current.

The relationship between electron concentration and electric potential for a gated two-dimensional electron gas (i.e., an FET) is given by

$$\rho = en = CU \qquad \text{Eq. 2-6}$$

where $U = U_g - U_c - U_T = U_{gc} - U_T$, U_T is the threshold voltage, $U_{gc} = U_g - U_c$ is the potential difference between gate and channel, $C = \varepsilon / d$ is the gate-to-channel capacitance per unit area, and d is the gate-to-channel separation. This equation holds when the gradual channel approximation is valid and U moves along the channel on a scale larger than d. Hence, the in-plane electric field is given by

$$\mathbf{E} = -\nabla U = -\frac{\nabla \rho}{C} \qquad \text{Eq. 2-7}$$

By substituting Eq. 1-7 into Eq. 1-6 we can obtain,

$$\frac{\partial^2 \rho}{\partial t^2} + s^2 \nabla^2 \rho = 0 \qquad \text{Eq. 2-8}$$

Where, plasma wave velocity, $s = \sqrt{\frac{e^2 n d}{m^* \varepsilon}}$ Eq. 2-9

The solution of Eq. 2-8 corresponds to waves having a linear dispersion law: $\omega = sk$, where ω and k are the plasma waves frequency and the wave vector, respectively. The electrons in a FET's channel are described by nonlinear hydrodynamic equations are identical to the shallow water equations in traditional hydrodynamics, as stated in Ref [61]. The phrase "shallow water" describes a condition in which the wavelength, or more

broadly, the spatial scale of fluctuation in the water level, is substantially larger than the depth h. This is comparable to supposing that the wavelength is substantially larger than the gate-to-channel spacing d, or kd <<1. In the case of short wavelengths (kd >> 1), the gate is irrelevant, which is analogous to the "ungated" scheme, and plasma waves exhibit a dispersion relation similar to that of "deep water" case:

$$\omega = \sqrt{\frac{e^2 n}{2m^* \varepsilon} k} \qquad \text{Eq. 2-10}$$

The dispersion law for plasma waves propagating along a one-dimensional wire may be obtained using the same method:

$$\omega_p = sk \sqrt{ln \frac{1}{kr}} \ , \ s = \sqrt{\frac{e^2 n}{m^* \varepsilon}} \qquad \text{Eq. 2-11}$$

where r is the radius of the wire and s is the velocity of one-dimensional plasma waves.

2.3 Terahertz detection mechanism in Field-effect transistor (FET)

In Ref [18], the concept of employing a FET to detect THz radiation was presented. The nonlinear properties of the transistor, which rectifies an AC produced by the incoming THz radiation, allow for such detection. A photoresponse is defined as a dc voltage between a source and drain proportional to the radiation power (photovoltaic effect) induced by an asymmetry between source and drain. Asymmetry can be accomplished in a variety of ways. The source and drain boundary conditions may differ due to the asymmetric design of the source and drain contact pads or external (parasitic) capacitances. A unique antenna design attached to one side of the transistor channel can be used to produce even more asymmetry. When a dc current is transmitted between the

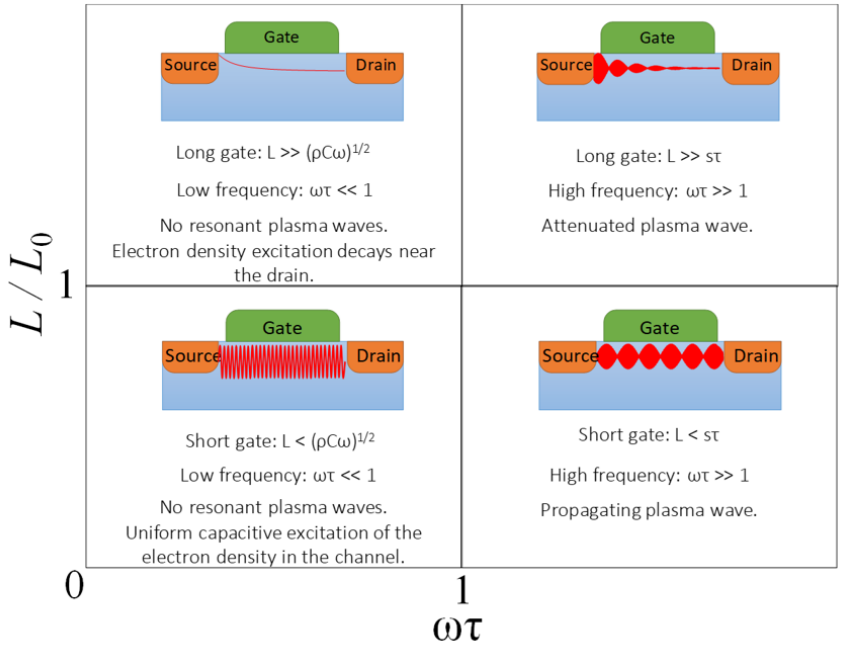

Figure 2.1: Schematic representation of the plasma waves in different regimes.

source and the drain, the electron density on the drain side of the channel is depleted, resulting in asymmetry.

In the absence of the drain current and under static circumstances, $U = U_0 = U_g - U_{th}$, where U_0 is the static voltage swing. Two operating regimes may be distinguished based on the frequency, and each of them can be further separated into two sub-regimes depending on the gate length L as shown in Figure 2.1.

1. **High frequency regime ($\omega\tau > 1$):** The conductivity in the channel, $\sigma = ne^2\tau/m$ is determined by the electron momentum relaxation time, τ, and the kinetic inductances plays an important role. The plasma waves have a velocity, $s = \sqrt{\frac{eU_0}{m}}$, a damping time τ with a propagation distance of $s\tau$.

    I. **Short gate case ($L < s\tau$):** In this case, the plasma wave reaches the drain side of the channel, gets reflected, and forms a standing wave

with enhanced amplitude, so that the channel serves as a high-quality resonator for plasma oscillations. The fundamental mode has a frequency, ~ s/L, and a numerical coefficient that varies according to the boundary conditions.

II. **Long gate case (L>>sτ):** In this case, the plasma waves generated at the source will dissipate before reaching the drain, leaving just a small fraction of the channel next to the source with an ac current.

2. **Low frequency regime (ωτ <<1):** In this case, the plasma waves cannot exist because of overdamping. The inductance becomes short-circuits at these low frequencies, resulting in an RC line. Its characteristics are also affected by the gate length, with the relevant parameter being $\omega\tau_{RC}$, where τ_{RC} is the overall transistor's RC time constant. The value of $\tau_{RC} = L^2\rho C$ can be obtained when the entire channel resistance is $L\rho/W$, and the total capacitance is CWL. Here, W is the gate width and $\rho = 1/$ is the channel resistivity.

   I. **Short gate case ($L < (\rho C\omega)^{1/2}$):** When $\omega\tau RC < 1$, the ac current is distributed evenly over the whole gate length through the gate-to-channel capacitance. This regime, also known as 'resistive mixer' regime, applies exclusively to transistors with extremely short gates at THz frequency.

   II. **Long gate case ($L >> (\rho C\omega)^{1/2}$):** When $\omega\tau_{RC} >> 1$, and the induced ac current may leak to the gate at a short distance from the source, satisfying the requirement $\omega\tau_{RC}(l) = 1$, where $\tau_{RC}(l) = R(l)C(l) = l^2\rho C$.

with the resistance R(l) and capacitance C(l) of this section of the transistor channel.

The "leakage length" l on the order of $(\rho C\omega)^{1/2} \approx s(\tau/\omega)^{1/2}$ is determined by this criterion. If l << L, there will be no ac voltage or current in the channel beyond a few distances l from the source.

2.4 Numerical Methods

2.4.1 Finite-Difference Time-Domain (FDTD) Method

The Finite-Difference Time-Domain (FDTD) algorithm is well suited because of its flexibility in discretization and matrix-free nature to simulate plasmon resonances and related nanophotonic structures and nanodevices. All spatial and temporal derivatives in Maxwell's curl equations are replaced by finite difference equations in this technique [63]. The software utilized in this thesis for FDTD calculations is FDTD Solutions, developed by LUMERICAL Inc. [64]. The structure of interest in our numerical analysis is placed in a computation window frame separated by a three-dimensional grid, and each of these cells is referred to as a Yee cell [65]. The size of these grids, x, y, and z, is chosen to be small enough that they do not differ significantly from one to the next. The time step is crucial in determining numerical analytic stability, also known as Courant stability [66], which can be described using following relation,

$$\sqrt{(\Delta x)^2 + (\Delta y)^2 + (\Delta z)^2} > c\Delta t = \sqrt{\frac{1}{\epsilon\mu}} \times \Delta t \qquad \text{Eq. 2-12}$$

2.4.2 Finite Element Method (FEM)

The Finite Element Method (FEM) is a prominent numerical analysis tool in nanophotonics that allows for precise frequency domain EM field calculations. The COMSOL Multiphysics 5.6 modeling software, produced by COMSOL Inc., is used in this thesis for FEM computations. [67]. One of the primary characteristics of the COMSOL Multiphysics® software is the flexibility to modify nearly any expression in the computational model. The mathematics interfaces provide a variety of tools for equation-based modeling and fulfilling distinct tasks, rather than modeling specific physics. ODEs, algebraic equations, other global (space-independent) equations, and curvilinear coordinates may all be added to a variety of PDE formulations using these interfaces.

For this thesis, we have used general form PDE (Eq. 2-60) and coefficient form PDE (Eq. 2-61) and week form PDE for our equation-based modeling interface.

$$e_a \frac{\delta^2 u}{\delta t^2} + d_a \frac{\delta u}{\delta t} + \nabla . \Gamma = f \qquad \text{Eq. 2-13}$$

$$e_a \frac{\delta^2 u}{\delta t^2} + d_a \frac{\delta u}{\delta t} + \nabla . (-c \nabla u - \alpha u + \gamma) + \beta . \nabla u + \alpha u = f \qquad \text{Eq. 2-14}$$

In the PDE, Boundary Elements Interface, domain and boundary feature nodes include Dirichlet Boundary Condition, Flux/Source, Initial Values, and Zero Flux.

CHAPTER 3 GRAPHENE TERAHERTZ DETECTOR

3.1 Introduction

Detecting and generating terahertz (THz) and sub-THz radiation with short-channel field-effect transistors (FETs) has shown considerable potential. According to the Dyakanov-Shur instability theory [61], when excited by impinging radiation and rectified by device nonlinearities, plasma waves could detect terahertz radiation. Terahertz detectors are critical components for the advancement of THz technologies, and choosing the proper material is vital to a robust detector design. We chose graphene [68], [69] as the material of choice for our terahertz detector because of its many benefits, including its minimal volumes, wide modulation frequency ranges (mid-IR and THz), ultrahigh speed, low energy consumption, high electron mobility, and high responsivity.

3.2 Graphene and its role in Terahertz Detection

Graphene is a one-atom-thick sheet of sp^2-hybridized carbon atoms organized in a honeycomb lattice. It was initially obtained in 2004 [70] by exfoliating graphite and has since been a popular study topic due to its appealing mechanical, thermal, and electrical characteristics [71]–[73]. The relativistic nature of graphene's quasiparticles results in unusually high electron mobility [70], which gives it its distinctive electrical and optical characteristics. Graphene has the potential to revolutionize a wide range of applications [71]–[73], including solar cells and light-emitting devices, as well as touch screens, photodetectors [73], microwave transistors [74], and ultrafast lasers [75]. The Drude-like electric response of the free carriers, and the interband transitions between the lower and

higher bands of the Dirac cone, dictate the electromagnetic characteristics of biased or photo-excited graphene. Controlling the Fermi energy allows for extraordinary tuning of electromagnetic structures formed of this material.

The structures investigated in this field section are graphene layers on high resistive silicon substrates. In a 35 nm thick Al_2O_3 layer, gold grating gates are deposited on graphene. The effect of various combinations of gate period, L, and gate finger length, W, on gate performance was examined. For plasma waves with the fundamental frequency of ω_0 and its harmonics, a short channel with high sheet carrier concentration works as a resonant cavity. In such a channel, incoming electromagnetic radiation triggers plasma waves. The resonance condition is met when $\omega_0\tau >> 1$ (τ is the momentum relaxation time). In an undoped graphene, the electron energy dispersion is linear, $E=\Delta V_F.k$, V_F is the 2D Fermi velocity ($V_F = 10^8$ cm/ s) and k is the electron momentum. In graphene, the linear electron energy spectrum means that there is no effective electron mass. In massless graphene, the electron inertia is characterized by a fictitious relativistic effective mass $m_F=E_F/V_F^2$, where E_F is the Fermi energy. In graphene with electron mobility, the electron relaxation rate is calculated as $1/\tau = e/\mu m_F$. Plasmon dispersion in a gated graphene may be described in the same way as in a traditional semiconductor structure, but with the effective electron mass replaced by the relativistic effective mass m_F.

$$\omega = q \sqrt[4]{N_s \frac{2V_f^2 e^4 d^2}{\hbar^2 \epsilon^2}} \qquad \text{Eq. 3-1}$$

where N_s is the sheet carrier concentration, d is the distance between the graphene channel and the gate metal, ϵ is the permittivity and the plasmon wavevector q is

dictated by the grating gate period L, with q=2/L (n = 1,2,3...). The ability of THz devices to operate at room temperature is critical for many applications such as medical imaging, security, and sensing.

3.3 Hexagonal Boron Nitride (h-BN)

Single-crystalline hexagonal boron nitride (h-BN) [76] shows prospect as an alternative gate dielectric. Few charged impurities exist in single-crystalline h-BN and cleaving it yields a flat surface with no dangling bonds. Furthermore, it has been demonstrated that graphene on an h-BN substrate has much higher carrier mobility than graphene on a SiO_2 substrate [77]. Hexagonal Boron Nitride (h-BN) is considered crucial for graphene physics research since it offers a flat and charge-free substrate [78]–[82]. Furthermore, in the direction perpendicular to the layers, the breakdown electric field of h-BN is as high as 12 MV cm^{-1} for mono layer [83] and 21 MV cm^{-1} for 3nm thick [84] layer. h-BN can be employed as a gate dielectric in FETs with high mobility and carrier density because of these properties. In our graphene detector, we used a monolayer of graphene on top of a monolayer of h-BN to increase graphene mobility and improve the resonant response.

3.4 Novel Broadband Antenna

High responsivity remains a challenge due to the low coupling efficiency between the detector and the incident terahertz wave. Gated plasmons in a single-gate FET are weakly coupled to terahertz radiation due to the vigorous screening of gate plasmons by the metal gate electrode and their vanishingly small net dipole moment. Terahertz detectors using field-effect transistors may be made more responsive in three ways. The

first is to replace a conventional gate configuration with a grating-gate structure [85]. Multiple gates (grating gates) on a common channel or multi-channel FETs with intrinsic source and drain connections can boost coupling efficiency significantly. The second technique is to use a silicon lens or a medium-sized dielectric cube [86], and the third option is to use an antenna or array structures [87].

An adequately constructed planar antenna, particularly for antenna structures, can dramatically improve coupling efficiency and hence detector responsivity. Dipole [88], bow-tie [18], [89]–[92], patch [93], [94], and loop [19], [95]–[98] are the most widely used antennas. In linear polarized THz detection, the antennas above are utilized. However, spiral antennas are commonly used for circularly polarized or non-polarized broadband detection [27], [99]–[101] . We have employed a bowtie and a spiral antenna with our grating gate-based THz detector.

3.1 Experimental Design

3.1.1 Device Design:

An insulating dielectric layer must be placed between the channel and the gate, sandwiching the graphene between the substrate and the oxide layer, to manufacture devices with gate electrodes. Because the materials above and below the graphene have an influence on the carriers, this method severely restricts graphene mobility. The substrate and dielectric material influence graphene mobility. The mobility of graphene reduces drastically when insulating material is deposited over it to make a FET, and it is even lower than the mobility of silicon. How to have a grating gated transistor while maintaining high graphene mobility values has been a challenge

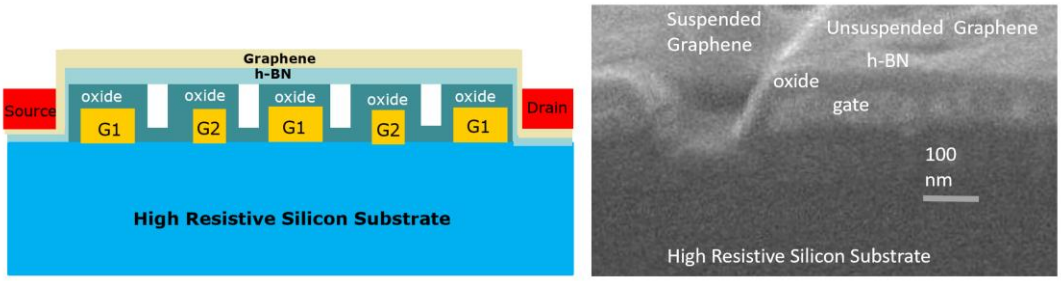

Figure 3.1. (a) Schematic of graphene and h-BN heterostructure field effect transistor and (b) SEM image showing the suspended and unsuspended graphene.

waiting to be addressed. We have used the reverse transistor model [102] instead of the traditional transistor structure and suspending graphene over specific regions, preventing it from being sandwiched. This enables gate control while yet maintaining a high level of mobility. In the ungated zone, graphene will be suspended in the air, whereas in the gated regions, it will be over the oxide. Such a transistor can attain extraordinarily high mobility with the proper graphene treatment. In our design we have used monolayer of graphene on top of monolayer of hexagonal boron nitride (h-BN) as active region. Figure 3.1(a) depicts the schematic of our graphene device, whereas Figure 3.1(b) depicts a SEM image of suspended and unsuspended graphene.

3.1.2 Fabrication Process Flow:

The process to fabricate a graphene device consists of multiple aligned layers using mask aligner and hybrid lithography approach. We have employed both photolithography and electron beam lithography (EBL) to fabricate our graphene device. We have used a high resistive silicon wafer substrate and deposited 120nm Alumina (Al_2O_3) which will act as the base insulating layer using the e-beam evaporator tool. We transferred the local and global alignment marks in the wafer using optical

photolithography process. We performed the gate layer and source and drain pattern writing using the electron beam lithography process.

We then deposited Ti (5nm)/Au (45nm) metals for gates and Ti (10nm)/Au (60nm) metals for source-drain using e-beam evaporation (EBE) method. Using ALD process, 33nm Alumina was deposited which will be the gate oxide level for our transistors. We have used the ALD process to ensure the gate oxide with minimal holes for minimal gate leakage current. After completing the oxide etching and contact mask transfer, 120nm aluminum was deposited as a contact pad metal. To obtain high mobility from graphene at a room temperature, we deposited a monolayer graphene on top of the hexagonal boron nitride to form a heterostructure combination. And finally, we performed the Mesa etch which will define the active region. In our case the graphene is the active region.

3.2 Device Characterization Results and Discussion

3.2.1 Electrical Characterization:

The electrical characterizations are carried out at room temperature using a 4-probe semiconductor parameter analyzer (SPA). By sweeping the drain voltage from negative to positive while keeping the gate at 0 V, the source-drain current and gate leak current are measured first. If the gate current and channel current are in the same order, the device is discarded, and a new one is tested until a device with a low gate current is identified. The drain voltage is then maintained at a level sufficient to generate a few tens of microamperes. Negative to positive gate voltage swept is done to measure channel

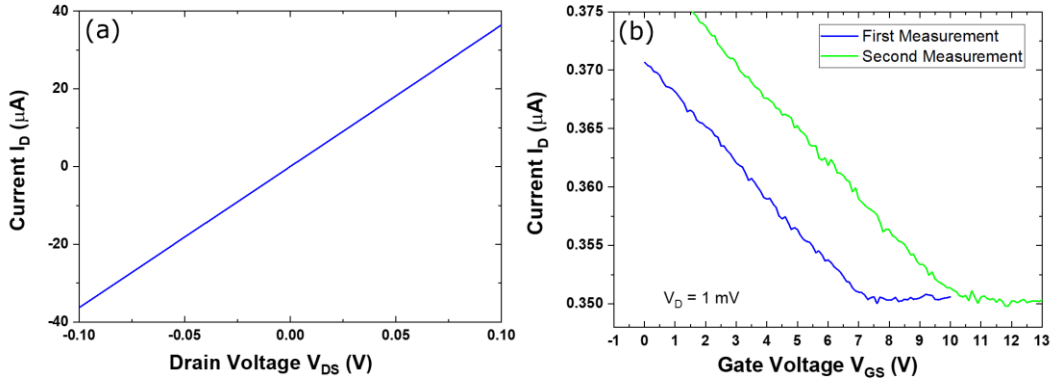

Figure 3.2. I-V Characteristics (a) Drain current as a function of source-drain voltage. (b) Drain current as a function of gate voltage.

current minima, implying the channel gate control. Once the devices have passed all of these tests, they are measured using the optical setup.

Figure 3.2 (a) depicts drain current as a function of source-drain voltage, whereas figure 3.2 (b) depicts the drain current as a function of gate voltage We took two measurements to demonstrate the current flow. Despite the fact that the gate and channel currents are only a few orders of magnitude apart, the channel current may be controlled by applying a voltage.

3.2.2 Optical Characterization:

Terahertz transmission and response are measured using a tunable frequency backward Wave Oscillator (BWO) source and a pyro-electric THz sensor incorporated into an optical transmission setup. The device can detect THz transmission from samples in the 180 to 380 GHz and 540 to 1120 GHz frequency bands (when a tripler is added to the emission port). Detector response as a function of frequency can be measured using the cryogenic system, which can reach temperatures of 65K. Figure 3.3 depicts our linear grating gate devices' temperature-dependent responsivity.

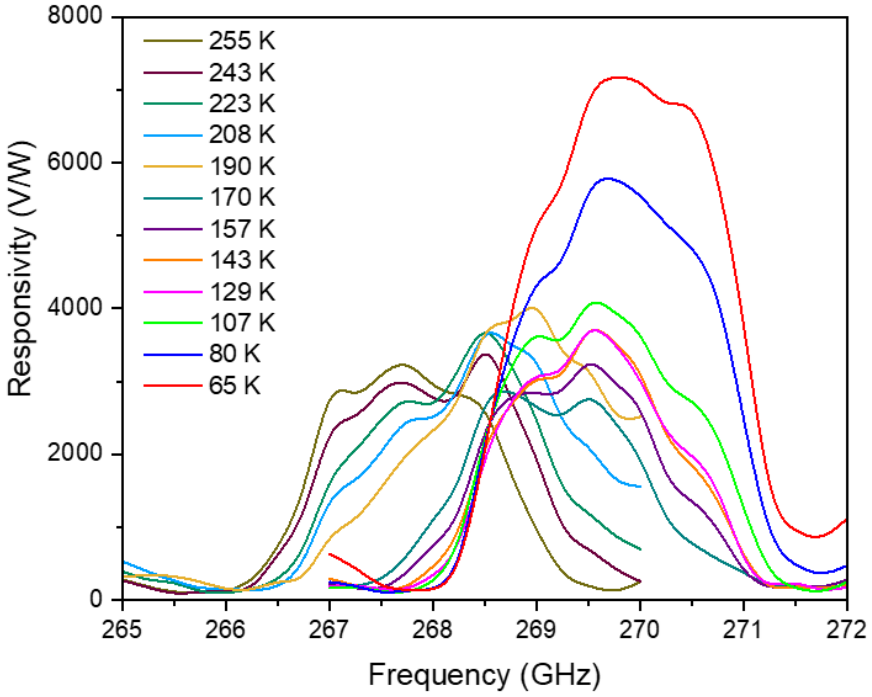

Figure 3.3. Temperature dependent responsivity of grating gate devices.

Although the resonance response and responsivity at cryogenic temperatures i substantially higher than at room temperature, we still observe a robust room temperature response and responsivity.

From our dual grating-gate structure we have obtained four strong resonance

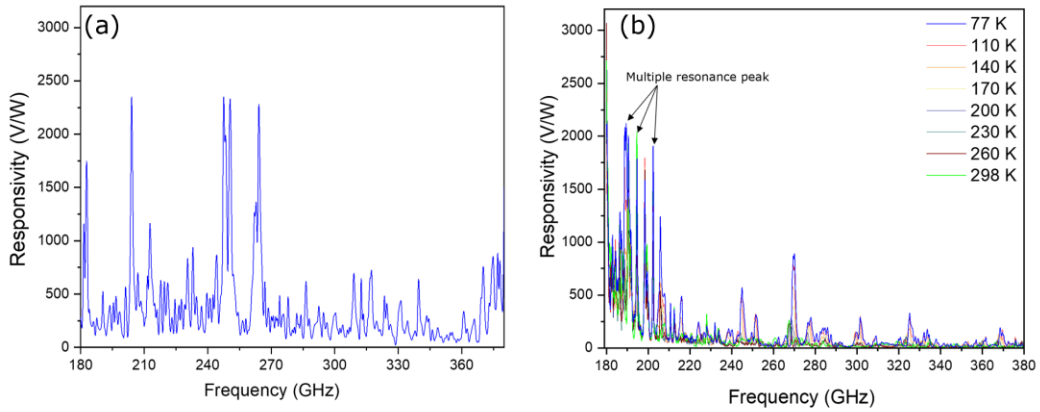

Figure 3.4. (a) Responsivity of dual grating gate device at room temperature and (b) Temperature dependent responsivity response at different frequencies.

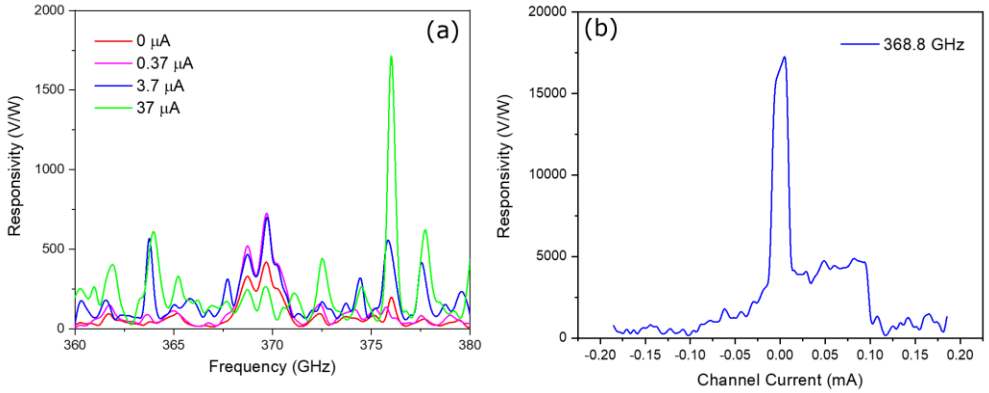

Figure 3.5. (a) Responsivity ($V=R=(x^2+y^2)^{1/2}$ of signal) as a function of channel current at different frequencies. (b) Responsivity and channel current as a function of channel voltage at 368.8 GHz resonant mode.

responsivity peaks at around 2.4kV/W with a highest quality factor (Q~267) as shown in figure 3.4(a). In figure 3.4(b), under different temperature the same device shows multiple resonance peak with highest responsivity at around 3.1kV/W. The discrepancy in responsivity response might be caused by a non-uniform graphene layer in the device, which could occur during graphene transfer.

The responsivity response as a function of channel current and channel response is shown in figure 3.5(a) and 3.5(b). The maximum channel current correlates to the highest resonant responsivity response, demonstrating the detector's efficiency.

3.2.3 Material Characterization:

We used Raman spectroscopy to establish the existence of graphene materials in our device and to determine the cause of multiple resonance. Non-uniform graphene layers, and in certain cases several graphene layers, might be the cause of numerous resonance responses. The Raman 2D band G band (2D/G) ratio provides information on the graphene layer. There is monolayer graphene if the 2D/G ratio is more than 1.6, and multiple layer graphene if the ratio is less than 1.6.

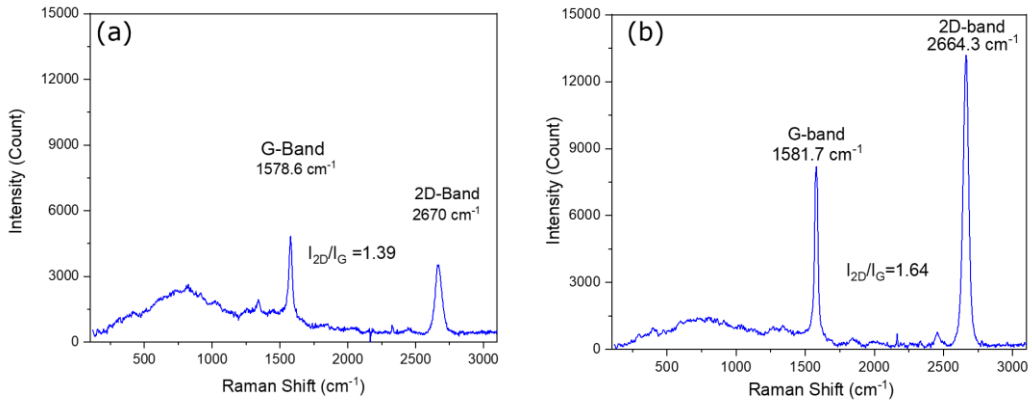

Figure 3.6. Raman measurements for the same at different reference point (a) Ratio of 2D/G<1.6 confirms multilayer graphene presence and (b) Ratio of 2D/G>1.6 confirms monolayer graphene presence.

3.3 Conclusion

We have fabricated and characterized the h-BN and graphene heterostructure based terahertz detector with highest responsivity of around 3.1kV/W at room temperature condition. Several issues emerged during device fabrication, which might explain why we were unable to achieve our goal response of more than 4kV/W. Initially, we discovered an oxide bubble in our wafer after employing the e-beam evaporation technique to deposit the Al metal contact pad. The presence of two separate processes (E-beam evaporation and ALD) and tool environment and temperature conditions for depositing Al_2O_3 dielectric might be the cause of this oxide bubble by causing a leakage from the lower oxide layer due to high film stress.

Second, we deposited Ti/Au metal to define the Source-drain metal after source-drain e-beam lithography writing, however when we tried to lift-off the metal, metal was everywhere in the wafer, and it would not lift-off. We had to subsequently selectively remove the metal off our wafer to etch Ti/Au metal, which resulted in some

device damage. It also made difficult to write the second time source-drain e-beam lithography. And finally, after Ti/Au metal deposition we had faced again the lift-off issue but this time it only affects some devices leaving behind a huge chunk of metal in the device. We discovered that the e-beam evaporation tool was causing the metal lift off problem by producing a high temperature and a crazy non-uniform deposition rate. For the next generation graphene device, we can achieve highest responsivity response for the detector by having a perfect fabricated device.

CHAPTER 4 DIAMOND TERAHETZ DETECTOR

4.1 Introduction

Silicon-based electronic devices have struggled to meet future demands for high temperature, high power, and high frequency due to bandgap energy, thermal conductivity, and electron saturation velocity constraints. Wide bandgap materials like 4H-SiC, GaN, and diamond are used to avoid the issues associated with Si-based substrates [103]–[106]. For the manufacture of electronic devices, the diamond emerged as the most advantageous of these materials. Wide bandgap, high carrier mobility, strong breakdown field, and high saturation velocity are some of the diamond's unique features, making it ideal for electrical devices that operate at high power, high frequency, and in hostile environments [107]–[114].

Diamonds have large optical phonon energy. As a result, optical phonon scattering is suppressed, resulting in an extremely long momentum relaxation time, τ, restricted by optical phonon scattering. Diamond is, therefore, a potential material for sub-THz and THz plasmonic devices [115]–[117].

4.2 Diamond as a candidate of terahertz detection

The Diamond is the extreme semiconductor [118]–[120] for high-power and high-frequency [121] electronic devices due to its ultra-wide bandgap energy (5.5eV), highest thermal conductivity (22 W/m-K) among all known semiconductors, high bulk carrier mobilities (4500 cm^2/Vs for electrons and 3800 cm^2/Vs for holes), and high breakdown field (10 MV/cm) [122]–[126]. To fully develop diamond electrical devices, both p-type

and n-type diamonds are necessary [127]. Boron is used as an electron acceptor (p-type dopant) [128] while phosphorus is used as an electron donor (n-type dopant) [129], [130] in diamond doping. P-type channels were used in all field-effect transistors (FETs) based on semiconductor diamond till today. P-type surface conductivity based on hydrogen-terminated diamond [131]–[134] is also commonly employed. On boron-doped diamond epilayers, P-channel FETs have also been investigated [135], [136]. The failure of n-channel diamond FETs has impeded the advancement of complementary device layout diamond electronics to the integrated circuit level. The phosphorus donor level in diamond is as low as 0.57 eV, making conductive n-type diamond in n-type diamond FETs difficult.

Here, we have presented both p-type and n-type diamond field effect transistor terahertz response both numerically and analytically. We have investigated the hydrodynamic equations both theoretically and analytically with diamond materials and presents their promising future in high power terahertz electronics devices.

4.3 Numerical Analysis

The response of plasmonic THz detectors may be analyzed using the hydrodynamic approach [62] due to the continual size decrease in semiconductor devices and current technology improvements. As a result, FET channels have extremely high electron densities, resembling a two-dimensional electron fluid. The governing equations consists of a continuity equation and Euler equation, as given below [43], [61]:

$$\frac{\partial n_s}{\partial t} + \nabla \cdot (n_s u) = \frac{\partial U}{\partial t} + \frac{\partial (Uu)}{\partial x} = 0 \qquad \text{Eq. 4-1}$$

$$\frac{\partial u}{\partial t} + u\frac{\partial u}{\partial x} + \frac{e}{m}\frac{\partial U}{\partial x} + \frac{u}{\tau} = 0 \qquad \text{Eq. 4-2}$$

Here, u is the hydrodynamic velocity (m/s) and U is the gate-to-channel potential (V), $U=U_0-U_{ch}$ where, U_0 is the DC gate bias above threshold and U_{ch} is the channel potential. Besides, $\tau = \frac{m\mu}{e}$ is the momentum relaxation time of carriers, where m and μ represent the effective mass and the mobility, respectively.

Carrier density, $n_s(U) = \frac{C\eta K_B T}{e^2}\ln(1+\exp(\frac{eU}{\eta K_B T}))$ Eq. 4-3

The unified charge control model (UCCM) [137], [138] can be used to relate n_s and U as shown in Eq. 4-3. The UCCM reduces to $n_s = \frac{CU}{e}$, when $eU >> K_B T$.

For boundary condition, we have considered the typical ac short circuit at the source end and ac open circuit at the drain end of the channel as a boundary condition [43], [61] as follows,

$$U(x=0,t) = U_0 + U_a(t) = U_0 + V_{am}\cos(2\pi f t) \quad \text{Eq. 4-4}$$

$$j(x=L,t) = 0 \quad \text{Eq. 4-5}$$

Here, U_0 is the gate voltage swing, $U_a(t)$ represents the pulsed small-signal voltage induced by the incoming radiation, j is the current flux density and V_{am} is the amplitude of the incident AC voltage. The above-mentioned hydrodynamic model is valid when $1/\tau_{ee} >> 1/\tau$ [137], [139], [140] , where τ_{ee} is the electron–electron scattering rate and τ represents the momentum relaxation time.

The relation of plasma velocity, s, can be represented as the function of the gate voltage swing for a 2DHG in diamond as follows [141], [142]

$$s = \sqrt{\frac{\eta V_{th}}{m_{eff} m_o}\left(\left[1+\exp\left(-\frac{U_o}{\eta V_{th_o}}\right)\right]\ln\left[1+\exp\left(\frac{U_o}{\eta V_{th}}\right)\right]\right)} \quad \text{Eq. 4-6}$$

here, U_o is the gate voltage swing, V_{th} is the thermal voltage, η is the subthreshold ideality factor, m_{eff} is the hole effective mass, and m_0 is the free electron mass. FET acts as a resonator when the fundamental frequency of plasma waves, $f_p = \frac{s}{4L}$,where L is the gate length.

4.3.1 Terahertz detector response without viscosity

The solution of Eq. 4-1 and Eq. 4-2 can be present as follows,

$$u = \bar{u} + u_1 + u_2 \dots\dots\dots \quad \text{Eq. 4-7}$$

$$U = \bar{U} + U_1 + U_2 \dots\dots\dots \quad \text{Eq. 4-8}$$

Here, $\bar{u}$ and $\bar{U}$ are the time-averaged electron velocity and channel potential, and u_n and U_n are the $n\omega$ frequency varying electron velocity and channel potential [ω=input frequency]. Different harmonics are coupled due to the non-linearity of equations Eq. 4-1 and Eq. 4-2. If the input signal, U_a is relatively small then u_1, U_1 are proportional to U_a while $\bar{U} - U_0$, $\bar{u}$, u_2, U_2 are proportional to U_a^2.

Considering the first order in U_a, we have the following

$$\frac{\partial u_1}{\partial t} + \frac{\partial U_1^*}{\partial x} + \frac{u_1}{\tau} = 0 \quad \text{Eq. 4-9}$$

$$\frac{\partial U_1^*}{\partial t} + s^2 \frac{\partial u_1}{\partial x} = 0 \quad \text{Eq. 4-10}$$

Where $U_1^* = \frac{eU_1}{m}$ and $s = \sqrt{\frac{eU_0}{m}}$, where s is the plasma wave velocity. We have the following for the second order time dependent:

$$\frac{d}{dx}\left(\overline{U^*} + \frac{\langle u_1^2 \rangle}{2}\right) + \frac{\bar{u}}{\tau} = 0 \quad \text{Eq. 4-11}$$

$$\frac{d}{dx}(s^2\bar{u} + \langle U_1^* u_1 \rangle) = 0 \quad \text{Eq. 4-12}$$

Here, $\overline{U^*} = \frac{e\bar{U}}{m}$ and $\langle a \rangle$ denotes the time average over the period 2π/ω. Now applying the boundary condition from Eq. 4-4 & Eq. 4-5 to Eq. 4-9 & Eq. 4-10, we get,

$$U_1(0) = \frac{e}{m} U_a \, cos\omega t \qquad \text{Eq. 4-13}$$

$$\bar{U}(0) = \frac{e}{m} U_0 \qquad \text{Eq. 4-14}$$

$$\bar{u}(0) = u_1(L) = 0 \qquad \text{Eq. 4-15}$$

The solution for $u_1$and $U_1$are proportional to exp*(ikx-iωt)* and we obtain the dispersion relation as follows,

$$\omega^2 + i\frac{\omega}{\tau} - s^2k^2 = 0 \qquad \text{Eq. 4-16}$$

As a result, the dispersion relation of plasma wave can be stated as follows:

$$k = \pm k_0 = \pm \frac{\omega}{s}\sqrt{1 + \frac{i}{\omega\tau}} \qquad \text{Eq. 4-17}$$

The solution of Eq. 2-9 and Eq. 2-10 are,

$$U_1 = Re[(C_1 e^{ik_0 x} + C_2 e^{-ik_0 x})e^{-i\omega\tau} \qquad \text{Eq. 4-18}$$

$$u_1 = Re[\frac{\omega}{k_0 s^2}(C_1 e^{ik_0 x} - C_2 e^{-ik_0 x})e^{-i\omega\tau} \qquad \text{Eq. 4-19}$$

$$C_1 = \frac{U_a^*}{1+\exp(2ik_0 L)} \qquad \text{Eq. 4-20}$$

$$C_2 = \frac{U_a^*}{1+\exp(-2ik_0 L)} \qquad \text{Eq. 4-21}$$

where, $U_a^* = \frac{eU_a}{m}$.

The plasma waves are excited by this ac voltage and the dc gate to source voltage determines the velocity, s. A FET biased only by the gate-to-source voltage and subjected to electromagnetic radiation develops a constant drain to source voltage that has a resonant dependence on the radiation frequency, with maxima at the plasma oscillation

frequency and its odd harmonics, due to the nonlinear properties of the electron fluid and the asymmetry in the boundary conditions and can be expressed as follows [62],

$$\frac{\Delta U}{U_o} = \frac{1}{4}\left(\frac{U_a}{U_o}\right)^2 f(\omega) \qquad \text{Eq. 4-22}$$

where

$$f(\omega) = 1 + \beta - \frac{1+\beta\cos(2k_1 L)}{sinh^2(k_0'' L)+cos^2(k_0' L)} \qquad \text{Eq. 4-23}$$

Here, $$\beta = \frac{2\omega\tau}{\sqrt{1+(\omega\tau)^2}} \qquad \text{Eq. 4-24}$$

Where, $k_0 = k_1 + ik_2$ and can be found from Eq. 4-17 as,

$$k_1 = \frac{\omega}{s}\sqrt{\frac{\sqrt{1+\frac{1}{(\omega\tau)^2}}+1}{2}} \qquad \text{Eq. 4-25}$$

$$k_2 = \frac{\omega}{s}\sqrt{\frac{\sqrt{1+\frac{1}{(\omega\tau)^2}}-1}{2}} \qquad \text{Eq. 4-26}$$

4.3.2 Terahertz detector response with temperature dependent viscosity

The solution of Eq. 4-1 and Eq. 4-2 can be present as follows,

$$u = \bar{u} + u_1 + u_2 \ldots\ldots\ldots \qquad \text{Eq. 4-27}$$

$$U = \bar{U} + U_1 + U_2 \ldots\ldots\ldots \qquad \text{Eq. 4-28}$$

Here, $\bar{u}$ and $\bar{U}$ are the time-averaged carrier velocity and gate-to-channel potential, and u_n and U_n are the $n\omega$ frequency varying carrier velocity and channel potential [ω=input frequency]. Different harmonics are coupled due to the non-linearity of Eq. 4-1 and Eq. 4-2. If the input signal, U_a is relatively small then u_1, U_1 are proportional to U_a while $\bar{U} - U_0$, $\bar{u}$, and u_2, U_2 are proportional to U_a^2. For the first order in U_a, the equations are as follows.

$$\frac{\partial u_1}{\partial t} + \frac{\partial U_1^*}{\partial x} + \frac{u_1}{\tau} - \vartheta \frac{\partial^2 u_1}{\partial x^2} = 0 \qquad \text{Eq. 4-29}$$

$$\frac{\partial U_1^*}{\partial t} + s^2 \frac{\partial u_1}{\partial x} = 0 \qquad \text{Eq. 4-30}$$

Where $U_1^* = \frac{eU_1}{m}$, $s = \sqrt{\frac{eU_0}{m}}$, where s is the plasma wave velocity and v is the viscosity.

We have added one viscosity dependent term $\vartheta \frac{\partial^2 u_1}{\partial x^2}$ [137] in Eq. 4-29, compared to our original equation Eq. 4-9 while equation Eq. 4-10 and Eq. 4-30 are the same. The temperature dependent kinematic viscosity ϑ [140], [143] can be numerically expressed as below:

$$\vartheta = \frac{2\hbar}{\pi m} \frac{1}{\ln(2)} (T_F \geqq 0 \;\&\&\; T_F \leqq T) + \frac{2\hbar}{\pi m} \frac{T_F^2}{T^2} \frac{1}{\ln\left(\frac{2T_F}{T}\right)} (T_F \geq T) \qquad \text{Eq. 4-31}$$

We have the following for the second order time dependent:

$$\frac{\partial}{\partial x}\left(\overline{U^*} + \frac{\langle u_1^2 \rangle}{2}\right) + \frac{\bar{u}}{\tau} - \vartheta \frac{\partial^2 \bar{u}}{\partial x^2} = = 0 \qquad \text{Eq. 4-32}$$

$$\frac{\partial}{\partial x}(s^2 \bar{u} + \langle U_1^* u_1 \rangle) = 0 \qquad \text{Eq. 4-33}$$

Here, $\overline{U^*} = \frac{e\bar{U}}{m}$ and $\langle a \rangle$ denotes the time average over the period 2π/ω. Now applying the boundary condition from Eq. 4-4 & Eq. 4-5 to Eq. 4-29 & Eq. 4-30 we get,

$$U_1(0) = \frac{e}{m} U_a \, cos\omega t \qquad \text{Eq. 4-34}$$

$$\bar{U}(0) = \frac{e}{m} U_0 \qquad \text{Eq. 4-35}$$

$$\bar{u}(0) = u_1(L) = 0 \qquad \text{Eq. 4-36}$$

The solution for $u_1$and $U_1$are proportional to *exp(ikx-iωt)* and we obtain the dispersion relation as follows,

$$\omega^2 + i\frac{\omega}{\tau} + i\omega v k^2 - s^2 k^2 = 0 \qquad \text{Eq. 4-37}$$

As a result, the dispersion relation of plasma wave can be stated as follows:

$$k = \pm k_0 = \pm\sqrt{\frac{\omega\,(\omega+i\gamma)}{s^2-i\omega v}} \qquad \text{Eq. 4-38}$$

Where, $k_0 = k_1 + ik_2$ and can be found from Eq. 4-49 as,

$$k_1 = \frac{\omega}{s\sqrt{1+(\omega\tau_1)^2}}\sqrt{\frac{\sqrt{(1-\frac{\tau_1}{\tau})^2+\left(\omega\tau_1+\frac{1}{\omega\tau}\right)^2}+(1-\frac{\tau_1}{\tau})}{2}} \qquad \text{Eq. 4-39}$$

$$k_1 = \frac{\omega}{s\sqrt{1+(\omega\tau_1)^2}}\sqrt{\frac{\sqrt{(1-\frac{\tau_1}{\tau})^2+\left(\omega\tau_1+\frac{1}{\omega\tau}\right)^2}-(1-\frac{\tau_1}{\tau})}{2}} \qquad \text{Eq. 4-40}$$

viscosity, $\tau_1 = \frac{\vartheta}{s^2}$, where τ_1 is the viscosity dependent relaxation time.

The solution of Eq. 4-29 and Eq. 4-30 are,

$$U_1 = Re[(C_1 e^{ik_0 x} + C_2 e^{-ik_0 x})e^{-i\omega\tau} \qquad \text{Eq. 4-41}$$

$$u_1 = Re[\frac{\omega}{k_0 s^2}(C_1 e^{ik_0 x} - C_2 e^{-ik_0 x})e^{-i\omega\tau} \qquad \text{Eq. 4-42}$$

$$C_1 = \frac{U_a^*}{1+\exp(2ik_0 L)} \qquad \text{Eq. 4-43}$$

$$C_2 = \frac{U_a^*}{1+\exp(-2ik_0 L)} \qquad \text{Eq. 4-44}$$

where, $U_a^* = \frac{eU_a}{m}$. The ac voltage generates plasma waves, and the dc gate to source voltage determines the velocity, s. A FET biased entirely by the gate-to-source voltage and exposed to electromagnetic radiation creates a continuous drain to source voltage that has a resonant dependence on the radiation frequency, with maxima at the plasma oscillation frequency and its odd harmonics, and can be described as follows.,

$$\frac{\Delta U}{U_o} = \frac{1}{4}(\frac{U_a}{U_o})^2 f(\omega) \qquad \text{Eq. 4-45}$$

where

$$f(\omega) \approx 1 + \beta - \frac{\beta[\cos^2(k_1 L) - \frac{\tau_1}{\tau}\sin^2(k_1 L)] + \cos(2k_1 L)}{sinh^2(k_2 L) + cos^2(k_1 L)} \quad \text{Eq. 4-46}$$

$$\beta = \frac{\omega^2}{s^2}\frac{1}{k_1^2 + k_2^2} = \frac{2(1+(\omega\tau)^2}{\sqrt{(1-\frac{\tau_1}{\tau})^2 + \left(\omega\tau_1 + \frac{1}{\omega\tau}\right)^2}} \quad \text{Eq. 4-47}$$

The detector response, ΔU, of equation 4-22 and 4-45 can be normalized as [144],

$$dU_n = \frac{\Delta U * U_o}{U_a{}^2} \quad \text{Eq. 4-48}$$

4.4 Materials and Methods

The schematic of proposed diamond FET device is shown in figure 4.1. To simulate the gated p-diamond and n-diamond plasmonic FETs, we use a one-dimensional hydrodynamic model in a COMSOL equation-based modelling. The governing equations consists of a continuity equation and Euler equation, as given in equation 4-1 and 4-2.

Electron-hole mobility of the p-, and n-diamond FET channel can be expressed as, $\mu = \frac{e\tau}{m}$, where, e is the electron charge, m electron mass and τ is the momentum relaxation time. Mobility is a temperature dependent parameter and is proportional to $T^{-3/2}$ as $\tau_{thermal} \sim l\,T^{\frac{-1}{2}} \sim T^{\frac{-3}{2}} \sim \mu$. We have calculated and extracted the values of temperature dependent hole and electron mobility, μ_h and μ_n and momentum relaxation time, τ from [145]. The material parameters for p-diamond are shown in table 4.1. The

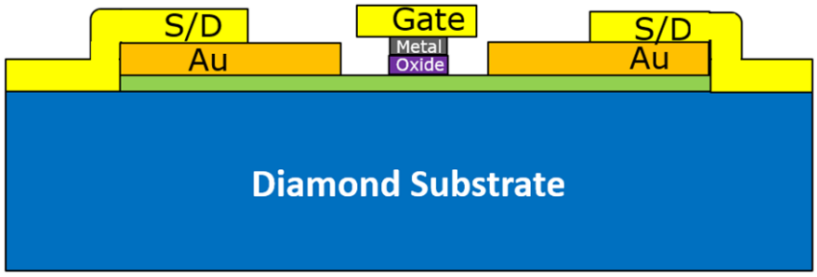

Figure 4.1. Schematic of diamond FET.

fundamental plasma frequency, $f_p = \frac{s}{4L}$, was derived using an open drain boundary condition and a THz signal injected between the source and gate. We employed a short circuit at the source and an open circuit at the drain as boundary conditions, as explained in equations 2-4 and 2-5. To formulate and solve the hydrodynamic problem, we used partial derivative equation (PDE) form of equation based COMSOL modeling and Dirichlet boundary condition.

Table 4.1. Material parameters for p-Diamond

Gate length, L	50nm
Gate to channel separation, d (L>>d)	4nm
Dielectric constant	5.7
Refractive index	2.42
Mobility	4.68 m^2/V.s (70K), 0.5284 m^2/V.s (300K)
Relaxation time	15.318 ps (70K), 1.9919 ps (300K)
Initial gate to channel voltage	1V
Threshold voltage	0.4V
Effective mass	0.663
Amplitude	0.01 V
Viscosity	1.6 cm^2/s for all T

Similarly, we have employed the same strategy to calculate the one-dimensional n-diamond FET. The material parameters for n-diamond are shown in table 4.2. The plasma velocity $s = \sqrt{\frac{eU_0}{m_{eff}}}$, where m_{eff} is the effective mass of electron (or, hole) is set for the above threshold operation, which is determined internally by the model equations.

Table 4.2. Material parameters for n-Diamond

Gate length, L	50nm
Gate to channel separation, d (L>>d)	4nm
Dielectric constant	5.7
Refractive index	2.42
Mobility	6.40 m^2/V.s (70K), 0.72 m^2/V.s (300K)
Relaxation time	13.1 ps (70K), 1.47 ps (300K)
Initial gate to channel voltage	1V
Threshold voltage	0.4V
Effective mass	0.36
Amplitude	0.01 V
Viscosity	3.05 cm^2/s (70K) and 2.9 cm^2/s (300K)

The Fermi energy, E_F, and Fermi temperature T_F can be expressed as follows, $E_f = \frac{\pi\hbar^2 C U_0}{em}$, where, capacitance, $C = \frac{\epsilon_r \epsilon_0}{d}$ and d is the gate to channel separation., and $T_f = \frac{E_f}{KB}$. We have adjusted the dielectric thickness by considering the L>>d condition.

4.5 Results and Discussion

The entire numerical and analytical response was evaluated based on three factors: viscosity, without viscosity, and high temperature. Considering no viscosity effect in our model as explained in the section 2.3.1 in equation 2-20 and 2-21, we have simulated and analytically calculated for both p- and n-diamond materials. Figure 4.2 shows the normalized detector response for p- and n-diamond as a function of temperature considering no viscosity. p-Diamond has a detector resonance response at around 2.5THz while n-diamond detector shows response at around 3.5 THz. Similarly considering the viscosity effect in our model as explained in the section 2.3.2 in equation 2-40 and 2-41, we have simulated and analytically calculated for both p- and n-diamond materials. Figure 4.3 shows the normalized detector response for p- and n-diamond as a

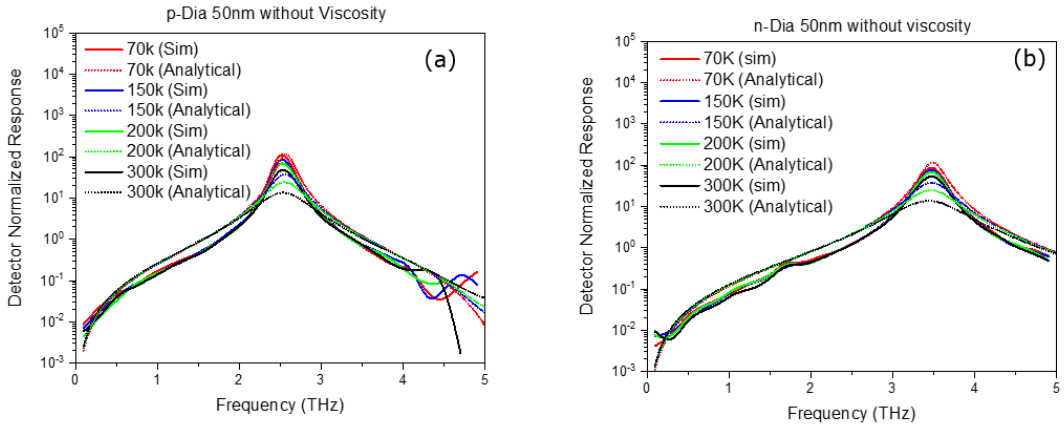

Figure 4.2 (a) p- and (b) n-diamond without viscosity effect for 50nm gate as a function of temperature.

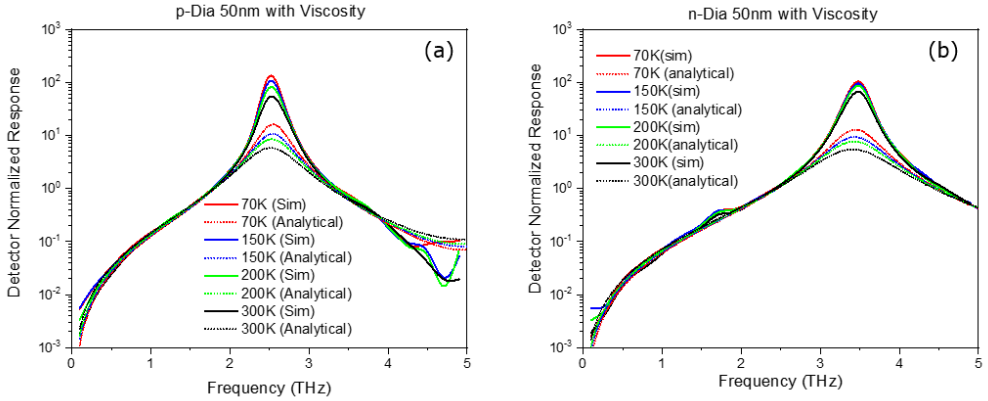

Figure 4.3 (a) p- and (b) n-diamond with viscosity effect for 50nm gate as a function of temperature.

function of temperature considering no viscosity. p-Diamond has a detector has resonance response at around 2.56THz while n-diamond detector shows response at around 3.65 THz.

The comparison between the with viscosity and without viscosity effect is shown in figure 4.4 for both p-diamond and n-diamond as a function of gate length under 300K temperature. So far, we have achieved a comparable response for both simulated and analytical result except when considering the effect as a function of gate under a certain temperature value. From figure 4.4 (a) & (b) it is evident that the analytical calculation differs from the simulated calculation by an exponential order of magnitude. The reason

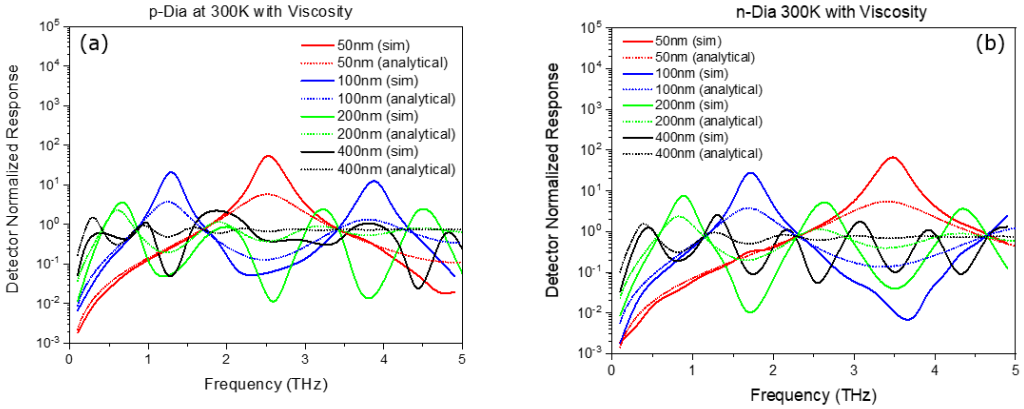

Figure 4.4 Comparison between with viscosity and without viscosity for (a) p- and (b) n-diamond as a function of gate length at 300K temperature.

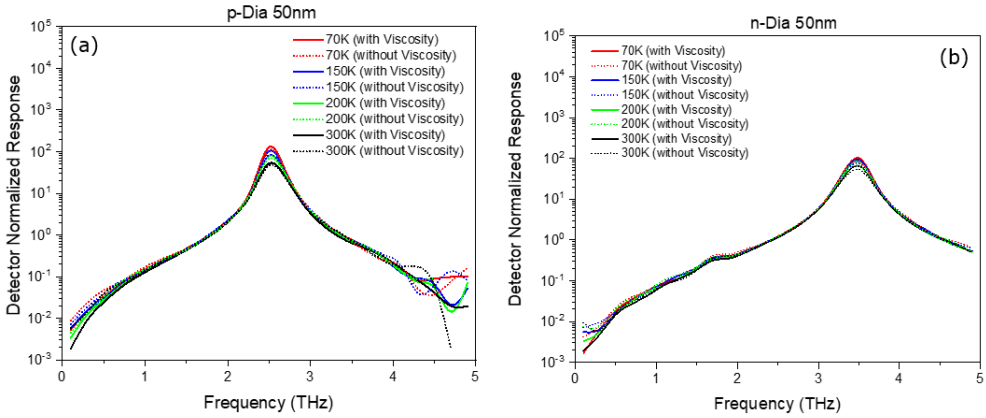

Figure 4.5 Comparison of viscosity and without viscosity effect of (a) p- and (b) n-diamond for 50nm gate.

behind the discrepancy could be the result that the analytical calculation does not consider all behavior or applied any boundary condition rather it solved the set of equations based on the defined parameters. Because of this the analytical response does not reflect the simulation behavior more accurately.

In figure 4.5 we have presented the effect of viscosity by presenting both with and without viscosity response for both p- and n-diamond. Given a large effective mass (m_{eff}) of diamond, the Fermi temperature T_F could be very low. So that for T = 77 K and T = 300 K, we always have T >> T_F and the carriers are always non-degenerate. Thus, following the expression used of viscosity, ϑ, in equation 2-42 and the viscosity used in 77 K and 300 K are the same for p-diamond and are different for n-diamond. Although the value of n-diamond viscosity is low. Since the viscosity in diamond is always very low, which has a minor effect on the simulation, we could use the approximation from equation 2-42 and the value is always very low. In general, viscosity effect tends to cause a decay in the response but in our diamond scenario we do not observe any significant viscosity effect due to its low value.

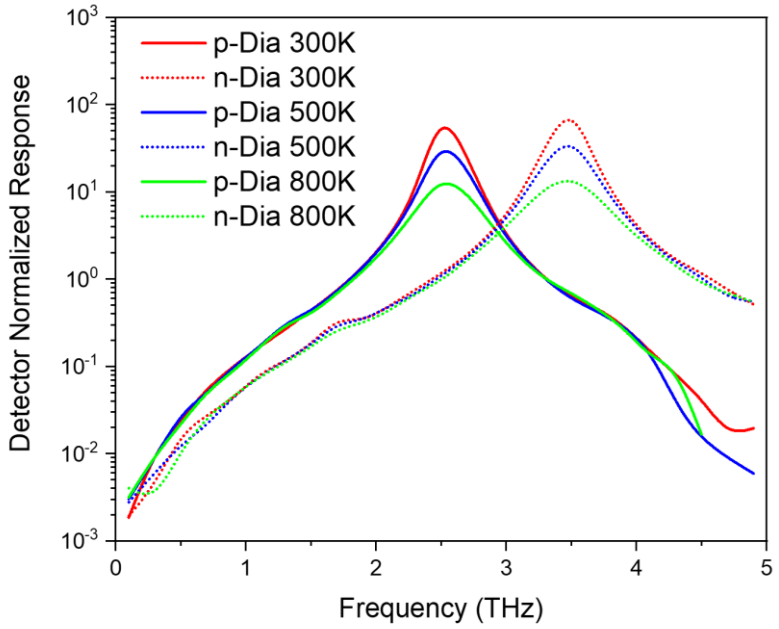

Figure 4.6 High temperature (300K, 500K and 800K) response of p- and n-diamond FET detector.

Finally, we have presented evaluated the detector response for both p-diamond and n-diamond for 300K, 500k and 800K temperature to represents it effectivity in high temperatures applications. Figure 4.6 shows normalized detector response for 50nm gate p- and n-diamond. From the figure we can see that the n-diamond detector response right shifted from the p-diamond and provides a higher resonance response value comparing to its p-diamond counterparts. The reason behind this high resonance value depends on the n-diamond's mobility. We have used a higher number of mobility value for n-diamond from the ref [145]. Recently, it has been reported that n-diamond has a very low mobility value [129]. Depending on the mobility value the result from can significantly change.

4.6 Conclusion

In summary, we have presented three significant novels while working with our diamond FET devices. First, we have investigated n-diamond materials along with p-diamond both theoretically and analytically. Second, we have formulated and solved the hydrodynamic equation using temperature dependent viscosity response for diamond materials. And lastly, we have shown the high temperatures (300K, 500K and 800K) response of both p-diamond and n-diamond materials.

CHAPTER 5 AI POWERED TERAHERTZ VLSI TESTING TECHNOLOGY

5.1 Introduction

The fast expansion of the digital world necessitates cyber security, which spans software and hardware that drives everything from personal gadgets to global infrastructure. Spectre and Meltdown [146], [147] have recently been found as critical chip vulnerabilities, reminding us that systems are only as safe as their weakest link. As physical hardware, all cyber systems rely on semiconductor chips. Chips are the cornerstone of digital trust and are becoming increasingly intricate in modern gadgets, computers, communications networks, and other essential infrastructure. All other layers of a system's cybersecurity can be jeopardized if a physical component is hacked. As a result, hardware security focuses on safeguarding systems against vulnerabilities at the device's physical layer. Modern chips are extremely complicated, with trillions of transistor components that may be damaged or intentionally modified during the design, manufacturing, assembly, and testing stages. For security and reliability, the identification of hidden defects or hardware Trojans in integrated circuit packages is crucial.

Counterfeit integrated circuits are becoming extremely prevalent in the worldwide semiconductor market, with some counterfeit ICs finding their way into high-risk applications such as the military and medical professions [148], [149]. Counterfeit ICs may have a shorter lifespan, malfunction under manufacturer-specified conditions, or leak sensitive data from the system to a third party [150].

5.2 Related Works

Physical and electrical faults have been the two most common categories of obstacles observed when investigating [151], [152] the taxonomy of counterfeit component types and problems in electronic components. A simple, comprehensive, nondestructive, and widely used inspection and testing processes are required to detect counterfeit, forged, or damaged ICs from authentic ICs. The IC packaging industry has developed several non-destructive testing methodologies since the 1970s [153], [154]. Infrared thermography (IRT) [155], [156], surface acoustic waves (SAW) [157], [158], X-ray laminography [159], [160], scanning acoustic microscopy (SAM) [161]–[163], and terahertz transmission and reflection imaging [164] are non-destructive testing and inspection methods for IC packaging. Despite several disadvantages such as limited sensitivity, large processing times, and poor spatial resolution, these approaches are widely employed. X-ray inspection techniques have a spatial resolution of 1-5 μm, IRT 5-30 μm, SAM 30-100 μm, and SAW 90-800 μm [165]–[168].

Among these options, the use of terahertz (THz) radiation is a relatively new concept [169]. Terahertz (0.1–10 THz) waves may penetrate nonmetallic materials and offer sub-micron to nano spatial precision information on composite deterioration [45], [170]. Terahertz waves contain low-energy radiation with no known risks to samples or humans. Cut connecting lines in damaged integrated circuits have been successfully inspected using the laser terahertz-emission microscope (LTEM) instrument (~resolution of 3 μm) [7], [8]. In semiconductor failure analysis laboratories at AMD, IBM, Intel, and TSMC, electro-optical terahertz pulse reflectometry (EOTPR) has been utilized to find and identify flaws in 3D packaged ICs [171], [172]. Near-field imaging systems need

objects to be positioned at a subwavelength distance from the lens, and it cannot be imaged if the object is thicker than 100 μm [164], [173]. Far-field THz imaging is more effective and can detect IC failures due to electrical overstress (EOS) and electrostatic discharge (ESD) [165]. It may also be used to determine the depth of cavities caused by IC package overheating [166] and can distinguish genuine from counterfeit ICs by detecting unexpected IC packaging materials. Due to the intrinsic long wavelength of THz waves, the spatial resolution of far-field THz imaging systems is limited by spot size constraints. As a result, blurring, low signal-to-noise ratio, and low-resolution challenges affect the images [62], [164], [174], [175], and poor image quality prevents accurate identification. In most previous studies, inefficient and inaccurate manual detection was another hurdle to the commercial implementation of THz-based IC identification. As a result, having a reliable and automated detection method is critical. We have devised a novel approach for integrated terahertz IC testing and analysis method to overcome the limitations of existing terahertz-based and other methodologies. We previously demonstrated that MMICs, VLSI, and ULSI circuits produced DC responses at pins, input/output contacts, and leads [62], [174]–[177]. Instead of utilizing terahertz imaging techniques, we recently shown that the DC responses obtained when incoming THz radiation passed through the ICs may be used as differentiating signatures [178]–[183]. Minor biasing alterations can result in significant changes in the transistor's response, improving the approach's efficacy. Voltages formed by terahertz or sub-terahertz radiation at the IC terminals can be utilized to identify defects or variations from the predicted output, forming distinct defect signatures. This technique can predict the lifespan and dependability of individual ICs after the defect diagnostic and identification

operation. For low terahertz radiation intensities, the DC voltage response will be proportional to the intensity. At high terahertz radiation intensities, however, it will most likely be proportional to the intensity's square root [184] or saturate [185]. For transistors having defects, such as strong leakage currents, the response will be significantly different [186]. The spatial resolution of this defect-detection method is determined by the transistor gate size.

The convolutional neural network (CNN), a subset of deep learning methods [180]–[182], was utilized to automate the detection of ICs exhibiting anomalous THz responses. By learning discriminative characteristics from training data, deep learning algorithms may detect outliers and failures [186]–[188]. Even though deep learning models have thrived in a variety of applications, employing them to tackle terahertz testing difficulties remains a hurdle. With the depth of a deep neural network, the number of network parameters connected with it expands exponentially. Millions of network parameters must be determined throughout the training process for a typical moderate-depth deep neural network. As a result, training a deep neural network often requires a lot of labeled data, which might be tough to get by. Transfer learning is an alternative approach to designing a deep learning model from scratch to cope with this problem. It solves a new problem using knowledge from a previous one [189]. We demonstrate that using the transfer learning approach to classify terahertz responses may considerably enhance the accuracy of identifying damaged or altered/modified ICs. The purpose of our research is to use our integrated THz IC testing and analysis framework to detect packaged IC failure and counterfeit ICs.

5.3 Terahertz experimental setup for image scanning

A terahertz detector can be formed using a short-channel field-effect transistor (FET) [45], [61]. Resonant or overdamped electron density waves (also known as plasma waves) were created by THz radiation impinging on the transistor and connected across the contacts or interconnects in the device channel. The rectified response to modulated THz radiation is caused by transistor nonlinearities, which generate DC voltages on the output pins. We have used a lock-in amplifier to measure and record the frequency modulated response. In a nano-stage, the generated DC response is scanned by moving the IC in three dimensions (x, y, and z). The resultant spatial dependence provides a distinct characteristic that may be used to differentiate genuine/healthy ICs from forged/defective ones. Although [179], [190] have shown that this approach is effective, it is not suitable for high throughput testing of complex ICs. Our research improves on prior work [180] by providing a proof-of-concept platform for fast and accurate IC testing utilizing automated scanning and deep learning approach. This new non-invasive and non-destructive method has a substantial advantage over prior radiation-enhanced testing processes.

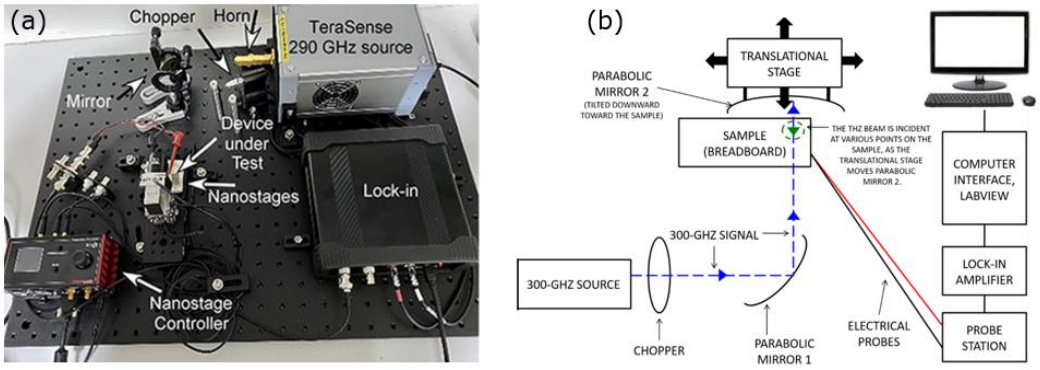

Figure 5.1 Experimental setup for terahertz IC scanning (a) Experimental setup using a IMPATT diode as a terahertz source. (b) Schematic presentation of the terahertz scanning setup using a Virginia Diodes 0.3-THz source for generating spatial terahertz response map for AI based image processing.

This approach can work with or without bias and has no effect on the operation of the device. Unlike standard terahertz imaging, this approach may take use of the terahertz response's intensity, polarization, frequency, and bias dependences at the VLSI or MMIC pins to produce a more detailed IC response. For Si and compound semiconductor devices and circuits, it may also be utilized for flaw identification, reliability prediction, and fabrication process optimization. Even though the wavelength of the radiation is hundreds of micrometers, the spatial resolution of our technology is restricted by the aperture (typically the transistor gate). As a result, it can reach the nanoscale. Such resolution has been demonstrated in previous studies by us [180], [191], and others [192]–[194].

Figure 5.1 depicts two different experimental settings. Figure 5.1a uses a fixed frequency IMPATT diode-based terahertz source operating at 0.290 THz with an output power of 8.5 mW and a 26dB gain detachable horn antenna whereas figure 5.1b uses a Virginia Diodes 0.3-THz source with an output power of about 6 mW. The remainder of the technique is same except for the THz source. A mechanical chopper at 4 kHz modulates the 0.3-THz wave. The collimated and directed signal from parabolic mirror 1 to parabolic mirror 2 directly focused on the IC chip. The parabolic mirror 2 is mounted on a translation stage which allows scanning the chip at different points using the 300-GHz signal. The IC chips were easily mounted on a prototype breadboard for testing. The THz beam was applied at various positions in the XY plane using the translation nano-stage. We now have a two-dimensional scan of the sample because of the parabolic mirror 2 linearly translating over this plane containing the sample.

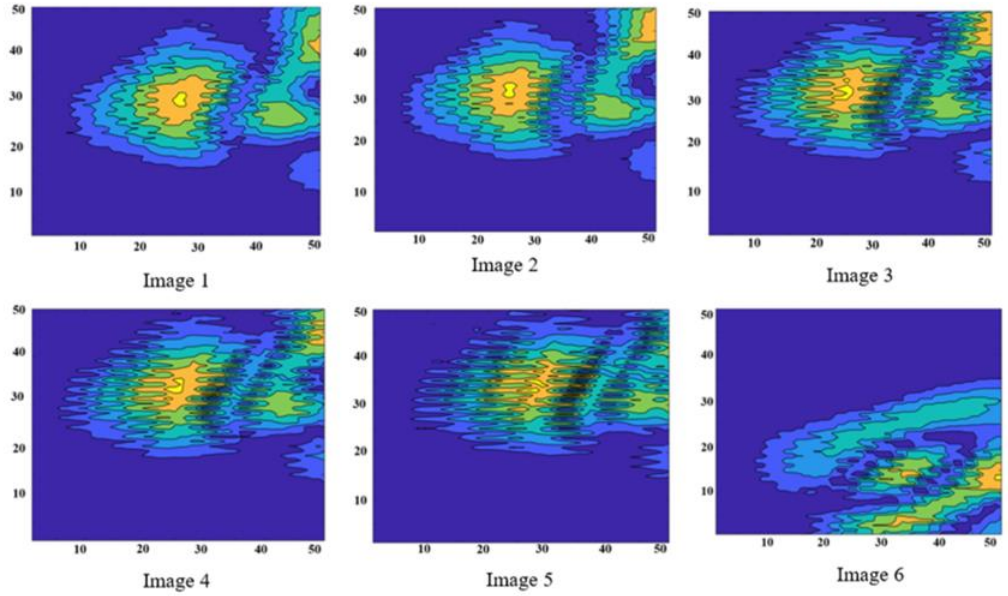

Figure 5.2 Position dependent DC response at a selected pin of the tested IC while a THz beam was swept in 2D for undamaged samples.

A lock-in amplifier operated by a computer running a custom-developed LabView interface measures the DC voltage response caused by the incident THz beam on the

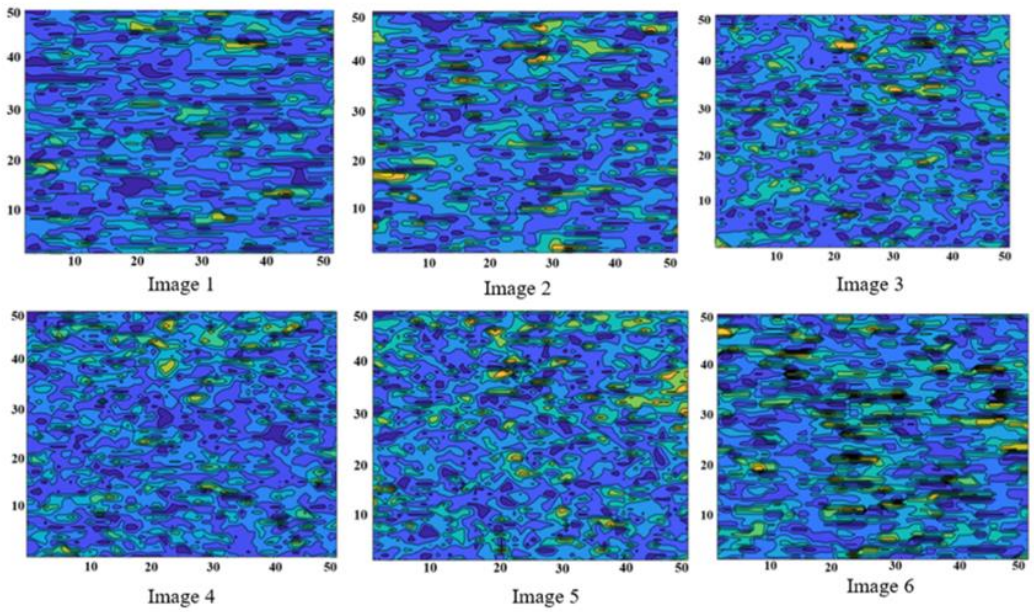

Figure 5.3 Position dependent DC response at a selected pin of the tested IC while a THz beam was swept in 2D for damaged samples.

CE3520K3 IC (20-24 GHz low-noise RF amplifier) pins. We produced a 2D signature response map by scanning the THz on the chips to acquire 50 × 50 image data points. The images from the undamaged samples were first acquired. The samples were subsequently damaged with high voltage, and six images were acquired for the damaged samples. We obtained 6 images of the undamaged ICs and 6 images of the damaged ICs in total. The DC response images of the undamaged and damaged ICs are shown in Figures 5.2 and 5.3, respectively.

5.4 Data Augmentation for Image Data Processing

There are three ways for a machine to learn: supervised learning, unsupervised learning, and reinforcement learning. We utilized supervised learning to train our model using two labeled datasets in our case: Secure images are corresponded to undamaged samples, whereas unsecure images are corresponded to damaged samples. We used four custom strategies and other data augmentation processes to create more image datasets.

5.4.1 Multiplication by Trigonometric function

5.4.1.1 Algorithm 1

We have multiplied our 12 images using the trigonometric functions, first by $\sin(\pi j/V_{max})$ and then by $\cos(\pi k/V_{max})$. Here, V_{max} is the maximum measured response value, and the value of j, k is in the range from 1 to N_{max}, the maximum number of pixels in a row and column (50 in the present case). Figure 5.4a shows algorithm 1.

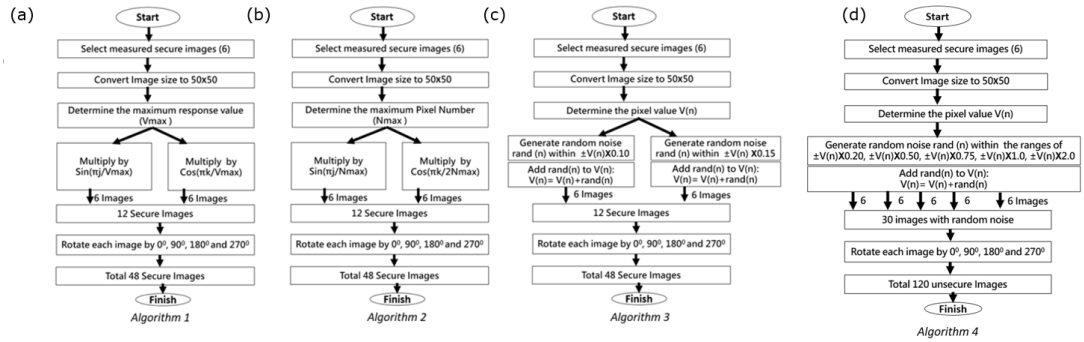

Figure 5.4 Algorithm for data augmentation. (a)Algorithm 1, (a) Algorithm 2, and (a)Algorithm 3 labelled as Secure Image dataset and (d) Algorithm 4 labelled as Unsecure Image dataset.

5.4.1.2 Algorithm 2

We have multiplied our 12 images using the trigonometric functions, first by sin(πj/Nmax) and then by sin(πj/N_{max}). Here, N_{max} the maximum number of pixels in a row/column (50) and the value of j, k is in the range from 1 to N_{max}. Figure 5.4b shows algorithm 2.

5.4.2 Random noise creation

5.4.2.1 Algorithm 3 and Algorithm 4

We added 10% and 15% of the measured response value to the measured image data set with a maximum amplitude of random noise. We used each pixel value of the original image to generate 10% (15%) random data. We added a random value between ± 10% (± 15%) of the original image's pixel value to create the 10% randomized images data set. This approach inherently assumes that variations up to 15% are acceptable for a device's geometries and characteristics. Figure 5.4c shows the image generation using this method. Using the same process as algorithm 3, we added random noise with the maximum amplitude of 20%, 50%, 75%, 100%, and 200% of the measured response value to the measured data set to generate algorithm 4 as shown in figure 5.4d. We labeled 10% and 15% of random noise-created data as secure image sets, while 20%,

50%, 75%, 100%, and 200% of random noise-created data were labeled as unsecure image sets. This method assumes that variations in device geometries and attributes of up to 15% are acceptable. For certain devices/process fabrication foundries, this tolerance rate can be modified to train the AI for higher accuracy.

5.4.3 Rotation

We rotated all the images (both unsecure and secure) three times by 90 degrees to have four sets of images containing 0^0, 90^0, 180^0, and 270^0 data points.

5.4.4 Flip

We generated a new set of data from the original 12 images (6 secure images and 6 unsecure images) by flipping each image horizontally and vertically.

5.4.5 Resize

We used the nearest-neighbor interpolation to shrink the size of each image by a factor of two.

Finally, we have obtained 216 secure images and 416 unsecure images from our original 6 secure images and 6 unsecure images by using our custom data augmentation process.

5.5 Convolution Neural Network

We used the deep network designer tool from MATLAB to create the standard Convolutional Neural Network (CNN). Our CNN model consists of eight layers: an Image input Layer, Convolution2D Layer, BatchNormalization Layer, ReLU Layer, MaxPooling2D Layer, FullyConnected Layer, Softmax Layer, and Classification OutputLayer. The CNN is divided into two sections: feature learning and classification. Convolutional layers, ReLU layers, and pooling layers make up the feature learning part,

while fully connected layers and the SoftMax activation function make up the classification section. Convolution operation (also known as a convolution filter or kernel), activation function, feature map, or activation map make up the convolution layer.

For CNN training, we employed 80% of the image data sets from the secure and unsecure categories. The remaining 20% of image data sets were eventually employed to put the trained CNN to the test. All the training samples ran through the learning process in one epoch before the weights were modified. All weights were modified for sequential training once each training vector was passed sequentially through the training algorithm. Using a small data set in a deep learning model might lead the data to overfit over time, resulting in a falsely greater accuracy rate. Data overfitting occurs when a model imitates the training data too closely. The transfer learning model is the greatest method for dealing with data overfitting.

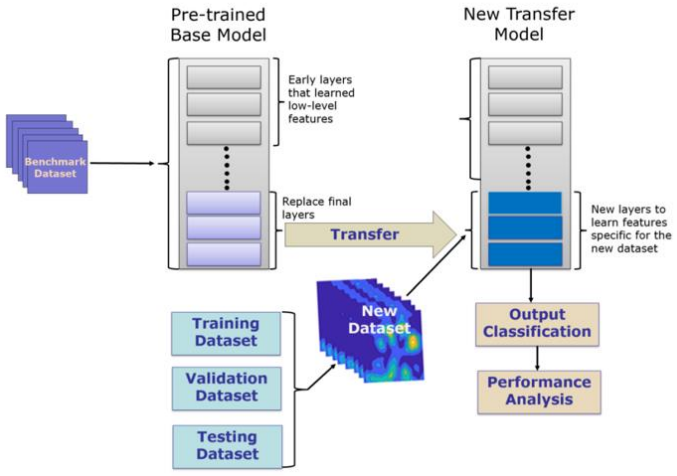

Figure 5.5 Basic framework of Transfer learning model.

5.6 Transfer Learning Model

Transfer learning works on the premise of using prior task knowledge to enhance prediction on a new task. From a variety of source data, it learns more generic characteristics like lines, curves, and forms. Edges are detected in the first layer, forms in the intermediate layer, and task-specific features in the following layers using neural networks. The initial and core layers are used in transfer learning, but the succeeding layers are just retrained. More precisely, it uses the labeled data from the new task to train the following layers. Figure 5.5 shows the basic operation of transfer learning approach.

Transfer learning has several advantages, including reduced training time and improved neural network performance. The vast quantity of data needed to train a neural network is expensive and time-consuming to get. Transfer learning can provide an effective machine learning model with minimum training data since the model has been pre-trained. This is critical in our case since obtaining a big number of datasets proved unattainable. Text classification [195], object identification [196], medical diagnosis [197], art categorization [198], and defect diagnoses [199] are some of the areas where this technique has proven useful.

5.7 Results and Discussion

We employed one CNN model and seven distinct transfer learning models to assess the training and testing accuracy of the images data set: GoogLeNet, MobileNet-v2, AlexNet, VGG16, VGG19, ResNet50, and ResNet101. The fastest models include AlexNet, VGG16, VGG19, and GoogLeNet, whereas the very accurate models are MobileNet-v2, ResNet50, and ResNet101. Table 5.1 provides a broad description of each

Table 5.1 General description of the used CNN and transfer learning models

	Simple CNN Model	Transfer Learning Model						
		Faster Models				Highly Accurate Models		
		AlexNet	VGG16	VGG19	GoogLeNet	MobileNet-v2	ResNet50	ResNet101
Description	8 layers deep Input image size: 227 × 227	8 layers deep Input image size: 227 × 227	16 layers deep Input image size: 224 × 224	19 layers deep Input image size: 224 × 224	22 layers deep Input image size: 224 × 224	53 layers deep Input image size: 224 × 224	50 layers deep Input image size: 224 × 224	101 layers deep Input image size: 224 × 224
No of images	6 Secure, and 6 Unsecure	More than a million images (ImageNet database)						
No of images after augmentation	216 Secure, and 416 Unsecure	216 Secure, and 416 Unsecure images and millions of images of the pretrained network						
Train (80%) and Test (20%) images	**Train Image set:** 172 Secure, 332 Unsecure **Test Image set:** 44 Secure, 84 Unsecure							

model. We used 80 % of the total images for training (172 Secure and 332 Unsecure) and 20% for testing (44 Secure and 84 Unsecure). We split 80 % of the total of the training images to train the CNN model and 20% of the training image sets to validate the training accuracy of our model from the training image sets. We used the initially segregated 20% of the total images to assess the model accuracy once the model training and validation were completed. Our basic CNN model has a classification accuracy of 99.0 % and a testing accuracy of 96.9 %.

Then, using the MATLAB deep learning platform's pre-trained model set, we applied the transfer learning principle. We employed Alex Net, VGG16, VGG19, GoogLeNet, MobileNet-v2, ResNet50, and ResNet101 pre-trained models to learn the feature extraction and classification task using millions of images. The lowest layers of these models were then replaced with our desired classification layer, while the upper layers were frozen, and a new model was created to train. Because more than millions of images were utilized to train the total network, the newly developed model is regarded very robust. Our model's training progress is depicted in Figure 5.6. The training progress

plot, which shows training metrics for each iteration, is essential for keeping track of deep learning network training. It displays how rapidly the network's accuracy increases and whether the training data is becoming overfit. Figure 5.6 shows the training and testing accuracy of a simple CNN model: 99.0% and 96.9%, Alex Net: 98.0% and 96.1%, VGG16: 98.0% and 96.1%, VGG19: 99.0% and 96.9%, ResNet50: 99.0% and 97.7%, and ResNet101: 99.0% and 98.4%, GoogLeNet: 98.0% and 96.9%, MobileNet-v2: 98.0% and 97.7%. A confusion matrix was created using 20% of the secure and unsecure image data to measure the trained CNN models' prediction accuracy.

The confusion matrix for each model is shown in Figure 5.7, with true positive (TP), false positive (FP), false negative (FN), and true negative (TN) values. The number of results that properly identified the positive class as positive is known as True Positive (TP), whereas the number of results that correctly classified the negative class as negative is known as True Negative (TN). False Positive (FP) indicates how many times the classifier categorized the negative class as positive, whereas False Negative (FN)

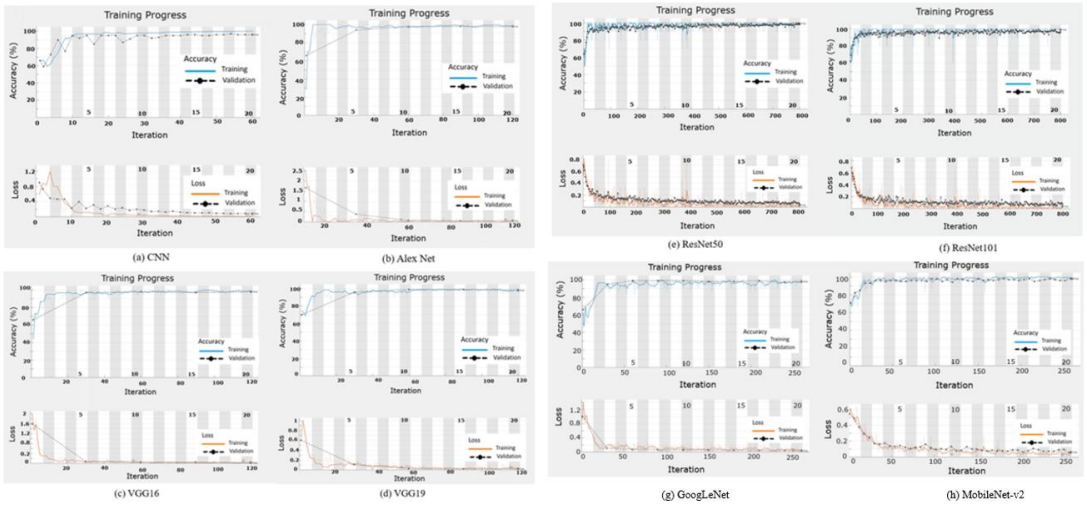

Figure 5.6 Training progress chart for (a) CNN, (b) Alex Net, (c) VGG16, (d) VGG19, (e) ResNet50, (f) ResNet101, (g) GoogLeNet, and (h) MobileNet-v2.

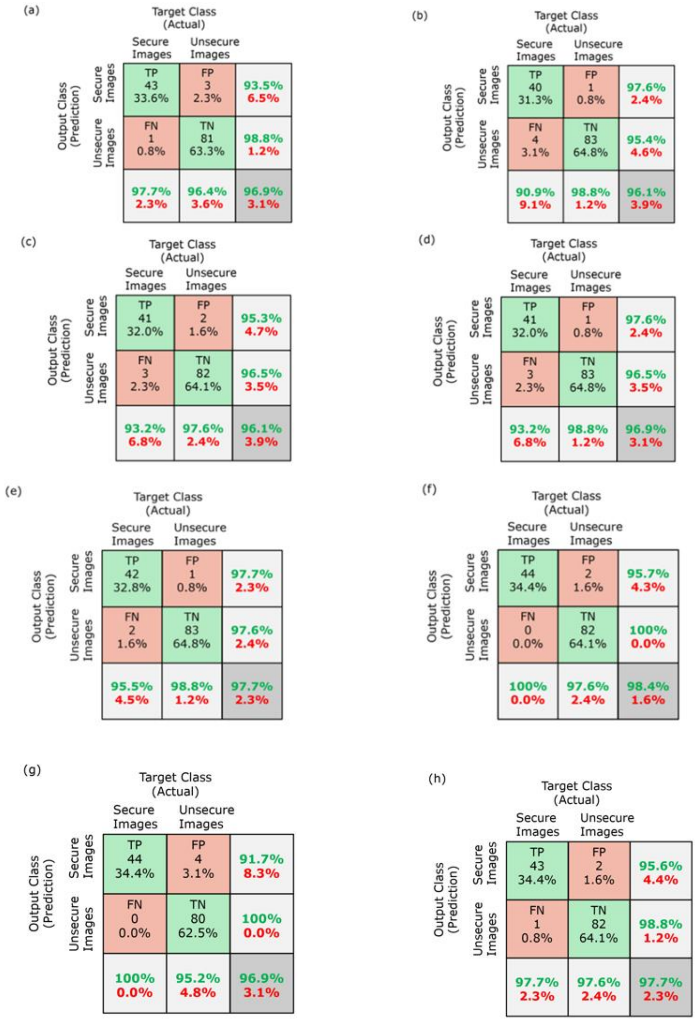

Figure 5.7 Confusion Matrix for (a) CNN, (b) Alex Net, (c) VGG16, (d) VGG19, (e) ResNet50, (f) ResNet101, (g) GoogLeNet, and (h) MobileNet-v2.

indicates how many times the classifier classed the positive class as negative. A basic CNN model with TP=43, FN=1, FP=3, and TN=81 is shown in Figure 5.7a.

In the first two diagonal cells of Figure 5.7a, the trained network's number and percentage of accurate classifications are displayed. Row1-Column1 indicates that 43 secure images are accurately classified as secure images, whereas Row2-Column2 indicates that 81 unsecure images are correctly classed as unsecure images. Row1-Column2 reveals that three of the secure images are mistakenly labeled as unsecure, resulting in a 2.3 percent false-positive rate over the whole dataset of 128 images.

Similarly, Row2-Column1 demonstrates that one of the unsecured images is mistakenly labeled as secure, resulting in a 0.8 percent false-negative rate. Row1-Column3 demonstrates that 93.5 percent of 46 secure images are correct, while 6.5 percent are wrong. Row2-Column3 reveals that 98.8% of the 82 secure images are correct, whereas 1.2 % are incorrect. Out of 44 secure images, 97.7% are accurately predicted as secure, while 2.3 percent are correctly predicted as unsecure. Row3-Column2 reveals that 96.4 % of 84 secure images are accurately predicted as secure, while only 3.6 % are correctly predicted as unsecure. Overall, 96.9% of the predictions are correct, whereas 3.1 percent are incorrect, according to Row3-Column3. Figures 5(b)-(h) demonstrate how AlexNet, VGG16, VGG19, ResNet50, ResNet101, GoogLeNet, and MobileNet-v2 explain their respective confusion matrices.

Table 5.2 Overall comparison of each deep leaning model's performance.

Model	**Precision (TP/(TP+FP))**	**Recall (TP/(TP+FN))**	**Prediction Accuracy ((TP+TN)/(TP+FP+TN+FN))**	**F1-Score (2TP/(2TP +FP+FN))**	**Training Accuracy**	**Testing Accuracy**
CNN	0.935	0.977	96.9%	0.955	97%	96.9%
Alex Net	0.975	0.909	96.1%	0.941	98%	96.1%
VGG16	0.953	0.931	96.1%	0.942	98%	96.1%
VGG19	0.976	0.931	96.9%	0.953	99%	96.9%
ResNet50	0.976	0.954	97.7%	0.965	99%	97.7%
ResNet101	0.956	1	98.4%	0.977	99%	98.4%
GoogLeNet	0.9167	1	96.8	0.956	98%	96.9%
MobileNet-v2	0.955	0.977	97.6%	0.966	98%	97.7%

Table 5.2 shows the overall comparison of our deep learning models and their accuracies. Precision and recall are two metrics used to assess a categorization or information retrieval system's performance. In general, recall (or sensitivity) indicates the proportion of recovered samples found among all relevant samples, whereas precision (or positive predictive value) represents the fraction of relevant samples discovered among the retrieved samples. For a perfect classifier, precision and recall are both equal. If the

model is near to 1, it is better. ResNet101 has the greatest true positive and true negative values among the eight models in the confusion matrix, indicating that it is a superior match. One of the most important assessment measures in machine learning is the F1 score. It works with an imbalanced dataset in which the number of observations for each class in a classification dataset is not equal, and it adjusts for false positives and negatives.

In most real-world classification problems, imbalanced class distribution exists, and the F1 score is a preferable tool for assessing those models. Even in our scenario, we have an imbalanced dataset, hence the model's prediction accuracy is calculated using the F1 score. Our transfer learning model has attained the greatest training accuracy of 99 %, while testing accuracy ranges from 96 to 98 %. A basic CNN model has a respectable overall performance and can predict data with near-perfect accuracy. To avoid data overfitting, it's best to apply the transfer learning approach to create a robust CNN model that can distinguish between genuine and defective ICs images.

5.8 Conclusion

Finally, we successfully showed an unique THz testing approach based on deep learning for the non-destructive and unobtrusive detection and classification of genuine and counterfeit, damaged, or forged integrated circuits. We first measured the circuit response to terahertz and sub-terahertz radiation at the circuit pins to construct a comprehensive IC signature map. A more thorough THz response profile may be generated by monitoring a larger number of pins at several frequencies and polarizations of terahertz radiation, resulting in enhanced classification accuracy. The proposed

technique has no impact on the operation of the IC. To achieve ultimate IC identification, we developed a CNN-based failure detection approach. We also explored at whether transfer learning may help IC detection networks perform better. Despite the wide range of realistic and THz IC images, the CNN model and fully trained CNNs found that knowledge transfer from realistic to THz IC images is viable. When we do not have any access to large volumes of labeled training data, transfer learning becomes a feasible choice for CNN training. With 99% training accuracy, 96 % to 98% testing accuracy, and 0.977 F1 scores, the convolution neural network was used to assess the classification process between secure and unsecure IC images. The accuracy of the transfer learning model may be improved further by fine-tuning the hyperparameter. Varied measurement approaches may be employed to establish terahertz signatures of individual ICs under different polarizations, frequencies, and depths of focus.

CHAPTER 6 TERAHERTZ METAMATERIALS AND FREQUENCY SELECTIVE SURFACE

6.1 Introduction

A range of subwavelength artificial micro/nanostructures make up metamaterials and their 2D equivalents, metasurfaces. They have sparked a lot of curiosity because of their incredible ability to manipulate external light [200]–[203]. Plasmonic metamaterials are composite arrays of artificially designed building blocks that use collective oscillations of electron subwavelength structures to trigger the desired electromagnetic response over the frequency range [204]–[209]. These artificial subwavelength structures excel in capturing and controlling electromagnetic interactions in the near field. Plasmonic metamaterials have gained a lot of interest in the photonics field during the last few decades. Metamaterials have been widely used as a robust photonic tool for a variety of applications, including super lensing [210], negative index media [211], [212], biochemical sensors [213], [214], ultrasound detectors [215], metamaterial absorbers [216], [217], and reconfigurable metadevices [218], [219] for various spectral ranges.

Toroidal moments are a new family of non-radiative plasmonic resonant modes based on magnetic currents that was recently discovered [220], [221]. In metasurfaces, a toroidal dipole can be utilized to produce high-Q resonances in a new method. Unlike ordinary multipoles, the intensity of the toroidal dipole interaction is determined by the time derivative of the surrounding electric field. Tightly constrained loops of oscillating magnetic field curl around the fictitious arrow of the toroidal dipole vector are a characteristic feature of toroidal dipoles. A toroidal dipole resonance occurs when the

magnetic moments of the current caused by incoming radiation on the surface of a torus are aligned head-to-tail to form a dynamic vortex. In well-engineered 3D and planar metamolecules, toroidal dipole resonances with high quality factors (Q factor), long dephasing times (τ), and high scattering intensity have been successfully demonstrated [221]–[223].

Toroidal moments are readily masked by the radiation pattern of strong classical EM multipoles because they reflect weak far-field radiation footprints. Despite the difficulty of detecting toroidal excitation, well-designed metamolecules can enhance toroidal dipole response. The magnetic field inside the metamolecule must be confined into tight oscillatory loops, and electric and magnetic dipoles and quadrupoles must be suppressed to induce toroidal excitation. The discovery of resilient toroidal modes will pave the way for high Q factor devices due to their weak scattering of electromagnetic radiation compared to their electrical and magnetic counterparts. Meta-photonic devices are failing to find practical applications due to inherent non-radiative and radiative losses, despite their immense promise in real-world applications. At microwave and terahertz frequencies, nonradiative losses are less substantial, but radiative losses can have a considerable impact on metamaterial device performance, leading in a decline in metamaterial quality (Q) factors [224]. Metamaterial allows for tailoring loss channels, making it a viable method for implementing toroidal excitations in the terahertz range. Toroidal excitations have the potential to reduce radiative losses and thereby enhance device performance [225].

6.2 Toroidal Dipole and related works of Toroidal Response in Terahertz range

In the microwave frequency, the first toroidal dominated response was achieved utilizing a 3D design of four split-ring resonators (SRRs) in a unit cell [221]. Theoretical study later suggested that by scaling the unit cell geometry, the toroidal response might be attained at far-infrared wavelengths [226]. However, at optical wavelengths, fabricating 3D structures to measure toroidal dipolar moments is difficult. Further research has been conducted to reduce the designs into planar structures [227], and the observation of toroidal responses has been extended to terahertz [228], [229] and optical regimes [226], [230]. Simple shapes have been investigated for manufacturing feasibility, including bars [231], disks [232], ring-shaped grooves [233], core-shell nanoparticles [234], oligomer structure [235], core-shell nanowires [236], and hybrid nanostructure [237].

Plasmonic toroidal moments are increasingly being exploited in nanophotonic device development, specifically for switching and biochemical detection [238], [239]. In the THz domain, however, the coupling of several toroidal resonators has yet to be thoroughly investigated. Toroidal resonance coupling in the core alone, shell only, and both core-shell at THz frequencies is investigated using a planar nanomatryoshka type core-shell resonator structure. The function of multiple toroidal resonator coupling is also demonstrated. This design may be used to modify the strength of toroidal resonances that have been identified as a result of the strong multifold near-field magnetic coupling across the unit cells. Transmission mode time-domain THz spectroscopy is used to experimentally evaluate the observed couplings of toroidal modes for the core-shell

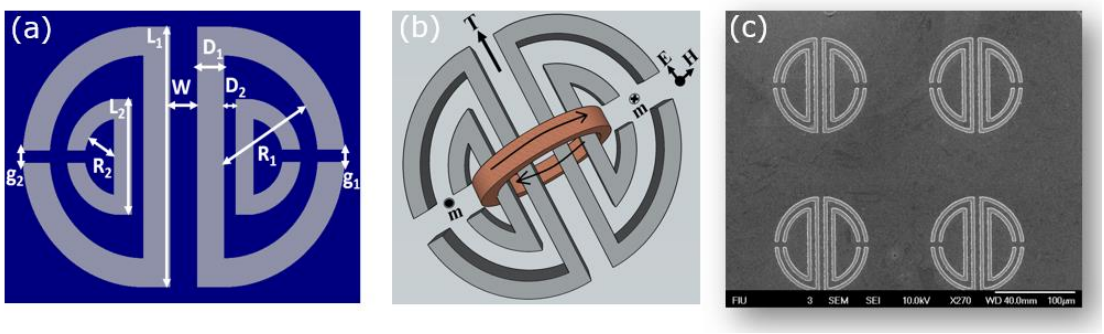

Figure 6.1 (a) Schematic representation with specified geometrical parameters, (b) 3D rendering view with the polarization of the incident THz beam (m—showing the direction of magnetic moment; E & H—electric and magnetic field of incident THz beam; and T—toroidal moment), and (c) SEM image of toroidal metamolecule.

structure in this study. The suggested design has also been used to demonstrate toroidal hybridization concepts utilizing magnetic current oscillations. Toroidal hybridization develops in a metallic nanostructure when the electromagnetic interaction between free plasmons causes the plasmon energy to split and shift. We are the first to study the hybridization nature of the toroidal resonance response, to our knowledge.

6.3 Materials and Methods for Hybrid Toroidal Resonance Response in Planar Core-Shell Structure

Figure 6.1a and 6.1b shows the polarization of the incoming THz beam, and a schematic representation of the examined planar core-shell THz metasurface unit cell (not in size). The proposed core-shell design has been fabricated by a single step photolithography process on an undoped high resistivity silicon (HR-Si) substrate (500-µm-thick, resistivity ρ>10 kΩ.cm and crystal orientation of <100>). The wafer was cleaned with acetone and isopropanol before being coated with a negative photoresist (NLOF 2020) and UV lithography patterned. We deposited 350 nm of aluminum using electron-beam evaporation at a vacuum pressure of ~ 3.2×10^{-6} mTorr. The sample was soaked in acetone for 10–15 minutes at room temperture using the sonication bath for

metal lift-off. The JEOL 7000 instrument was used to create the SEM images displayed in Figure 6.1c.

A terahertz time-domain spectrometer (THz-TDS) setup with a frequency step size of 10 GHz was used to measure the transmission spectrum of the fabricated devices. A commercially available finite-difference time-domain (FDTD) solver, Lumerical 2019, was utilized for numerical modeling, combined with custom numerical analysis codes. Perfectly matched layers (PMLs) with 64 layers were employed in the z-direction for the simulation setup, with periodic boundaries in the x- and y-directions. All simulations employed a spatial grid size of $\Delta x = \Delta y = \Delta z = 0.1$ μm. Electric field, magnetic field, and surface-current distribution monitors were utilized to collect the data after a broadband plane wave pulse was injected in the z-direction for THz radiation and transmission. The permittivity of a high resistive silicon substrate was calculated using a refractive index of ~ 3.64+i0.0001 for Si in the THz band [239]. Aluminum's frequency-dependent complex permittivity is equal to,

$$\epsilon(\omega) = \epsilon(\infty) - \frac{\omega_p}{\omega(\omega + i\Gamma)} \qquad \text{Eq. 6-1}$$

where plasma frequency $\omega_p = 2.243 \times 10^{16}$ rad s^{-1} and damping rate $\Gamma = 1.2434 \times 10^{14}$ rad s^{-1} [240].

6.4 Results and Discussion for Hybrid Toroidal Resonance Response in Planar Core-Shell Terahertz Metasurfaces

The After several numerical investigations and device geometry optimization, the geometrical parameters of the core-shell structure have been finalized [241]. The STTM cluster's geometrical parameters are R1=60 μm, R2=35 μm, W=5 μm, D1=4 μm, D2=4

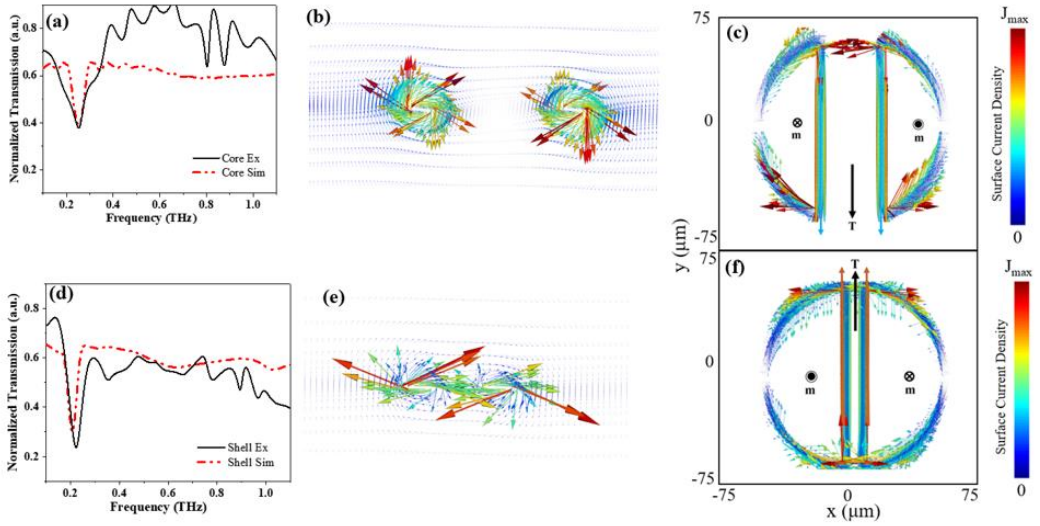

Figure 6.2 (a) Simulated and experimental transmission versus frequency spectra, (b) vectorial B field, and (c) surface current distribution (j) for core at 0.259 THz. (d) Simulated and experimental transmission versus frequency spectra, (e) vectorial B field, and (f) surface current distribution (j) for shell at 0.212 THz. The red arrows in (c) and (f) show the direction of the current (j) in the center strip of the resonators.

μm, L1=120 μm, L2=100 μm, g1=6 μm, g2=6 μm. In all simulations and experiments, a y-polarized incident THz beam was delivered on the devices, parallel to the unit cell's symmetric blocks but perpendicular to the capacitive gap illustrated in Figure 6.1b. Figure 6.2 a and d show the normalized transmission amplitude spectra for the core and shell resonators (simulated: dashed red curves and experimentally measured: solid curves), and the vectorial magnetic field distribution ((6.2b) and (6.2e)) and the surface current distribution ((6.2c) and (6.2f)). The transmission spectra predicted by FDTD for the core resonator exhibit a minimum at 0.259 THz (Figure 6.2a) and the shell resonator exhibit a minimum of 0.212 THz (Figure 6.2d).

The surface current analysis demonstrates that the current (j) on the semicircle's central axis flows in the same direction, producing magnetic fields in the loop's center that are in the opposite direction. Magnetic fields are oriented head-to-tail as shown in Figure 6.2c and 6.2f, resulting in a toroidal dipole moment (T) in the y-direction. The

incoming THz beam excites local modes in both circumstances, resulting in circular magnetic fields at the center and significant suppression of the electric dipole moment by the stimulated toroidal resonances [228], [242]. Integrating the scattered magnetic and incoming electromagnetic fields yields the total transmitted magnetic radiation from magnetoplasmonic unit cell arrays. The magnetic (m_c) and toroidal (T_c) dipolar moments can be defined as [220], [237]:

$$\boldsymbol{m_c} = \frac{1}{2c}\int (\boldsymbol{r} \times \boldsymbol{J})\, d^3\boldsymbol{r}$$
$$\boldsymbol{T_c} = \frac{1}{10c}\int [(\boldsymbol{r}.\boldsymbol{J})\boldsymbol{r} - 2r^2\boldsymbol{J}]\, d^3\boldsymbol{r} \qquad \text{Eq. 6-2}$$

where J is the induced current density over the entire volume of the area and c is the light's conventional speed.

Using the minima of the induced toroidal dipolar features, we derived the appropriate theoretical Q-factors for the simulated spectra as $Q_{T,sim}^{core}$ =5.8 and $Q_{T,sim}^{shell}$=8 for the toroidal modes in core and shell resonators, respectively. The experimentally measured curves closely match the theoretically predicted curves, especially for the core resonator, whereas the shell resonator has a minor disagreement. The shell resonator's observed spectrum reaches a minimum at 0.224 THz. The modest discrepancy might be due to a little variation between the material's real optical properties and those utilized in simulations, and environmental conditions like as humidity, which could have a significant impact on terahertz propagation. In the experimental scenario, the losses resulted in a significant loss of resonance and a drop of the measured quality factors to $Q_{T,exp}^{core}$=3.5 and $Q_{T,exp}^{shell}$=4.6 for the core and shell resonators, respectively.

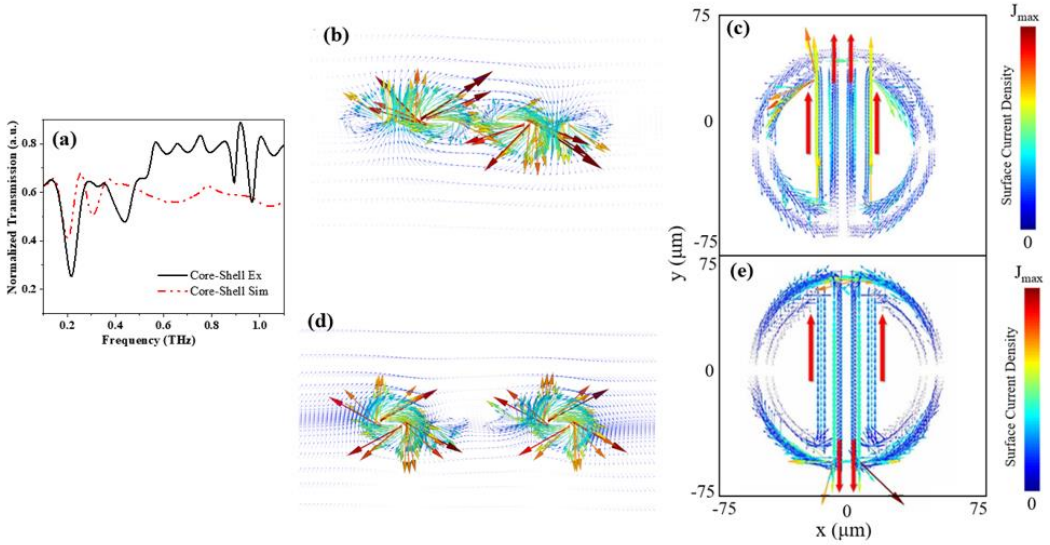

Figure 6.3 (a) Simulated and experimental transmission versus frequency spectra for core-shell, (b) vectorial B field, and (c) surface current distribution (j) for core-shell at 0.202 THz, and (d) vectorial B field, and (e) surface current distribution (j) for core-shell at 0.308 THz

6.5 Toroidal Hybridization Concepts of the Proposed Planar Core-Shell Terahertz Metasurfaces

The array of nanomatryoshka unit cells that integrate core and shell resonators (Fig. 6.1c) was then numerically and experimentally studied. With quality factors of $Q_{T,sim}^{c-s1}$ =4.5 and $Q_{T,sim}^{c-s2}$=5.9, the numerically predicted transmission spectra shown in Fig. 6.3a (dashed curve) indicate two substantial minima at 0.202 THz and 0.308 THz, respectively. In both core and shell resonators, the current (j) on the semicircle's central axis flows in the same direction, resulting in magnetic fields in the opposite direction at the loop's center for the first minima, according to the surface current analysis (Fig. 6.3b). Figure 6.3c depicts the vectorial magnetic field distribution, demonstrating that magnetic fields are in a head-to-tail pattern, forming toroidal dipole moments (T) in the y-direction for both resonators. At the second minimum at 0.308 THz, the current (j) on the central axis of the semicircles in core and shell resonators flows in opposite directions in an anti-

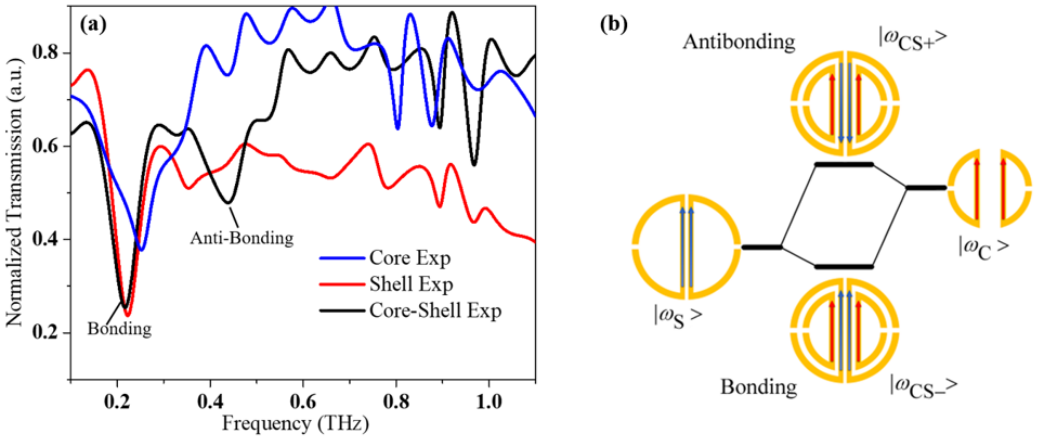

Figure. 6.4 (a) Experimental transmission spectra for core-shell, core, and shell structures and (b) an energy level diagram, describing the interaction between the core and shell plasmon resonances based on the surface current distribution, resulting in the hybrid plasmon resonance of a concentric core-shell nanomatryoshka structure.

symmetric pattern. This resonance mode also yields head-to-tail magnetic fields and toroidal moments, but in a opposite directions.

The vectorial sum of both is the net toroidal moment. The experimental transmission spectra for the core-shell, core, and shell architectures are shown in Figure 6.4 a. The coupled coreshell resonators, as predicted by the numerical calculations, have two shifted minima at 0.214 THz and 0.439 THz, with quality factors of $Q_{T,exp}^{cs1}$= 4.2 and $Q_{T,exp}^{cs2}$ = 6.2, respectively. A hybridization model like the one described for localized surface plasmons previously in [243] can explain the behavior of the core-shell structure. The plasmon hybridization model depicts the collective plasmon oscillation process of conduction electrons in core-shell metallic nanoparticles in an intuitive pictorial manner. The atomic molecular orbital theory is used to understand the energy distribution of nanoparticles by giving bonding and antibonding combinations, i.e., hybridization of the individual nanoparticle plasmon. The plasmon hybridization model describes plasmon resonances in metal-based nanostructures as a collection of plasmons from simpler

geometries that interact to form a "hybridized" system. By splitting and shifting the plasmon energy, the electromagnetic interaction between free plasmons in a metallic nanostructure can lead to hybridization. The plasmon hybridization model is usually described using the charge distribution analysis of nanoparticles.

In our case, we have followed the concept of plasmon hybridization theory to interpret our planar core-shell nanostructure hybridization utilizing the magnetic current oscillations. The geometry-dependent resonance response can be observed in the core-shell structure as an interaction between the two components fixed frequency plasmon response. This interaction results in producing two hybrid toroidal resonance modes: (a) bonding mode (|ωCS−>): lower energy symmetric current distribution and (b) antibonding mode (|ωCS+>): higher energy anti-symmetric current distribution. The lower energy (bonding mode) of the core-shell structure is somewhat lower than the lower energy of the shell alone structure, as shown in Fig. 6.4a, but the higher energy (antibonding mode) of the core-shell structure is much greater than the higher energy of the core only structure. Figure 6.4 b depicts the toroidal hybridization scheme, which uses the bonding ((|ωCS−>) and antibonding (|ωCS+>) modes to explain the core-shell resonator transmission spectra. The proposed device energy distribution is defined by the magnetic current oscillations depicted by the arrows on the center axis in the figure, rather than the charge distribution utilized in the plasmon hybridization model. The bonding and antibonding modes can be used to support our assertion of toroidal hybridization in our planar core-shell configuration. The toroidal hybridization concept may be used to anticipate and characterize the toroidal resonance response of composite metallic nanostructures with higher geometrical complexity.

6.6 Frequency selective surface-based Terahertz bandpass filter

Any thin, repetitive surface intended to reflect, transmit, or absorb electromagnetic fields dependent on the frequency of the field is known as a frequency-selective surface (FSS). FSS is a frequency selective structure of identical planar structures that act as an EM filter. FSS and metamaterials with different designs and orientations have various features and phenomena. FSS structure and the constituents of metamaterials are the primary differences between them. The type of application, such as reflection or transmission in a certain frequency range or absorption in a specific frequency range, influences the choice of FSS and metamaterials.

Here, a frequency-selective, tunable THz bandpass filter is designed and numerically investigated using a stretchable and flexible elastomer with metallic nanostructures. The proposed structure offers bandpass filters with linewidths of 23 GHz and 170 GHz at 0.15 THz and 0.825 THz, respectively, according to comprehensive numerical studies. The THz filter presented is polarization-independent and has a simple and compact structure.

Tunable or electronically reconfigurable filters are becoming increasingly popular due to their ability to cover a vast bandwidth range without requiring a complex structure. Using a flexible elastic polymer substrate instead of a rigid substrate to meet this tremendous need for flexible technologies has caught on. These substrates' flexibility and stretching allow for a wide range of applications in the MW, visible, and THz spectrum. Flexible polymers with high THz transmission and low loss, such as poly(dimethylsiloxane) (PDMS) [204], [244], [245], poly (3,4-ethylene dioxythiophene) polystyrene sulfonate (PEDOT: PSS) [246]–[248], high-density polyethylene (HDPE)

[249], polyimide [250], and polyethylene terephthalate (PET) [251]–[253], have emerged as ideal candidates for THz frequency selective surface (FSS) substrate materials. THz FSSs based on flexible substrates have recently been rapidly utilized for biosensing, filtering, and absorbers [254]–[258]. Electronic devices manufactured on a flexible, foldable, and stretchable substrate could be the first step toward novel electronic applications [259]. Various research on applying these flexible elastomer substrates has been performed [250], [260]–[267]. Flexibility and folding do not necessitate a great deal of stress and strain. However, when it comes to stretchability, the ability to absorb a large amount of strain without fracture or deformation, and significant loss in electrical and photonic properties, is required. Designing a stretchable flexible substrate while keeping the electrical and optical features of the devices is incredibly challenging. Stretching the flexible polymer substrate has dramatically shifted the Plasmon resonant frequency in several frequency ranges (optical, MW, GHz-THz range), according to various studies [204], [244], [245], [266]–[270]. However, building a stretchable and flexible substrate in high-frequency ranges, such as MW, millimeter, and THz, can be difficult because of their weakly sensitive unit cell response but with precise design and consideration, these problems can be overcome.

6.7 Materials and Methods for Terahertz bandpass filter

A highly adjustable filter design is proposed based on metal nanoparticles embedded in an elastomer layer. According to our comprehensive numerical analysis, the filter with gold nanoparticles in PDMS provides a band-pass filter in the spectrum region of 0.1 to 2 THz. Even when the polymer substrate is stretched under mechanical strain, the gold

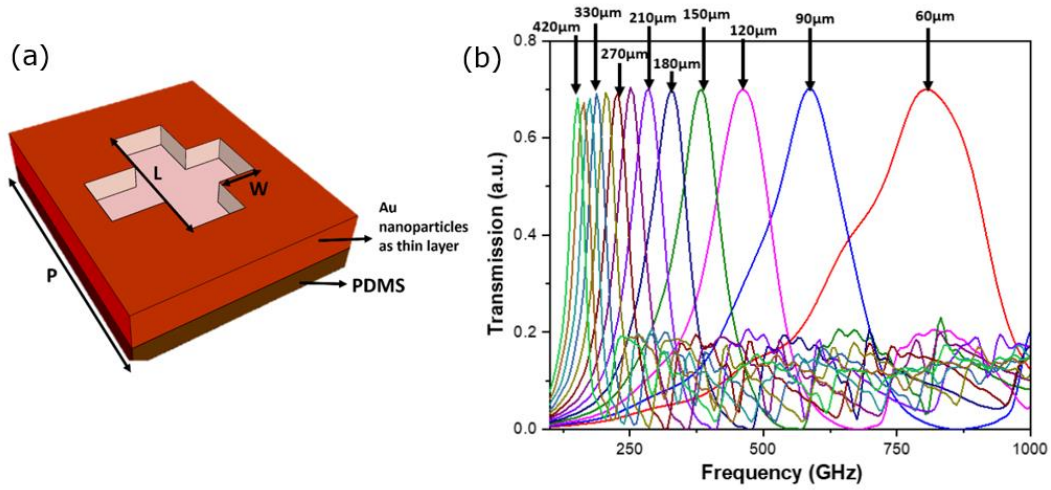

Figure 6.5. Schematic representation of the (a) unit cell of the THz bandpass filter structure and specified geometrical parameters and (b) Transmission spectrum of the proposed filter structure from 100 to 1000 GHz based on the periodicity P=420µm, 390µm, 360µm, 330µm, 300µm, 270µm, 240µm, 210µm, 180µm, 150µm, 120µm, 90µm and 60µm.

nanoparticles will collectively behave like a thin film layer and create the desired filter pattern. The polymer substrate's stretchability enables fine-tuning of the feature size and, as a result, the filter frequency, depending on the applied mechanical strain. The proposed filter is low-cost, readily scalable for the desired frequency range, and simple to design. The conformal surface's mechanical flexibility and ease of implementation allow for a wide range of size options while maintaining electrical and optical qualities. We first chose a poly(dimethylsiloxane) (PDMS) substrate as shown in fig. 6.5(a) that allows for stretchable electronics based on our objectives [267], [271]. We chose the cross-slot shape as our THz filter because of its simple design and cost-effective one-step fabrication procedure [271], [272]among the several frequency selective surfaces (FSS) based structures available. The empirical formula [273] below can be used to estimate the center frequency of the filter:

$$\lambda = 1.8 \times L - 1.3 \times W + 0.2 \times P \qquad \text{Eq. 6-3}$$

where L is the cross-arm length, W is the cross-arm width and P is the periodicity of the unit cell. We investigated the suitable filter structure using the numerical optimization procedure, with the period, P, fixed and L and W varying as L=0.8×P and W=0.1×P, respectively, and the nanoparticle thickness as 2μm.

Later, we utilized poly (3,4-ethylenedioxythiophene) polystyrene sulfonate (PEDOT:PSS) on a PDMS substrate with and without embedded Au nanoparticles to improve the performance as shown in fig. 6.6(a) and (b). This new design concept can maintain optical characteristics despite undergoing deformation. We have chosen PEDOT: PSS for its high electrical conductivity (~1362 Scm^{-1}), high transparency (≈88 %) and mechanical elasticity (≈ 1.2 GPa) characteristics.

Table 6.1. Terahertz bandpass filter parameters

Period (P)	Length (L)	Width (W)	Center frequency (fc) GHz	FWHM (GHz)	Transmission (%)
90	81	22.5	1630	900	65
120	108	30	1240	670	67
150	135	37.5	1000	590	72
180	162	45	830	500	72.5
210	189	52.5	700	355	74
240	216	60	620	345	75.2
270	243	67.5	540	285	77.5
300	270	75	490	235	76.8
330	297	82.5	450	240	79.1
360	324	90	410	220	79.2
390	351	97.5	370	200	80
420	378	105	350	150	78.9

6.8 Results and Discussion for Terahertz bandpass filter

We numerically examined and optimized the proposed structure for width, length, period, and polymer thickness to finalize the device characteristics. From 100 GHz to 1000 GHz, the transmission characteristic of the proposed filter design was investigated. The frequency of the filter is greatly influenced by parameters value (Period, length, and

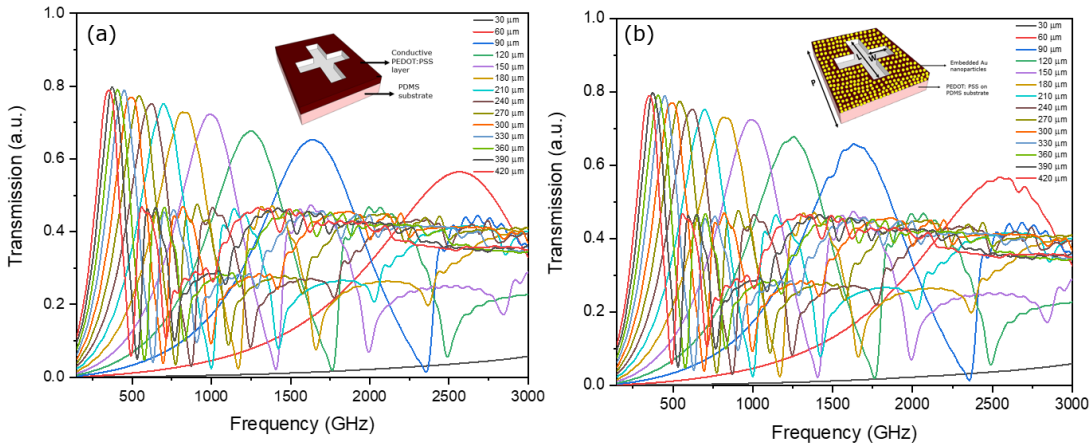

Figure 6.6. Transmission spectrum of the proposed filter structure from 100 to 3000 GHz based on the periodicity P=420µm, 390µm, 360µm, 330µm, 300µm, 270µm, 240µm, 210µm, 180µm, 150µm, 120µm, 90µm, 60µm and 30 µm (a) without embedded au nanoparticles and (b) with embedded au nanoparticles.

width). As the periodicity or structure of the proposed filter decreases, the transmission bands right shifted. The frequency range can significantly affect by even minor fractional changes in parameter values. The frequency range can significantly affect by even minor fractional changes in parameter values. The numerically derived transmission spectrums vs frequency is shown in Figure 6.5b. Spectral resolution is determined by the filter structure. In the investigated spectral range, the narrowest linewidth (Full width half maximum, FWHM) is 23 GHz at 0.15 THz for a periodicity of 420 µm, while the highest linewidth is 170 GHz at 0.825 THz for a periodicity of 60 µm. Table-6.1 shows the entire parameters and their corresponding transmission (%) values.

We numerically examined and optimized the proposed structure for width, length, period, and polymer thickness to finalize the device characteristics. From 100 GHz to 1000 GHz, the transmission characteristic of the proposed filter design was investigated. The frequency of the filter is greatly influenced by parameters value (Period, length, and width). As the periodicity or structure of the proposed filter decreases, the transmission bands right shifted. The frequency range can significantly affect by even minor fractional

changes in parameter values. The frequency range can significantly affect by even minor fractional changes in parameter values. The numerically derived transmission spectrums vs frequency is shown in Figure 6.5b. Spectral resolution is determined by the filter structure. In the investigated spectral range, the narrowest linewidth (Full width half maximum, FWHM) is 23 GHz at 0.15 THz for a periodicity of 420 μm, while the highest linewidth is 170 GHz at 0.825 THz for a periodicity of 60 μm. Table-1 shows the entire parameters and their corresponding transmission (%) values.

PEDOT: PSS on a PDMS substrate without and with incorporated Au nanoparticles were also numerically analyzed and the transmission spectrums versus the frequency of the proposed filter design are shown in figure 6.6a and 6.6b as a proof-of-principle using the three-dimensional (3D) finite-difference time-domain (FDTD) method (Lumerical 2018) software [64]. To achieve the best possible results, the special grid sizes in all three axes were set to 25nm and periodic boundary condition was set to x and y-axis while in z-axis perfectly matched layer has been used. The light source was a x-polarized linear plane wave with a pulse length of 100psas shown in. We have observed a significant improvement in the frequency spectral range for PEDOT: PSS on a PDMS substrate than PDMS substrate only. Although no substantial differences in transmission have been obtained for with and without embedded Au nanoparticles. But Au nanoparticles embedded structures will be a feasible candidate for biological sample sensing applications because to their biocompatibility, optical and electrical features, and relative ease of fabrication and modification.

The strength of our approach lies in innovative combination with the mechanical stretching and flexible nature of the substrate along with gold nanoparticles which will

behave like a thin film based on the applied mechanical stress. Based on the applied elongation force the elastomer substrate is maintaining its elastic limit and elasticity in corresponds with the electrical and optical properties of the filter and tune its frequency accordingly. More study is needed to investigate the feasibility and fabrication process of identifying the best polymer substrate to improve the performance of the filter indicated above. Although some of the concepts may not be completely compatible with the chosen polymer substrate due to fabrication issues, they have the potential to significantly enhance future process and component designs.

6.9 Conclusion

In summary, we have presented here two different structures and methods, one using metamaterials and another using frequency selective surface, and both has a potential in advanced terahertz technology. The proposed planar core-shell structure and terahertz bandpass filter can find application in almost all fields of science and technology including but not limited to THz technology, bio/chemical analysis, embedded bio sensing, and astrophysics.

The planar nanomatryoshka type core-shell resonator exhibits hybrid toroidal resonance modes at THz frequencies and the resonance response of the device is very geometry sensitive, and by modifying the device design, the resonance response may be blue and red-shifted, making it highly tunable. The proposed design can also be utilized to investigate the Fano resonance response by breaking the device's symmetry. This study might open the way for new applications in advanced THz photonics, including precise bio-sensing, fast switching, narrow-band filters and modulation, diagnostic instruments,

data storage, polarization twisting, near-field lasing, and lasing spacer. Terahertz toroidal plasmonic metasurfaces can provide accurate screening and detection of various biomarkers due to considerable field confinement at subwavelength geometries [241], [274]. The potential of utilizing terahertz spectroscopy for early detection of COVID-19 was also investigated using the toroidal resonator in [275]–[277]. Although terahertz-based biosensing techniques have been used in various domains [278], [279], further research on SARS CoV-2 and similar viruses is required. The SARS-CoV-2 outbreak is now sweeping the globe. To prevent current and future pandemics, terahertz might be a fantastic method to solve the urgent need for label-free, selective, repeatable, cost-effective, phase-sensitive, and rapid detection technologies.

The THz band pass filter can find its applications in communications (emerging 5G or beyond), sensing, imaging, spectroscopy, and other scientific and research fields.

CHAPTER 7 FUTURE DIRECTIONS

In this thesis, we have explored different materials such as graphene, p-diamond and n-diamond to find the most suitable materials for high power and high temperature terahertz detector devices. Both theoretically and analytically, we investigated p-diamond and n-diamond materials. However, we have not delved into the diamond fabrication process. Fabrication of diamond material could be tricky due to its small substrate size. The experimental results of diamond devices could open up a new horizon to design and fabricate a more robust diamond THz FET for future application arena.

References

[1] A. Y. Pawar, D. D. Sonawane, K. B. Erande, and D. v. Derle, “Terahertz technology and its applications,” *Drug Invention Today*, vol. 5, no. 2, pp. 157–163, Jun. 2013, doi: 10.1016/J.DIT.2013.03.009.

[2] D. Arnone, C. Ciesla, and Michael Pepper, “Terahertz imaging comes into view,” *Physics World*, vol. 13, no. 4, p. 35, Apr. 2000, doi: 10.1088/2058-7058/13/4/24.

[3] A. G. Markelz, A. Roitberg, and E. J. Heilweil, “Pulsed terahertz spectroscopy of DNA, bovine serum albumin and collagen between 0.1 and 2.0 THz,” *Chemical Physics Letters*, vol. 320, no. 1–2, pp. 42–48, Mar. 2000, doi: 10.1016/S0009-2614(00)00227-X.

[4] M. Walther, B. Fischer, M. Schall, H. Helm, and P. U. Jepsen, “Far-infrared vibrational spectra of all-trans, 9-cis and 13-cis retinal measured by THz time-domain spectroscopy,” *Chemical Physics Letters*, vol. 332, no. 3–4, pp. 389–395, Dec. 2000, doi: 10.1016/S0009-2614(00)01271-9.

[5] H.-B. Liu *et al.*, “Detection and identification of explosive RDX by THz diffuse reflection spectroscopy,” *Optics Express, Vol. 14, Issue 1, pp. 415-423*, vol. 14, no. 1, pp. 415–423, Jan. 2006, doi: 10.1364/OPEX.14.000415.

[6] D. M. Mittleman, J. Cunningham, M. C. Nuss, and M. Geva, “Noncontact semiconductor wafer characterization with the terahertz Hall effect,” *Applied Physics Letters*, vol. 71, no. 1, p. 16, Jun. 1998, doi: 10.1063/1.119456.

[7] M. Yamashita, K. Kawase, C. Otani, T. Kiwa, and M. Tonouchi, “Imaging of large-scale integrated circuits using laser-terahertz emission microscopy,” *Optics Express*, vol. 13, no. 1, p. 115, Jan. 2005, doi: 10.1364/opex.13.000115.

[8] K. Kawase, M. Yamashita, M. Tonouchi, and T. Kiwa, “Laser terahertz-emission microscope for inspecting electrical faults in integrated circuits,” *Optics Letters, Vol. 28, Issue 21, pp. 2058-2060*, vol. 28, no. 21, pp. 2058–2060, Nov. 2003, doi: 10.1364/OL.28.002058.

[9] S. D. Ganichev, E. Ziemann, I. N. Yassievich, V. I. Perel, and W. Prettl, “Characterization of deep impurities in semiconductors by terahertz tunneling ionization,” *Materials Science in Semiconductor Processing*, vol. 4, no. 1–3, pp. 281–284, Feb. 2001, doi: 10.1016/S1369-8001(00)00120-7.

[10] W. Zhang, A. K. Azad, and D. Grischkowsky, “Terahertz studies of carrier dynamics and dielectric response of n-type, freestanding epitaxial GaN,” *Applied Physics Letters*, vol. 82, no. 17, p. 2841, Apr. 2003, doi: 10.1063/1.1569988.

[11] M. Shur, S. Rudin, G. Rupper, F. Dagefu, and M. Brodsky, “Tera FETs for terahertz communications,” *IEEE Photonics Newsletter, Vol 33*, pp. 4–7, 2019.

[12] I. F. Akyildiz, J. M. Jornet, and C. Han, “Terahertz band: Next frontier for wireless communications,” *Physical Communication*, vol. 12, pp. 16–32, Sep. 2014, doi: 10.1016/J.PHYCOM.2014.01.006.

[13] P. T. Dat, A. Kanno, N. Yamamoto, and T. Kawanishi, “Seamless convergence of fiber and wireless systems for 5G and beyond networks,” *Journal of Lightwave Technology*, vol. 37, no. 2, pp. 592–605, Jan. 2019, doi: 10.1109/JLT.2018.2883337.

[14] A. Yazgan, L. Jofre, and J. Romeu, “The state of art of terahertz sources: A communication perspective at a glance,” *2017 40th International Conference on Telecommunications and Signal Processing, TSP 2017*, vol. 2017-January, pp. 810–816, Oct. 2017, doi: 10.1109/TSP.2017.8076101.

[15] C. Jastrow, K. Münter, R. Piesiewicz, T. Kürner, M. Koch, and T. Kleine-Ostmann, “300 GHz transmission system,” *Electronics Letters*, vol. 44, no. 3, p. 213, 2008, doi: 10.1049/el:20083359.

[16] H.-J. Song *et al.*, “8 Gbit/s wireless data transmission at 250 GHz,” *Electronics Letters*, vol. 45, no. 22, p. 1121, 2009, doi: 10.1049/el.2009.2186.

[17] P. Pirinen, “A brief overview of 5G research activities,” *Proceedings of the 2014 1st International Conference on 5G for Ubiquitous Connectivity, 5GU 2014*, pp. 17–22, Feb. 2014, doi: 10.4108/ICST.5GU.2014.258061.

[18] M. Bauer *et al.*, “A High-Sensitivity AlGaN/GaN HEMT Terahertz Detector with Integrated Broadband Bow-Tie Antenna,” *IEEE Transactions on Terahertz Science and Technology*, vol. 9, no. 4, pp. 430–444, Jul. 2019, doi: 10.1109/TTHZ.2019.2917782.

[19] H. Hou, Z. Liu, J. Teng, T. Palacios, and S. J. Chua, “A sub-terahertz broadband detector based on a GaN high-electron-mobility transistor with nanoantennas,” *Applied Physics Express*, vol. 10, no. 1, p. 014101, Jan. 2017, doi: 10.7567/APEX.10.014101/XML.

[20] T. Watanabe *et al.*, “InP- and GaAs-based plasmonic high-electron-mobility transistors for room-temperature ultrahigh-sensitive terahertz sensing and imaging,” *IEEE Sensors Journal*, vol. 13, no. 1, pp. 89–99, Jan. 2013, doi: 10.1109/JSEN.2012.2225831.

[21] Y. Kurita *et al.*, “Ultrahigh sensitive sub-terahertz detection by InP-based asymmetric dual-grating-gate high-electron-mobility transistors and their

broadband characteristics," *Applied Physics Letters*, vol. 104, no. 25, p. 251114, Jun. 2014, doi: 10.1063/1.4885499.

[22] R. al Hadi *et al.*, "A 1 k-pixel video camera for 0.7-1.1 terahertz imaging applications in 65-nm CMOS," *IEEE Journal of Solid-State Circuits*, vol. 47, no. 12, pp. 2999–3012, 2012, doi: 10.1109/JSSC.2012.2217851.

[23] U. R. Pfeiffer, J. Grzyb, H. Sherry, A. Cathelin, and A. Kaiser, "Toward low-NEP room-temperature THz MOSFET direct detectors in CMOS technology," *International Conference on Infrared, Millimeter, and Terahertz Waves, IRMMW-THz*, 2013, doi: 10.1109/IRMMW-THZ.2013.6665522.

[24] S. Boppel *et al.*, "CMOS integrated antenna-coupled field-effect transistors for the detection of radiation from 0.2 to 4.3 THz," *IEEE Transactions on Microwave Theory and Techniques*, vol. 60, no. 12, pp. 3834–3843, 2012, doi: 10.1109/TMTT.2012.2221732.

[25] J. Zdanevicius *et al.*, "Field-Effect Transistor Based Detectors for Power Monitoring of THz Quantum Cascade Lasers," *IEEE Transactions on Terahertz Science and Technology*, vol. 8, no. 6, pp. 613–621, Nov. 2018, doi: 10.1109/TTHZ.2018.2871360.

[26] A. Lisauskas *et al.*, "Antenna-coupled field-effect transistors for multi-spectral terahertz imaging up to 4.25 THz," *Optics Express, Vol. 22, Issue 16, pp. 19235-19241*, vol. 22, no. 16, pp. 19235–19241, Aug. 2014, doi: 10.1364/OE.22.019235.

[27] K. Ikamas, D. Cibiraite, A. Lisauskas, M. Bauer, V. Krozer, and H. G. Roskos, "Broadband Terahertz Power Detectors Based on 90-nm Silicon CMOS Transistors with Flat Responsivity Up to 2.2 THz," *IEEE Electron Device Letters*, vol. 39, no. 9, pp. 1413–1416, Sep. 2018, doi: 10.1109/LED.2018.2859300.

[28] A. Zak *et al.*, "Antenna-integrated 0.6 THz FET direct detectors based on CVD graphene," *Nano Letters*, vol. 14, no. 10, pp. 5834–5838, Oct. 2014, doi: 10.1021/NL5027309/ASSET/IMAGES/MEDIUM/NL-2014-027309_0004.GIF.

[29] L. Vicarelli *et al.*, "Graphene field-effect transistors as room-temperature terahertz detectors," *Nature Materials 2012 11:10*, vol. 11, no. 10, pp. 865–871, Sep. 2012, doi: 10.1038/nmat3417.

[30] L. Viti *et al.*, "Black Phosphorus Terahertz Photodetectors," *Advanced Materials*, vol. 27, no. 37, pp. 5567–5572, Oct. 2015, doi: 10.1002/ADMA.201502052.

[31] Y. Xie *et al.*, "Defect Engineering of MoS2 for Room-Temperature Terahertz Photodetection," *ACS Applied Materials and Interfaces*, vol. 12, no. 6, pp. 7351–7357,

Feb. 2020, doi: 10.1021/ACSAMI.9B21671/SUPPL_FILE/AM9B21671_SI_001.PDF.

[32] W. J. Stillman and M. S. Shur, “Closing the gap: Plasma wave electronic terahertz detectors,” *Journal of Nanoelectronics and Optoelectronics*, vol. 2, no. 3, pp. 209–221, Dec. 2007, doi: 10.1166/JNO.2007.301.

[33] S. Regensburger *et al.*, “Broadband THz detection from 0.1 to 22 THz with large area field-effect transistors,” *Optics Express, Vol. 23, Issue 16, pp. 20732-20742*, vol. 23, no. 16, pp. 20732–20742, Aug. 2015, doi: 10.1364/OE.23.020732.

[34] Y. Kurita *et al.*, “Ultrahigh sensitive sub-terahertz detection by InP-based asymmetric dual-grating-gate high-electron-mobility transistors and their broadband characteristics,” *Applied Physics Letters*, vol. 104, no. 25, p. 251114, Jun. 2014, doi: 10.1063/1.4885499.

[35] W. Knap *et al.*, “Plasma wave detection of sub-terahertz and terahertz radiation by silicon field-effect transistors,” *Applied Physics Letters*, vol. 85, no. 4, p. 675, Jul. 2004, doi: 10.1063/1.1775034.

[36] W. Stillman *et al.*, “SILICON FINFETS AS DETECTORS OF TERAHERTZ AND SUB-TERAHERTZ RADIATION,” *http://dx.doi.org/10.1142/S0129156411006374*, vol. 20, no. 1, pp. 27–42, Apr. 2012, doi: 10.1142/S0129156411006374.

[37] N. Pala, F. Teppe, D. Veksler, Y. Deng, M. S. Shur, and R. Gaska, “Nonresonant detection of terahertz radiation by silicon-on-insulator MOSFETs,” *Electronics Letters*, vol. 41, no. 7, pp. 447–449, Mar. 2005, doi: 10.1049/EL:20058182.

[38] T. Otsuji, M. Hanabe, and O. Ogawara, “Terahertz plasma wave resonance of two-dimensional electrons in InGaP⁄InGaAs⁄GaAs high-electron-mobility transistors,” *Applied Physics Letters*, vol. 85, no. 11, p. 2119, Sep. 2004, doi: 10.1063/1.1792377.

[39] A. el Fatimy *et al.*, “Terahertz detection by GaN/AlGaN transistors,” *Electronics Letters*, vol. 42, no. 23, pp. 1342–1344, 2006, doi: 10.1049/EL:20062452.

[40] D. A. Bandurin *et al.*, “Resonant terahertz detection using graphene plasmons,” *Nature Communications 2018 9:1*, vol. 9, no. 1, pp. 1–8, Dec. 2018, doi: 10.1038/s41467-018-07848-w.

[41] M. Shur, S. Rudin, G. Rupper, and T. Ivanov, “p-Diamond as candidate for plasmonic terahertz and far infrared applications,” *Applied Physics Letters*, vol. 113, no. 25, p. 253502, Dec. 2018, doi: 10.1063/1.5053091.

[42] V. Y. Kachorovskii and M. S. Shur, “Field effect transistor as ultrafast detector of modulated terahertz radiation,” *Solid-State Electronics*, vol. 52, no. 2, pp. 182–185, Feb. 2008, doi: 10.1016/J.SSE.2007.08.002.

[43] M. I. Dyakonov and M. S. Shur, “Plasma wave electronics: Novel terahertz devices using two dimensional electron fluid,” *IEEE Transactions on Electron Devices*, vol. 43, no. 10, pp. 1640–1645, 1996, doi: 10.1109/16.536809.

[44] M. I. Dyakonov, “Terahertz electronic and optoelectronic components and systems Generation and detection of Terahertz radiation by field effect transistors Génération et détection de rayonnement térahertz avec des transistors à effet de champ,” *C. R. Physique*, vol. 11, pp. 413–420, 2010, doi: 10.1016/j.crhy.2010.05.003.

[45] N. Akter, N. Pala, W. Knap, and M. Shur, “THz Plasma Field Effect Transistor Detectors,” *Fundamentals of Terahertz Devices and Applications*, pp. 285–322, Jul. 2021, doi: 10.1002/9781119460749.CH8.

[46] M. Shur, S. Rudin, G. Rupper, F. Dagefu, and M. Brodsky, “TeraFETs for Terahertz Communications,” *Photonics Newsletter, vol. 33, no. 3, ,* pp. 4–7, 2019.

[47] J. A. Shaw, “Radiometry and the Friis transmission equation,” *American Journal of Physics*, vol. 81, no. 1, p. 33, Dec. 2012, doi: 10.1119/1.4755780.

[48] A. S. Hajo, O. Yilmazoglu, A. Dadgar, F. Kuppers, and T. Kusserow, “Reliable GaN-Based THz gunn diodes with side-contact and field-plate technologies,” *IEEE Access*, vol. 8, pp. 84116–84122, 2020, doi: 10.1109/ACCESS.2020.2991309.

[49] M. Asada and S. Suzuki, “Terahertz Emitter Using Resonant-Tunneling Diode and Applications,” *Sensors 2021, Vol. 21, Page 1384*, vol. 21, no. 4, p. 1384, Feb. 2021, doi: 10.3390/S21041384.

[50] M. Asada and S. Suzuki, “Room-Temperature Oscillation of Resonant Tunneling Diodes close to 2 THz and Their Functions for Various Applications,” *Journal of Infrared, Millimeter, and Terahertz Waves*, vol. 37, no. 12, pp. 1185–1198, Dec. 2016, doi: 10.1007/S10762-016-0321-6/FIGURES/13.

[51] D. Gamzina *et al.*, “Backward wave oscillator for high power generation at THz frequencies,” *https://doi.org/10.1117/12.2273256*, vol. 10383, p. 1038303, Aug. 2017, doi: 10.1117/12.2273256.

[52] K. Fujita, S. Hayashi, A. Ito, M. Hitaka, and T. Dougakiuchi, “Sub-terahertz and terahertz generation in long-wavelength quantum cascade lasers,” *Nanophotonics*,

vol. 8, no. 12, pp. 2235–2241, Dec. 2019, doi: 10.1515/NANOPH-2019-0238/MACHINEREADABLECITATION/RIS.

[53] Q. Lu, D. Wu, S. Sengupta, S. Slivken, and M. Razeghi, "Room temperature continuous wave, monolithic tunable THz sources based on highly efficient mid-infrared quantum cascade lasers," *Scientific Reports 2016 6:1*, vol. 6, no. 1, pp. 1–7, Mar. 2016, doi: 10.1038/srep23595.

[54] K. Murate and K. Kawase, "Perspective: Terahertz wave parametric generator and its applications," *Journal of Applied Physics*, vol. 124, no. 16, p. 160901, Oct. 2018, doi: 10.1063/1.5050079.

[55] J. Hamazaki *et al.*, "Conversion efficiency improvement of terahertz wave generation laterally emitted by a ridge-type periodically poled lithium niobate," *Optics Express, Vol. 30, Issue 7, pp. 11472-11478*, vol. 30, no. 7, pp. 11472–11478, Mar. 2022, doi: 10.1364/OE.450876.

[56] R. Huang *et al.*, "Design of a Pre-Bunched THz Free Electron Laser," *Particles 2018, Vol. 1, Pages 267-278*, vol. 1, no. 1, pp. 267–278, Nov. 2018, doi: 10.3390/PARTICLES1010021.

[57] J. F. O'Hara, S. Ekin, W. Choi, and I. Song, "A Perspective on Terahertz Next-Generation Wireless Communications," *Technologies 2019, Vol. 7, Page 43*, vol. 7, no. 2, p. 43, Jun. 2019, doi: 10.3390/TECHNOLOGIES7020043.

[58] J. M. Chamberlain and R. E. Miles, "New Directions in Terahertz Technology," p. 444, 1997.

[59] A. Yazgan, L. Jofre, and J. Romeu, "Comparative Efficiency and Power Assessment of Optical Photoconductive Material-Based Terahertz Sources for Wireless Communication Systems," *https://doi.org/10.1142/S0218126619500051*, vol. 28, no. 1, Oct. 2018, doi: 10.1142/S0218126619500051.

[60] H. Eisele, A. Rydberg, and G. I. Haddad, "Recent advances in the performance of InP gunn devices and GaAs TUNNETT diodes for the 100-300-GHz frequency range and above," *IEEE Transactions on Microwave Theory and Techniques*, vol. 48, pp. 626–631, 2000, doi: 10.1109/22.841952.

[61] M. Dyakonov and M. Shur, "Shallow water analogy for a ballistic field effect transistor: New mechanism of plasma wave generation by dc current," *Physical Review Letters*, vol. 71, no. 15, p. 2465, Oct. 1993, doi: 10.1103/PhysRevLett.71.2465.

[62] M. Dyakonov and M. Shur, “Detection, mixing, and frequency multiplication of terahertz radiation by two-dimensional electronic fluid,” *IEEE Transactions on Electron Devices*, vol. 43, no. 3, pp. 380–387, 1996, doi: 10.1109/16.485650.

[63] S. D. Gedney, “Introduction to the Finite-Difference Time-Domain (FDTD) Method for Electromagnetics,” *Synthesis Lectures on Computational Electromagnetics*, vol. 27, pp. 1–250, Jan. 2011, doi: 10.2200/S00316ED1V01Y201012CEM027.

[64] “Nanophotonic FDTD Simulation Software - Lumerical FDTD.” https://www.lumerical.com/products/fdtd/ (accessed May 16, 2022).

[65] K. S. Yee, J. S. Chen, and A. H. Chang, “Conformal finite difference time domain (FDTD) with overlappinggrids,” *IEEE Antennas and Propagation Society, AP-S International Symposium (Digest)*, vol. 1992-June, pp. 1949–1952, 1992, doi: 10.1109/APS.1992.221489.

[66] F. Zheng, Z. Chen, and J. Zhang, “A Finite-Difference Time-Domain Method Without the Courant Stability Conditions,” *IEEE Microwave and Guided Wave Letters*, vol. 9, no. 11, pp. 441–443, 1999, doi: 10.1109/75.808026.

[67] “COMSOL - Software for Multiphysics Simulation.” https://www.comsol.com/ (accessed May 16, 2022).

[68] P. Tassin, T. Koschny, and C. M. Soukoulis, “Graphene for terahertz applications,” *Science*, vol. 341, no. 6146. American Association for the Advancement of Science, pp. 620–621, Aug. 09, 2013. doi: 10.1126/science.1242253.

[69] V. Ryzhii, T. Otsuji, and M. Shur, “Graphene based plasma-wave devices for terahertz applications,” *Applied Physics Letters*, vol. 116, no. 14, p. 140501, Apr. 2020, doi: 10.1063/1.5140712.

[70] K. S. Novoselov *et al.*, “Electric field in atomically thin carbon films,” *Science (1979)*, vol. 306, no. 5696, pp. 666–669, Oct. 2004, doi: 10.1126/SCIENCE.1102896/SUPPL_FILE/NOVOSELOV.SOM.PDF.

[71] F. Bonaccorso, Z. Sun, T. Hasan, and A. C. Ferrari, “Graphene photonics and optoelectronics,” *Nature Photonics 2010 4:9*, vol. 4, no. 9, pp. 611–622, Aug. 2010, doi: 10.1038/nphoton.2010.186.

[72] K. S. Novoselov, V. I. Fal’Ko, L. Colombo, P. R. Gellert, M. G. Schwab, and K. Kim, “A roadmap for graphene,” *Nature 2012 490:7419*, vol. 490, no. 7419, pp. 192–200, Oct. 2012, doi: 10.1038/nature11458.

[73] A. N. Grigorenko, M. Polini, and K. S. Novoselov, “Graphene plasmonics,” *Nature Photonics 2012 6:11*, vol. 6, no. 11, pp. 749–758, Nov. 2012, doi: 10.1038/nphoton.2012.262.

[74] Y. M. Lin *et al.*, “100-GHz transistors from wafer-scale epitaxial graphene,” *Science (1979)*, vol. 327, no. 5966, p. 662, Feb. 2010, doi: 10.1126/SCIENCE.1184289/SUPPL_FILE/LIN.SOM.PDF.

[75] T. Li *et al.*, “Femtosecond population inversion and stimulated emission of dense dirac fermions in graphene,” *Physical Review Letters*, vol. 108, no. 16, p. 167401, Apr. 2012, doi: 10.1103/PHYSREVLETT.108.167401/FIGURES/4/MEDIUM.

[76] S. Roy *et al.*, “Structure, Properties and Applications of Two-Dimensional Hexagonal Boron Nitride,” *Advanced Materials*, vol. 33, no. 44, p. 2101589, Nov. 2021, doi: 10.1002/ADMA.202101589.

[77] C. R. Dean *et al.*, “Boron nitride substrates for high-quality graphene electronics,” *Nature Nanotechnology 2010 5:10*, vol. 5, no. 10, pp. 722–726, Aug. 2010, doi: 10.1038/nnano.2010.172.

[78] M. Yankowitz *et al.*, “Emergence of superlattice Dirac points in graphene on hexagonal boron nitride,” *Nature Physics 2012 8:5*, vol. 8, no. 5, pp. 382–386, Mar. 2012, doi: 10.1038/nphys2272.

[79] C. R. Dean *et al.*, “Hofstadter’s butterfly and the fractal quantum Hall effect in moiré superlattices,” *Nature 2013 497:7451*, vol. 497, no. 7451, pp. 598–602, May 2013, doi: 10.1038/nature12186.

[80] A. K. Geim and I. v. Grigorieva, “Van der Waals heterostructures,” *Nature 2013 499:7459*, vol. 499, no. 7459, pp. 419–425, Jul. 2013, doi: 10.1038/nature12385.

[81] Y. Cao *et al.*, “Unconventional superconductivity in magic-angle graphene superlattices,” *Nature 2018 556:7699*, vol. 556, no. 7699, pp. 43–50, Mar. 2018, doi: 10.1038/nature26160.

[82] K. Komatsu *et al.*, “Observation of the quantum valley Hall state in ballistic graphene superlattices,” *Science Advances*, vol. 4, no. 5, May 2018, doi: 10.1126/SCIADV.AAQ0194/SUPPL_FILE/AAQ0194_SM.PDF.

[83] Y. Sasama, K. Komatsu, and S. Moriyama, “High-mobility diamond field effect transistor with a monocrystalline h-BN gate dielectric,” vol. 6, p. 111105, 2018, doi: 10.1063/1.5055812.

[84] A. Ranjan *et al.*, "Dielectric Breakdown in Single-Crystal Hexagonal Boron Nitride," *ACS Applied Electronic Materials*, vol. 3, no. 8, pp. 3547–3554, Aug. 2021, doi: 10.1021/ACSAELM.1C00469/SUPPL_FILE/EL1C00469_SI_001.PDF.

[85] Y. D. Huang *et al.*, "Plasmonic terahertz modulator based on a grating-coupled two-dimensional electron system," *Applied Physics Letters*, vol. 109, no. 20, p. 201110, Nov. 2016, doi: 10.1063/1.4967998.

[86] O. v. Minin, I. v. Minin, Y. M. Meziani, and S. Hisatake, "Improvement of a point-contact detector performance using the terajet effect initiated by photonics," *https://doi.org/10.1117/1.OE.60.8.082005*, vol. 60, no. 8, p. 082005, Oct. 2020, doi: 10.1117/1.OE.60.8.082005.

[87] E. Öjefors, A. Lisauskas, D. Glaab, H. G. Roskos, and U. R. Pfeiffer, "Terahertz imaging detectors in CMOS technology," *Journal of Infrared, Millimeter, and Terahertz Waves*, vol. 30, no. 12, pp. 1269–1280, Aug. 2009, doi: 10.1007/S10762-009-9569-4/FIGURES/8.

[88] T. Tanigawa, T. Onishi, S. Takigawa, and T. Otsuje, "Enhanced responsivity in a novel AlGaN / GaN plasmon-resonant terahertz detector using gate-dipole antenna with parasitic elements," *Device Research Conference - Conference Digest, DRC*, pp. 167–168, 2010, doi: 10.1109/DRC.2010.5551895.

[89] J. D. Sun, Y. F. Sun, D. M. Wu, Y. Cai, H. Qin, and B. S. Zhang, "High-responsivity, low-noise, room-temperature, self-mixing terahertz detector realized using floating antennas on a GaN-based field-effect transistor," *Applied Physics Letters*, vol. 100, no. 1, p. 013506, Jan. 2012, doi: 10.1063/1.3673617.

[90] M. Yu *et al.*, "Bowtie loaded meander antenna for a high-temperature superconducting terahertz detector and its characterization by the Josephson effect," *Optics Express, Vol. 28, Issue 10, pp. 14271-14279*, vol. 28, no. 10, pp. 14271–14279, May 2020, doi: 10.1364/OE.390997.

[91] K. Ikamas, D. B. But, and A. Lisauskas, "Homodyne Spectroscopy with Broadband Terahertz Power Detector Based on 90-nm Silicon CMOS Transistor," *Applied Sciences 2021, Vol. 11, Page 412*, vol. 11, no. 1, p. 412, Jan. 2021, doi: 10.3390/APP11010412.

[92] B. Zhang, W. Yan, Z. Li, L. Bai, and F. Yang, "Analysis of substrate effect in field effect transistor terahertz detectors," *IEEE Journal on Selected Topics in Quantum Electronics*, vol. 23, no. 4, Jul. 2017, doi: 10.1109/JSTQE.2016.2633865.

[93] Z. Y. Liu, L. Y. Liu, J. Yang, and N. J. Wu, "A CMOS Fully Integrated 860-GHz Terahertz Sensor," *IEEE Transactions on Terahertz Science and Technology*, vol. 7, no. 4, pp. 455–465, Jul. 2017, doi: 10.1109/TTHZ.2017.2692040.

[94] P. Kopyt, B. Salski, P. Zagrajek, D. Obrebski, and J. Marczewski, “Modeling of Silicon-Based Substrates of Patch Antennas Operating in the Sub-THz Range,” *IEEE Transactions on Terahertz Science and Technology*, vol. 7, no. 4, pp. 424–432, Jul. 2017, doi: 10.1109/TTHZ.2017.2706026.

[95] M. Labidi and F. Choubani, “Performances enhancement of metamaterial loop antenna for terahertz applications,” *Opt Mater (Amst)*, vol. 82, pp. 116–122, Aug. 2018, doi: 10.1016/J.OPTMAT.2018.05.050.

[96] J. Mou, Q. Xue, D. Guo, and X. Lv, “A THz Detector Chip with Printed Circular Cavity as Package and Enhancement of Antenna Gain,” *IEEE Transactions on Antennas and Propagation*, vol. 64, no. 4, pp. 1242–1249, Apr. 2016, doi: 10.1109/TAP.2016.2526068.

[97] S. Lepeshov, A. Gorodetsky, A. Krasnok, E. Rafailov, and P. Belov, “Enhancement of terahertz photoconductive antenna operation by optical nanoantennas,” *Laser & Photonics Reviews*, vol. 11, no. 1, p. 1600199, Jan. 2017, doi: 10.1002/LPOR.201600199.

[98] T. Gric, A. Gorodetsky, A. Trofimov, and E. Rafailov, “Tunable Plasmonic Properties and Absorption Enhancement in Terahertz Photoconductive Antenna Based on Optimized Plasmonic Nanostructures,” *Journal of Infrared, Millimeter, and Terahertz Waves*, vol. 39, no. 10, pp. 1028–1038, Oct. 2018, doi: 10.1007/S10762-018-0516-0/FIGURES/8.

[99] C. Liu *et al.*, “Graphene-based broadband terahertz detector integrated with a square-spiral antenna,” *Optics Letters, Vol. 43, Issue 8, pp. 1647-1650*, vol. 43, no. 8, pp. 1647–1650, Apr. 2018, doi: 10.1364/OL.43.001647.

[100] J. Gou, Q. Niu, K. Liang, J. Wang, and Y. Jiang, “Frequency Modulation and Absorption Improvement of THz Micro-bolometer with Micro-bridge Structure by Spiral-Type Antennas,” *Nanoscale Research Letters*, vol. 13, no. 1, pp. 1–9, Mar. 2018, doi: 10.1186/S11671-018-2484-7/FIGURES/9.

[101] Z. Huang, Z. Li, H. Dong, F. Yang, W. Yan, and X. Wang, “Novel Broadband Slot-Spiral Antenna for Terahertz Applications,” *Photonics 2021, Vol. 8, Page 123*, vol. 8, no. 4, p. 123, Apr. 2021, doi: 10.3390/PHOTONICS8040123.

[102] Mustafa Karabiyik; and Nezih Pala, “Graphene devices for terahertz detection and emission,” Patent # 16288748, 2019

[103] H. N. Abbasi, Y. F. Wang, W. Wang, J. Hussain, and H. X. Wang, “Diamond field effect transistors using bilayer dielectrics Yb2TiO5/Al2O3 on hydrogen-terminated diamond,” *Diamond and Related Materials*, vol. 106, p. 107866, Jun. 2020, doi: 10.1016/J.DIAMOND.2020.107866.

[104] M. Bhatnagar and B. J. Baliga, “Comparison of 6H-SiC, 3C-SiC, and Si for Power Devices,” *IEEE Transactions on Electron Devices*, vol. 40, no. 3, pp. 645–655, 1993, doi: 10.1109/16.199372.

[105] W. Saito *et al.*, “High Breakdown Voltage AlGaN-GaN Power-HEMT Design and High Current Density Switching Behavior,” *IEEE Transactions on Electron Devices*, vol. 50, no. 12, pp. 2528–2531, Dec. 2003, doi: 10.1109/TED.2003.819248.

[106] H. Umezawa, M. Nagase, Y. Kato, and S. I. Shikata, “High temperature application of diamond power device,” *Diamond and Related Materials*, vol. 24, pp. 201–205, Apr. 2012, doi: 10.1016/J.DIAMOND.2012.01.011.

[107] T. T. Pham, J. Pernot, G. Perez, D. Eon, E. Gheeraert, and N. Rouger, “Deep-Depletion Mode Boron-Doped Monocrystalline Diamond Metal Oxide Semiconductor Field Effect Transistor,” *IEEE Electron Device Letters*, vol. 38, no. 11, pp. 1571–1574, Nov. 2017, doi: 10.1109/LED.2017.2755718.

[108] T. Matsumoto *et al.*, “Inversion channel diamond metal-oxide-semiconductor field-effect transistor with normally off characteristics,” *Scientific Reports 2016 6:1*, vol. 6, no. 1, pp. 1–6, Aug. 2016, doi: 10.1038/srep31585.

[109] T. Suwa *et al.*, “Normally-off diamond junction field-effect transistors with submicrometer channel,” *IEEE Electron Device Letters*, vol. 37, no. 2, pp. 209–211, Feb. 2016, doi: 10.1109/LED.2015.2513074.

[110] W. Wang *et al.*, “Diamond based field-effect transistors with SiNx and ZrO2 double dielectric layers,” *Diamond and Related Materials*, vol. 69, pp. 237–240, Oct. 2016, doi: 10.1016/J.DIAMOND.2016.04.014.

[111] M. Kasu, “Diamond field-effect transistors for RF power electronics: Novel NO2 hole doping and low-temperature deposited Al2O3 passivation,” *Japanese Journal of Applied Physics*, vol. 56, no. 1, p. 01AA01, Jan. 2017, doi: 10.7567/JJAP.56.01AA01/XML.

[112] J. Liu, H. Ohsato, M. Liao, M. Imura, E. Watanabe, and Y. Koide, “Logic circuits with hydrogenated diamond field-effect transistors,” *IEEE Electron Device Letters*, vol. 38, no. 7, pp. 922–925, Jul. 2017, doi: 10.1109/LED.2017.2702744.

[113] W. Wang *et al.*, “An Enhancement-Mode Hydrogen-Terminated Diamond Field-Effect Transistor with Lanthanum Hexaboride Gate Material,” *IEEE Electron Device Letters*, vol. 41, no. 4, pp. 585–588, Apr. 2020, doi: 10.1109/LED.2020.2972330.

[114] D. Kueck, P. Leber, A. Schmidt, G. Speranza, and E. Kohn, “AlN as passivation for surface channel FETs on H-terminated diamond,” *Diamond and Related Materials*, vol. 19, no. 7–9, pp. 932–935, Jul. 2010, doi: 10.1016/J.DIAMOND.2010.02.026.

[115] M. Shur, S. Rudin, G. Rupper, and T. Ivanov, “p-Diamond as candidate for plasmonic terahertz and far infrared applications,” *Applied Physics Letters*, vol. 113, no. 25, p. 253502, Dec. 2018, doi: 10.1063/1.5053091.

[116] Y. Zhang and M. S. Shur, “P-diamond Plasmonic TeraFET Detector,” *International Conference on Infrared, Millimeter, and Terahertz Waves, IRMMW-THz*, vol. 2020-November, pp. 779–780, Nov. 2020, doi: 10.1109/IRMMW-THZ46771.2020.9371002.

[117] M. S. Shur, “Si, SiGe, InP, III-N, and p-diamond FETs and HBTs for sub-terahertz and terahertz applications,” *https://doi.org/10.1117/12.2551204*, vol. 11279, p. 1127903, Mar. 2020, doi: 10.1117/12.2551204.

[118] M. W. Geis *et al.*, “Progress Toward Diamond Power Field-Effect Transistors,” *physica status solidi (a)*, vol. 215, no. 22, p. 1800681, Nov. 2018, doi: 10.1002/PSSA.201800681.

[119] M. W. Geis *et al.*, “Progress Toward Diamond Power Field-Effect Transistors,” *physica status solidi (a)*, vol. 215, no. 22, p. 1800681, Nov. 2018, doi: 10.1002/PSSA.201800681.

[120] A. Aleksov *et al.*, “Diamond field effect transistors—concepts and challenges,” *Diamond and Related Materials*, vol. 12, no. 3–7, pp. 391–398, Mar. 2003, doi: 10.1016/S0925-9635(02)00401-6.

[121] H. Taniuchi, H. Umezawa, T. Arima, M. Tachiki, and H. Kawarada, “High-frequency performance of diamond field-effect transistor,” *IEEE Electron Device Letters*, vol. 22, no. 8, pp. 390–392, Aug. 2001, doi: 10.1109/55.936353.

[122] Y. Yamamoto, T. Imai, K. Tanabe, T. Tsuno, Y. Kumazawa, and N. Fujimori, “The measurement of thermal properties of diamond,” *Diamond and Related Materials*, vol. 6, no. 8, pp. 1057–1061, May 1997, doi: 10.1016/S0925-9635(96)00772-8.

[123] J. Isberg *et al.*, “High carrier mobility in single-crystal plasma-deposited diamond,” *Science (1979)*, vol. 297, no. 5587, pp. 1670–1672, Sep. 2002, doi: 10.1126/SCIENCE.1074374/ASSET/97C83FE7-F776-4EF3-860F-13B22173909C/ASSETS/GRAPHIC/SE3320811004.JPEG.

[124] M. Liao, “Progress in semiconductor diamond photodetectors and MEMS sensors,” *https://doi.org/10.1080/26941112.2021.1877019*, vol. 1, no. 1, pp. 29–46, Jan. 2021, doi: 10.1080/26941112.2021.1877019.

[125] S. Shikata, “Single crystal diamond wafers for high power electronics,” *Diamond and Related Materials*, vol. 65, pp. 168–175, May 2016, doi: 10.1016/J.DIAMOND.2016.03.013.

[126] L. Sang, “Diamond as the heat spreader for the thermal dissipation of GaN-based electronic devices,” *https://doi.org/10.1080/26941112.2021.1980356*, vol. 1, no. 1, pp. 174–188, Jan. 2021, doi: 10.1080/26941112.2021.1980356.

[127] S. Koizumi, K. Watanabe, M. Hasegawa, and H. Kanda, “Ultraviolet emission from a diamond pn junction,” *Science (1979)*, vol. 292, no. 5523, pp. 1899–1901, Jun. 2001, doi: 10.1126/SCIENCE.1060258/ASSET/79E03E59-E661-462E-B8C1-5D0D93B52B94/ASSETS/GRAPHIC/SE2119484003.JPEG.

[128] J. Achard *et al.*, “Thick boron doped diamond single crystals for high power electronics,” *Diamond and Related Materials*, vol. 20, no. 2, pp. 145–152, Feb. 2011, doi: 10.1016/J.DIAMOND.2010.11.014.

[129] T. Shimaoka, M. Liao, and S. Koizumi, “n-Type Diamond Metal-Semiconductor Field-Effect Transistor With High Operation Temperature of 300°C,” *IEEE Electron Device Letters*, vol. 43, no. 4, pp. 588–591, Apr. 2022, doi: 10.1109/LED.2022.3156149.

[130] E. Gheeraert, S. Koizumi, T. Teraji, and H. Kanda, “Electronic transitions of electrons bound to phosphorus donors in diamond,” *Solid State Communications*, vol. 113, no. 10, pp. 577–580, Feb. 2000, doi: 10.1016/S0038-1098(99)00546-3.

[131] P. Gluche, A. Aleksov, A. Vescan, W. Ebert, and E. Kohn, “Diamond surface-channel FET structure with 200 V breakdown voltage,” *IEEE Electron Device Letters*, vol. 18, no. 11, pp. 547–549, Nov. 1997, doi: 10.1109/55.641441.

[132] H. Umezawa, H. Taniuchi, T. Arima, M. Tachiki, and H. Kawarada, “Potential applications of surface channel diamond field-effect transistors,” *Diamond and Related Materials*, vol. 10, no. 9–10, pp. 1743–1748, Sep. 2001, doi: 10.1016/S0925-9635(01)00406-X.

[133] D. A. J. Moran, O. J. L. Fox, H. McLelland, S. Russell, and P. W. May, “Scaling of hydrogen-terminated diamond FETs to sub-100-nm gate dimensions,” *IEEE Electron Device Letters*, vol. 32, no. 5, pp. 599–601, May 2011, doi: 10.1109/LED.2011.2114871.

[134] H. Kawarada, M. Aoki, and M. Ito, “Enhancement mode metal-semiconductor field effect transistors using homoepitaxial diamonds,” *Applied Physics Letters*, vol. 65, no. 12, p. 1563, Aug. 1998, doi: 10.1063/1.112915.

[135] H. Umezawa, T. Matsumoto, and S. I. Shikata, “Diamond metal-semiconductor field-effect transistor with breakdown voltage over 1.5 kV,” *IEEE Electron Device Letters*, vol. 35, no. 11, pp. 1112–1114, Nov. 2014, doi: 10.1109/LED.2014.2356191.

[136] H. Kawashima, S. Ohmagari, H. Umezawa, and D. Takeuchi, “Improved drain current of diamond metal–semiconductor field-effect transistor by selectively grown p+ contact layer,” *Japanese Journal of Applied Physics*, vol. 58, no. SB, p. SBBD17, Apr. 2019, doi: 10.7567/1347-4065/AB073D.

[137] S. Rudin, G. Rupper, A. Gutin, and M. Shur, “Theory and measurement of plasmonic terahertz detector response to large signals,” *Journal of Applied Physics*, vol. 115, no. 6, p. 064503, Feb. 2014, doi: 10.1063/1.4862808.

[138] Y. H. Byun, K. Lee, and M. Shur, “Unified Charge Control Model and Subthreshold Current in Heterostructure Field-Effect Transistors,” *IEEE Electron Device Letters*, vol. 11, no. 1, pp. 50–53, 1990, doi: 10.1109/55.46928.

[139] S. Rudin, G. Rupper, and M. Shur, “Ultimate response time of high electron mobility transistors,” *Journal of Applied Physics*, vol. 117, no. 17, p. 174502, May 2015, doi: 10.1063/1.4919706.

[140] G. Rupper, S. Rudin, and F. J. Crowne, “Effects of oblique wave propagation on the nonlinear plasma resonance in the two-dimensional channel of the Dyakonov–Shur detector,” *Solid-State Electronics*, vol. 78, pp. 102–108, Dec. 2012, doi: 10.1016/J.SSE.2012.05.052.

[141] S. Rudin, G. Rupper, T. G. Ivanov, J. Weil, and M. S. Shur, “p-Diamond as a plasmonic material for terahertz applications,” p. 26, Apr. 2021, doi: 10.1117/12.2587129.

[142] W. Knap *et al.*, “Nonresonant detection of terahertz radiation in field effect transistors,” *Journal of Applied Physics*, vol. 91, no. 11, p. 9346, May 2002, doi: 10.1063/1.1468257.

[143] S. Rudin, “Temperature dependence of the nonlinear plasma resonance in gated two-dimensional semiconductor conduction channels,” *Applied Physics Letters*, vol. 96, no. 25, p. 252101, Jun. 2010, doi: 10.1063/1.3455993.

[144] Y. Zhang and M. S. Shur, “P-diamond Plasmonic TeraFET Detector,” *International Conference on Infrared, Millimeter, and Terahertz Waves, IRMMW-*

THz, vol. 2020-November, pp. 779–780, Nov. 2020, doi: 10.1109/IRMMW-THZ46771.2020.9371002.

[145] I. Akimoto, Y. Handa, K. Fukai, and N. Naka, "High carrier mobility in ultrapure diamond measured by time-resolved cyclotron resonance," *Applied Physics Letters*, vol. 105, no. 3, p. 032102, Jul. 2014, doi: 10.1063/1.4891039.

[146] M. D. Hill, J. Masters, P. Ranganathan, P. Turner, and J. L. Hennessy, "On the Spectre and Meltdown Processor Security Vulnerabilities," *IEEE Micro*, vol. 39, no. 2, pp. 9–19, Mar. 2019, doi: 10.1109/MM.2019.2897677.

[147] N. Abu-Ghazaleh, D. Ponomarev, and D. Evtyushkin, "How the spectre and meltdown hacks really worked," *IEEE Spectrum*, vol. 56, no. 3, pp. 42–49, Mar. 2019, doi: 10.1109/MSPEC.2019.8651934.

[148] U. Guin, D. Dimase, and M. Tehranipoor, "Counterfeit integrated circuits: Detection, avoidance, and the challenges ahead," *Journal of Electronic Testing: Theory and Applications (JETTA)*, vol. 30, no. 1, pp. 9–23, Feb. 2014, doi: 10.1007/S10836-013-5430-8/TABLES/2.

[149] U. Guin, K. Huang, D. Dimase, J. M. Carulli, M. Tehranipoor, and Y. Makris, "Counterfeit integrated circuits: A rising threat in the global semiconductor supply chain," *Proceedings of the IEEE*, vol. 102, no. 8, pp. 1207–1228, 2014, doi: 10.1109/JPROC.2014.2332291.

[150] U. Guin, D. Forte, and M. Tehranipoor, "Anti-counterfeit techniques: From design to resign," *Proceedings - International Workshop on Microprocessor Test and Verification*, pp. 89–94, Oct. 2014, doi: 10.1109/MTV.2013.28.

[151] S. E. Quadir *et al.*, "A Survey on Chip to System Reverse Engineering," *ACM Journal on Emerging Technologies in Computing Systems (JETC)*, vol. 13, no. 1, Apr. 2016, doi: 10.1145/2755563.

[152] N. Asadizanjani, S. Shahbazmohamadi, M. Tehranipoor, and D. Forte, "Non-destructive PCB reverse engineering using X-ray micro computed tomography," *Conference Proceedings from the International Symposium for Testing and Failure Analysis*, vol. 2015-January, pp. 164–172, Nov. 2015, doi: 10.31399/ASM.CP.ISTFA2015P0164/10172/NON-DESTRUCTIVE-PCB-REVERSE-ENGINEERING-USING-X.

[153] Richard J. Ross, Ed., *Microelectronics Failure Analysis: Desk Reference Sixth Edition*. ASM International, 2011. Accessed: Aug. 03, 2020. [Online]. Available: www.asminternational.org

[154] P. Aryan, S. Sampath, and H. Sohn, “An Overview of Non-Destructive Testing Methods for Integrated Circuit Packaging Inspection,” *Sensors*, vol. 18, no. 7, p. 1981, Jun. 2018, doi: 10.3390/s18071981.

[155] O. Breitenstein, J. P. Rakotoniaina, F. Altmann, J. Schulz, and G. Linse, “Fault Localization and Functional Testing of ICs by Lock-in Thermography,” in *ASM International; INTERNATIONSYMPOSIUM FOR TESTING AND FAILURE ANALYSIS*, 1998, pp. 29–38.

[156] T. C. Chai, B. S. Wong, W. M. Bai, A. Trigg, and Y. K. Lam, “A novel defect detection technique using active transient thermography for high density package and interconnections,” in *Proceedings - Electronic Components and Technology Conference*, 2003, pp. 920–925. doi: 10.1109/ectc.2003.1216400.

[157] S. Liu and I. C. Ume, “Vibration analysis based modeling and defect recognition for flip-chip solder-joint inspection,” *Journal of Electronic Packaging, Transactions of the ASME*, vol. 124, no. 3, pp. 221–226, Sep. 2002, doi: 10.1115/1.1464878.

[158] L. Su, T. Shi, Z. Liu, H. Zhou, L. Du, and G. Liao, “Nondestructive diagnosis of flip chips based on vibration analysis using PCA-RBF,” *Mechanical Systems and Signal Processing*, vol. 85, pp. 849–856, Feb. 2017, doi: 10.1016/j.ymssp.2016.09.030.

[159] T. D. Moore, D. Vanderstraeten, and P. M. Forssell, “Three-dimensional x-ray laminography as a tool for detection and characterization of BGA package defects,” *IEEE Transactions on Components and Packaging Technologies*, vol. 25, no. 2, pp. 224–229, Jun. 2002, doi: 10.1109/TCAPT.2002.1010010.

[160] Y. J. Roh, K. W. Ko, H. Cho, H. C. Kim, H. Joo, and S. K. Kim, “Inspection of ball grid array (BGA) solder joints using x-ray cross-sectional images,” in *Machine Vision Systems for Inspection and Metrology VIII*, Aug. 1999, vol. 3836, pp. 168–178. doi: 10.1117/12.360270.

[161] E. Martin, C. Larato, A. Clément, and M. Saint-Paul, “Detection of delaminations in sub-wavelength thick multi-layered packages from the local temporal coherence of ultrasonic signals,” *NDT & E International*, vol. 41, no. 4, pp. 280–291, Jun. 2008, doi: 10.1016/J.NDTEINT.2007.10.013.

[162] J. E. Semmens and L. W. Kessler, “Further investigation into the use of acoustic micro imaging for analyzing flip chip integrity and failure modes,” in *In Proceedings 1997 International Conference on Multichip Modules*, Nov. 1997, pp. 165–169. doi: 10.1109/icmcm.1997.581167.

[163] J. E. Semmens and L. W. Kessler, “Characterization of flip chip interconnect failure modes using high frequency acoustic micro imaging with correlative analysis,” in *Annual Proceedings - Reliability Physics (Symposium)*, 1997, pp. 141–148. doi: 10.1109/relphy.1997.584251.

[164] K. Ahi, S. Shahbazmohamadi, and N. Asadizanjani, “Quality control and authentication of packaged integrated circuits using enhanced-spatial-resolution terahertz time-domain spectroscopy and imaging,” *Optics and Lasers in Engineering*, vol. 104, pp. 274–284, May 2018, doi: 10.1016/J.OPTLASENG.2017.07.007.

[165] E. Keenan, R. G. Wright, R. Mulligan, and L. v. Kirkland, “Terahertz and laser imaging for printed circuit board failure detection,” *AUTOTESTCON (Proceedings)*, pp. 563–569, 2004, doi: 10.1109/AUTEST.2004.1436955.

[166] S. H. Park, J. W. Jang, and H. S. Kim, “Non-destructive evaluation of the hidden voids in integrated circuit packages using terahertz time-domain spectroscopy,” *Journal of Micromechanics and Microengineering*, vol. 25, no. 9, p. 095007, Aug. 2015, doi: 10.1088/0960-1317/25/9/095007.

[167] N. M. Burford and M. O. El-Shenawee, “Enhancement of terahertz imaging of packaged power electronic devices,” *IEEE Antennas and Propagation Society, AP-S International Symposium (Digest)*, vol. 2015-October, pp. 1300–1301, Oct. 2015, doi: 10.1109/APS.2015.7305039.

[168] G. M. Zhang, D. M. Harvey, and D. R. Braden, “Microelectronic package characterisation using scanning acoustic microscopy,” *NDT & E International*, vol. 40, no. 8, pp. 609–617, Dec. 2007, doi: 10.1016/J.NDTEINT.2007.05.002.

[169] Y. Lu, Q. Mao, and J. Liu, “A Deep Transfer Learning Model for Packaged Integrated Circuit Failure Detection by Terahertz Imaging,” *IEEE Access*, vol. 9, pp. 138608–138617, 2021, doi: 10.1109/ACCESS.2021.3118687.

[170] B. B. Hu and M. C. Nuss, “Imaging with terahertz waves,” *Optics Letters, Vol. 20, Issue 16, pp. 1716-1718*, vol. 20, no. 16, pp. 1716–1718, Aug. 1995, doi: 10.1364/OL.20.001716.

[171] Y. Cai, Z. Wang, R. Dias, and D. Goyal, “Electro Optical Terahertz Pulse Reflectometry - An innovative fault isolation tool,” *Proceedings - Electronic Components and Technology Conference*, pp. 1309–1315, 2010, doi: 10.1109/ECTC.2010.5490646.

[172] M. Nagel *et al.*, “Contact-free fault location and imaging with on-chip terahertz time-domain reflectometry,” *Optics Express, Vol. 19, Issue 13, pp. 12509-12514*, vol. 19, no. 13, pp. 12509–12514, Jun. 2011, doi: 10.1364/OE.19.012509.

[173] F. Blanchard, A. Doi, T. Tanaka, and K. Tanaka, “Real-Time, Subwavelength Terahertz Imaging,” *http://dx.doi.org/10.1146/annurev-matsci-071312-121656*, vol. 43, pp. 237–259, Jul. 2013, doi: 10.1146/ANNUREV-MATSCI-071312-121656.

[174] M. S. Shur and J. Suarez, “Nanoscale silicon mosfet response to THz radiation for testing VLSI,” in *27th North Atlantic Test Workshop, NATW 2018*, Jun. 2018, pp. 1–6. doi: 10.1109/NATW.2018.8388865.

[175] W. Stillman *et al.*, “Silicon finfets as detectors of terahertz and sub-terahertz radiation,” in *International Journal of High Speed Electronics and Systems*, Mar. 2011, vol. 20, no. 1, pp. 27–42. doi: 10.1142/S0129156411006374.

[176] W. Stillman *et al.*, “Nanometer scale complementary silicon MOSFETs as detectors of terahertz and sub-terahertz radiation,” in *Proceedings of IEEE Sensors*, 2007, pp. 934–937. doi: 10.1109/ICSENS.2007.4388556.

[177] W. Stillman, M. S. Shur, D. Veksler, S. Rumyantsev, and F. Guarin, “Device loading effects on nonresonant detection of terahertz radiation by silicon MOSFETs,” *Electronics Letters*, vol. 43, no. 7, pp. 422–423, 2007, doi: 10.1049/EL:20073475.

[178] M. Shur and J. Suarez, “Terahertz testing of very large scale integrated circuits,” *Semiconductor Technology for Ultra Large Scale Integrated Circuits and Thin Film Transistors VII*, May 2019, Accessed: Aug. 03, 2020. [Online]. Available: https://dc.engconfintl.org/ulsic_tft_vii/51

[179] M. Shur, S. Rudin, G. Rupper, M. Reed, and J. Suarez, “Sub-terahertz testing of millimeter wave Monolithic and very large scale integrated circuits,” *Solid-State Electronics*, vol. 155, pp. 44–48, May 2019, doi: 10.1016/j.sse.2019.03.007.

[180] N. Akter, M. R. Siddiquee, M. Shur, and N. Pala, “AI-Powered Terahertz VLSI Testing Technology for Ensuring Hardware Security and Reliability,” *IEEE Access*, vol. 9, pp. 64499–64509, 2021, doi: 10.1109/ACCESS.2021.3075429.

[181] N. Akter, M. Karabiyik, A. Wright, M. Shur, and N. Pala, “AI Powered THz Testing Technology for Ensuring Hardware Cybersecurity,” *2020 IEEE Research and Applications of Photonics in Defense Conference, RAPID 2020 - Proceedings*, Aug. 2020, doi: 10.1109/RAPID49481.2020.9195662.

[182] N. Akter, M. Karabiyik, M. Shur, J. Suarez, and N. Pala, “AI Powered THz VLSI Testing Technology,” *29th North Atlantic Test Workshop, NATW 2020*, Jun. 2020, doi: 10.1109/NATW49237.2020.9153077.

[183] G. Rupper, J. Suarez, S. Rudin, M. Reed, and M. Shur, “Terahertz Plasmonics for Testing Very Large-Scale Integrated Circuits under Bias,” United States, The Government of the United States, as represented by the Secretary of the Army (Washington, DC, US), 15/437713, Aug. 2018 [Online]. Available: https://www.freepatentsonline.com/y2018/0238961.html

[184] M. S. Shur and Jian-Qiang, “Terahertz sources and detectors using two-dimensional electronic fluid in high electron-mobility transistors,” *IEEE Transactions on Microwave Theory and Techniques*, vol. 48, no. 4 PART 2, pp. 750–756, 2000, doi: 10.1109/22.841969.

[185] X. Liu and M. Shur, “An Efficient TCAD Model for TeraFET Detectors operating in a large dynamic range,” *IEEE TRANSACTIONS ON TERAHERTZ SCIENCE AND TECHNOLOGY*, vol. 10, no. 1, pp. 15–20, 2020, doi: 10.1109/TTHZ.2019.2952248.

[186] Y. Bao, Z. Tang, H. Li, and Y. Zhang, “Computer vision and deep learning–based data anomaly detection method for structural health monitoring:,” *https://doi.org/10.1177/1475921718757405*, vol. 18, no. 2, pp. 401–421, Feb. 2018, doi: 10.1177/1475921718757405.

[187] D. Kwon, H. Kim, J. Kim, S. C. Suh, I. Kim, and K. J. Kim, “A survey of deep learning-based network anomaly detection,” *Cluster Computing*, vol. 22, no. 1, pp. 949–961, Jan. 2019, doi: 10.1007/S10586-017-1117-8/TABLES/2.

[188] Q. I. Mao *et al.*, “Convolutional neural network model based on terahertz imaging for integrated circuit defect detections,” *Optics Express, Vol. 28, Issue 4, pp. 5000-5012*, vol. 28, no. 4, pp. 5000–5012, Feb. 2020, doi: 10.1364/OE.384146.

[189] J. Yosinski, J. Clune, Y. Bengio, and H. Lipson, “How transferable are features in deep neural networks?,” *Advances in Neural Information Processing Systems*, vol. 27, 2014.

[190] S. L. Rumyantsev *et al.*, “Terahertz Beam Testing of Millimeter Wave Monolithic Integrated Circuits,” *IEEE Sensors Journal*, vol. 17, no. 17, pp. 5487–5491, Sep. 2017, doi: 10.1109/JSEN.2017.2725744.

[191] T. A. Elkhatib *et al.*, “Subwavelength detection of terahertz radiation using GaAs HEMTs,” in *Proceedings of IEEE Sensors*, 2009, pp. 1988–1990. doi: 10.1109/ICSENS.2009.5398312.

[192] T. L. Cocker *et al.*, “Terahertz Microscopy Down to the Atomic Scale,” in *International Conference on Infrared, Millimeter, and Terahertz Waves, IRMMW-THz*, Oct. 2018, vol. 2018-September. doi: 10.1109/IRMMW-THz.2018.8509936.

[193] T. L. Cocker *et al.*, “Sub-cycle terahertz microscopy down to the atomic scale.”

[194] K. Kawase, “Terahertz Imaging For Drug Detection And Large-Scale Integrated Circuit Inspection,” *Optics and Photonics News*, vol. 15, no. 10, p. 34, Oct. 2004, doi: 10.1364/opn.15.10.000034.

[195] S. J. Pan and Q. Yang, “A survey on transfer learning,” *IEEE Transactions on Knowledge and Data Engineering*, vol. 22, no. 10, pp. 1345–1359, 2010, doi: 10.1109/TKDE.2009.191.

[196] J. Donahue *et al.*, “DeCAF: A Deep Convolutional Activation Feature for Generic Visual Recognition.” PMLR, pp. 647–655, Jan. 27, 2014. Accessed: Feb. 13, 2022. [Online]. Available: https://proceedings.mlr.press/v32/donahue14.html

[197] N. Tajbakhsh *et al.*, “Convolutional Neural Networks for Medical Image Analysis: Full Training or Fine Tuning?,” *IEEE Transactions on Medical Imaging*, vol. 35, no. 5, pp. 1299–1312, May 2016, doi: 10.1109/TMI.2016.2535302.

[198] E. Cetinic, T. Lipic, and S. Grgic, “Fine-tuning Convolutional Neural Networks for fine art classification,” *Expert Systems with Applications*, vol. 114, pp. 107–118, Dec. 2018, doi: 10.1016/J.ESWA.2018.07.026.

[199] S. Shao, S. McAleer, R. Yan, and P. Baldi, “Highly Accurate Machine Fault Diagnosis Using Deep Transfer Learning,” *IEEE Transactions on Industrial Informatics*, vol. 15, no. 4, pp. 2446–2455, Apr. 2019, doi: 10.1109/TII.2018.2864759.

[200] N. Yu *et al.*, “Light propagation with phase discontinuities: Generalized laws of reflection and refraction,” *Science (1979)*, vol. 334, no. 6054, pp. 333–337, Oct. 2011, doi: 10.1126/SCIENCE.1210713/SUPPL_FILE/YU-SOM.PDF.

[201] N. I. Zheludev and Y. S. Kivshar, “From metamaterials to metadevices,” *Nature Materials 2012 11:11*, vol. 11, no. 11, pp. 917–924, Oct. 2012, doi: 10.1038/nmat3431.

[202] S. Chen, Z. Li, W. Liu, H. Cheng, and J. Tian, “Metasurfaces: From Single-Dimensional to Multidimensional Manipulation of Optical Waves with Metasurfaces (Adv. Mater. 16/2019),” *Advanced Materials*, vol. 31, no. 16, p. 1970118, Apr. 2019, doi: 10.1002/ADMA.201970118.

[203] A. M. Shaltout, V. M. Shalaev, and M. L. Brongersma, “Spatiotemporal light control with active metasurfaces,” *Science*, vol. 364, no. 6441, 2019, doi: 10.1126/SCIENCE.AAT3100.

[204] X. Zhu *et al.*, “A stretch-tunable plasmonic structure with a polarization-dependent response,” *Optics Express, Vol. 20, Issue 5, pp. 5237-5242*, vol. 20, no. 5, pp. 5237–5242, Feb. 2012, doi: 10.1364/OE.20.005237.

[205] S. Maier, “Plasmonics - Towards Subwavelength Optical Devices,” *Current Nanoscience*, vol. 1, no. 1, pp. 17–22, Mar. 2006, doi: 10.2174/1573413052953165.

[206] K. Yao and Y. Liu, “Plasmonic metamaterials,” *Nanotechnology Reviews*, vol. 3, no. 2. Walter de Gruyter GmbH, pp. 177–210, Apr. 01, 2014. doi: 10.1515/ntrev-2012-0071.

[207] G. v. Naik and A. Boltasseva, “A comparative study of semiconductor-based plasmonic metamaterials,” *Metamaterials*, vol. 5, no. 1, pp. 1–7, Apr. 2011, doi: 10.1016/j.metmat.2010.11.001.

[208] S. Singamaneni *et al.*, “Nondestructive in situ identification of crystal orientation of anisotropic zno nanostructures,” *ACS Nano*, vol. 3, no. 9, pp. 2593–2600, Sep. 2009, doi: 10.1021/nn900687g.

[209] A. Boltasseva and H. A. Atwater, “Low-loss plasmonic metamaterials,” *Science*, vol. 331, no. 6015. American Association for the Advancement of Science, pp. 290–291, Jan. 21, 2011. doi: 10.1126/science.1198258.

[210] I. I. Smolyaninov, J. Elliott, A. v. Zayats, and C. C. Davis, “Far-field optical microscopy with a nanometer-scale resolution based on the in-plane image magnification by surface plasmon polaritons,” *Physical Review Letters*, vol. 94, no. 5, p. 057401, Feb. 2005, doi: 10.1103/PhysRevLett.94.057401.

[211] A. N. Grigorenko *et al.*, “Nanofabricated media with negative permeability at visible frequencies,” *Nature*, vol. 438, no. 7066, pp. 335–338, Nov. 2005, doi: 10.1038/nature04242.

[212] G. Dolling, M. Wegener, C. M. Soukoulis, and S. Linden, “Negative-index metamaterial at 780 nm wavelength,” *Optics Letters*, vol. 32, no. 1, p. 53, Jan. 2007, doi: 10.1364/ol.32.000053.

[213] V. G. Kravets *et al.*, “Singular phase nano-optics in plasmonic metamaterials for label-free single-molecule detection,” *Nature Materials*, vol. 12, no. 4, pp. 304–309, Apr. 2013, doi: 10.1038/nmat3537.

[214] Y. Y. Lee, R. M. Kim, S. W. Im, M. Balamurugan, and K. T. Nam, “Plasmonic metamaterials for chiral sensing applications,” *Nanoscale*, vol. 12, no. 1. Royal Society of Chemistry, pp. 58–66, Jan. 07, 2020. doi: 10.1039/c9nr08433a.

[215] V. v. Yakovlev *et al.*, “Ultrasensitive Non-Resonant Detection of Ultrasound with Plasmonic Metamaterials,” *Advanced Materials*, vol. 25, no. 16, pp. 2351–2356, Apr. 2013, doi: 10.1002/adma.201300314.

[216] H. Hajian, A. Ghobadi, B. Butun, and E. Ozbay, “Active metamaterial nearly perfect light absorbers: a review [Invited],” *Journal of the Optical Society of America B*, vol. 36, no. 8, p. F131, Aug. 2019, doi: 10.1364/josab.36.00f131.

[217] A. Vora, J. Gwamuri, N. Pala, A. Kulkarni, J. M. Pearce, and D. O. Güney, “Exchanging ohmic losses in metamaterial absorbers with useful optical absorption for photovoltaics,” *Scientific Reports*, vol. 4, no. 1, pp. 1–13, May 2014, doi: 10.1038/srep04901.

[218] J. Y. Ou, E. Plum, J. Zhang, and N. I. Zheludev, “An electromechanically reconfigurable plasmonic metamaterial operating in the near-infrared,” *Nature Nanotechnology*, vol. 8, no. 4, pp. 252–255, Mar. 2013, doi: 10.1038/nnano.2013.25.

[219] A. Kuzyk, R. Schreiber, H. Zhang, A. O. Govorov, T. Liedl, and N. Liu, “Reconfigurable 3D plasmonic metamolecules,” *Nature Materials*, vol. 13, no. 9, pp. 862–866, Jul. 2014, doi: 10.1038/nmat4031.

[220] N. Papasimakis, V. A. Fedotov, V. Savinov, T. A. Raybould, and N. I. Zheludev, “Electromagnetic toroidal excitations in matter and free space,” *Nature Materials*, vol. 15, no. 3, pp. 263–271, Feb. 2016, doi: 10.1038/nmat4563.

[221] T. Kaelberer, V. A. Fedotov, N. Papasimakis, D. P. Tsai, and N. I. Zheludev, “Toroidal dipolar response in a metamaterial,” *Science (1979)*, vol. 330, no. 6010, pp. 1510–1512, Dec. 2010, doi: 10.1126/science.1197172.

[222] M. Gupta *et al.*, “Sharp Toroidal Resonances in Planar Terahertz Metasurfaces,” *Advanced Materials*, vol. 28, no. 37, pp. 8206–8211, Oct. 2016, doi: 10.1002/adma.201601611.

[223] B. Gerislioglu, A. Ahmadivand, and N. Pala, “Tunable plasmonic toroidal terahertz metamodulator,” *Physical Review B*, vol. 97, no. 16, p. 161405, Apr. 2018, doi: 10.1103/PhysRevB.97.161405.

[224] E. A. Nanni, S. K. Jawla, M. A. Shapiro, P. P. Woskov, and R. J. Temkin, “Low-loss transmission lines for high-power terahertz radiation,” *Journal of Infrared, Millimeter, and Terahertz Waves*, vol. 33, no. 7, pp. 695–714, Jul. 2012, doi: 10.1007/s10762-012-9870-5.

[225] Y. W. Huang, W. T. Chen, P. C. Wu, V. A. Fedotov, N. I. Zheludev, and D. P. Tsai, “Toroidal lasing spaser,” *Scientific Reports*, vol. 3, no. 1, pp. 1–4, Feb. 2013, doi: 10.1038/srep01237.

[226] Y.-W. Huang *et al.*, “Design of plasmonic toroidal metamaterials at optical frequencies,” *Optics Express*, vol. 20, no. 2, p. 1760, Jan. 2012, doi: 10.1364/oe.20.001760.

[227] S. Han, M. Gupta, L. Cong, Y. K. Srivastava, and R. Singh, “Toroidal and magnetic Fano resonances in planar THz metamaterials,” *Journal of Applied Physics*, vol. 122, no. 11, p. 113105, Sep. 2017, doi: 10.1063/1.5001246.

[228] M. Gupta and R. Singh, “Toroidal versus Fano Resonances in High Q planar THz Metamaterials,” *Advanced Optical Materials*, vol. 4, no. 12, pp. 2119–2125, Dec. 2016, doi: 10.1002/adom.201600553.

[229] A. Ahmadivand and B. Gerislioglu, “Large-modulation-depth polarization-sensitive plasmonic toroidal terahertz metamaterial,” *IEEE Photonics Technology Letters*, vol. 29, no. 21, pp. 1860–1863, Nov. 2017, doi: 10.1109/LPT.2017.2754339.

[230] P. C. Wu *et al.*, “Three-dimensional metamaterials: from split ring resonator to toroidal metamolecule,” in *Plasmonics: Metallic Nanostructures and Their Optical Properties XII*, Sep. 2014, vol. 9163, p. 91630M. doi: 10.1117/12.2061340.

[231] Z. Dong *et al.*, “Optical toroidal dipolar response by an asymmetric double-bar metamaterial Optical toroidal dipolar response by an asymmetric double-bar metamaterial,” vol. 144105, no. December 2018, pp. 1–5, 2017, doi: 10.1063/1.4757613.

[232] Q. Zhang, J. J. Xiao, and S. L. Wang, “Optical characteristics associated with magnetic resonance in toroidal metamaterials of vertically coupled plasmonic nanodisks,” *Journal of the Optical Society of America B*, vol. 31, no. 5, p. 1103, May 2014, doi: 10.1364/josab.31.001103.

[233] J. Li, Y. Zhang, R. Jin, Q. Wang, Q. Chen, and Z. Dong, “Excitation of plasmon toroidal mode at optical frequencies by angle-resolved reflection,” *Optics Letters*, vol. 39, no. 23, p. 6683, Dec. 2014, doi: 10.1364/ol.39.006683.

[234] W. Liu, J. Zhang, and A. E. Miroshnichenko, “Toroidal dipole-induced transparency in core-shell nanoparticles,” *Laser & Photonics Reviews*, vol. 9, no. 5, pp. 564–570, Sep. 2015, doi: 10.1002/lpor.201500102.

[235] B. Ögüt, N. Talebi, R. Vogelgesang, W. Sigle, and P. A. van Aken, “Toroidal plasmonic eigenmodes in oligomer nanocavities for the visible,” *Nano Letters*, vol. 12, no. 10, pp. 5239–5244, Oct. 2012, doi: 10.1021/nl302418n.

[236] W. Liu, J. Zhang, B. Lei, H. Hu, and A. E. Miroshnichenko, “Invisible nanowires with interfering electric and toroidal dipoles,” *Optics Letters*, vol. 40, no. 10, p. 2293, May 2015, doi: 10.1364/ol.40.002293.

[237] N. Akter, M. Karabiyik, and N. Pala, “Hybrid Toroidal Modes in Planar Core-Shell Metamaterial Structures,” *31st Annual Conference of the IEEE Photonics Society, IPC 2018*, Nov. 2018, doi: 10.1109/IPCON.2018.8527265.

[238] M. Gupta, Y. K. Srivastava, and R. Singh, “A Toroidal Metamaterial Switch,” *Advanced Materials*, vol. 30, no. 4, p. 1704845, Jan. 2018, doi: 10.1002/adma.201704845.

[239] V. E. Rogalin, I. A. Kaplunov, and G. I. Kropotov, “Optical Materials for the THz Range,” *Optics and Spectroscopy*, vol. 125, no. 6, pp. 1053–1064, Dec. 2018, doi: 10.1134/S0030400X18120172.

[240] M. A. Ordal, R. J. Bell, R. W. Alexander, L. L. Long, and M. R. Querry, “Optical properties of Au, Ni, and Pb at submillimeter wavelengths,” *Applied Optics*, vol. 26, no. 4, p. 744, Feb. 1987, doi: 10.1364/ao.26.000744.

[241] A. Ahmadivand *et al.*, “Extreme sensitive metasensor for targeted biomarkers identification using colloidal nanoparticles-integrated plasmonic unit cells,” *Biomedical Optics Express*, vol. 9, no. 2, p. 373, Feb. 2018, doi: 10.1364/boe.9.000373.

[242] X. Chen and W. Fan, “Study of the interaction between graphene and planar terahertz metamaterial with toroidal dipolar resonance,” *Optics Letters*, vol. 42, no. 10, p. 2034, May 2017, doi: 10.1364/ol.42.002034.

[243] E. Prodan, C. Radloff, N. J. Halas, and P. Nordlander, “A Hybridization Model for the Plasmon Response of Complex Nanostructures,” *Science (1979)*, vol. 302, no. 5644, pp. 419–422, Oct. 2003, doi: 10.1126/science.1089171.

[244] I. M. Pryce, K. Aydin, Y. A. Kelaita, R. M. Briggs, and H. A. Atwater, “Highly strained compliant optical metamaterials with large frequency tunability,” *Nano Letters*, vol. 10, no. 10, pp. 4222–4227, Oct. 2010, doi: 10.1021/NL102684X/SUPPL_FILE/NL102684X_SI_001.PDF.

[245] I. E. Khodasevych *et al.*, “Elastomeric silicone substrates for terahertz fishnet metamaterials,” *Applied Physics Letters*, vol. 100, no. 6, p. 061101, Feb. 2012, doi: 10.1063/1.3665180.

[246] S. Khodakarimi, M. H. Hekhmatshoar, M. Nasiri, M. Khaleghi Moghaddam, and F. Abbasi, “Effects of process and post-process treatments on the electrical conductivity of the PEDOT:PSS films,” *Journal of Materials Science: Materials in Electronics*, vol. 27, no. 2, pp. 1278–1285, Feb. 2016, doi: 10.1007/S10854-015-3886-2/FIGURES/8.

[247] M. Vosgueritchian, D. J. Lipomi, and Z. Bao, “Highly Conductive and Transparent PEDOT:PSS Films with a Fluorosurfactant for Stretchable and Flexible Transparent Electrodes,” *Advanced Functional Materials*, vol. 22, no. 2, pp. 421–428, Jan. 2012, doi: 10.1002/ADFM.201101775.

[248] W. F. Quirós-Solano, N. Gaio, C. Silvestri, G. Pandraud, and P. M. Sarro, “PEDOT:PSS: A Conductive and Flexible Polymer for Sensor Integration in Organ-on-Chip Platforms,” *Procedia Engineering*, vol. 168, pp. 1184–1187, Jan. 2016, doi: 10.1016/J.PROENG.2016.11.401.

[249] A. M. Melo, A. L. Gobbi, M. H. O. Piazzetta, and A. M. P. A. da Silva, “Cross-Shaped Terahertz Metal Mesh Filters: Historical Review and Results,” *Advances in Optical Technologies*, vol. 2012, p. 12, 2012, doi: 10.1155/2012/530512.

[250] D. Zhai, Y. Yang, Z. Geng, B. Cui, and R. Zhao, “A High-Selectivity THz Filter Based on a Flexible Polyimide Film,” *IEEE Transactions on Terahertz Science and Technology*, vol. 8, no. 6, pp. 719–724, Nov. 2018, doi: 10.1109/TTHZ.2018.2872414.

[251] A. Khalid, D. R. S. Cumming, T. D. Drysdale, and Y. Ma, “Direct fabrication of terahertz optical devices on low-absorption polymer substrates,” *Optics Letters, Vol. 34, Issue 10, pp. 1555-1557*, vol. 34, no. 10, pp. 1555–1557, May 2009, doi: 10.1364/OL.34.001555.

[252] M. Zhuldybina *et al.*, “Mass-production of terahertz devices,” pp. 1–2, Oct. 2021, doi: 10.1109/IRMMW-THZ50926.2021.9566995.

[253] H. S. Bark, K. H. Jang, K. Lee, Y. U. Jeong, and T. I. Jeon, “THz guided-mode resonance notch filter with variable filtering strength,” *Scientific Reports 2021 11:1*, vol. 11, no. 1, pp. 1–10, Jan. 2021, doi: 10.1038/s41598-020-80134-2.

[254] H. Tao *et al.*, “Performance enhancement of terahertz metamaterials on ultrathin substrates for sensing applications,” *Applied Physics Letters*, vol. 97, no. 26, p. 261909, Dec. 2010, doi: 10.1063/1.3533367.

[255] Z. Geng, X. Guo, Y. Cao, Y. Yang, and H. Chen, “Flexible, low-loss and large area metamaterials with high Q value,” *Microelectronic Engineering*, vol. 135, pp. 23–27, Mar. 2015, doi: 10.1016/J.MEE.2015.02.045.

[256] H. Tao *et al.*, “Highly flexible wide angle of incidence terahertz metamaterial absorber: Design, fabrication, and characterization,” *Physical Review B - Condensed Matter and Materials Physics*, vol. 78, no. 24, p. 241103, Dec. 2008, doi: 10.1103/PHYSREVB.78.241103/FIGURES/4/MEDIUM.

[257] M. Choi *et al.*, “A terahertz metamaterial with unnaturally high refractive index,” *Nature 2011 470:7334*, vol. 470, no. 7334, pp. 369–373, Feb. 2011, doi: 10.1038/nature09776.

[258] Y. Shan *et al.*, “Ultrathin flexible dual band terahertz absorber,” *Optics Communications*, vol. 350, pp. 63–70, Sep. 2015, doi: 10.1016/J.OPTCOM.2015.03.072.

[259] A. Lecavelier Des Etangs-Levallois *et al.*, “A converging route towards very high frequency, mechanically flexible, and performance stable integrated electronics,” *Journal of Applied Physics*, vol. 113, no. 15, p. 153701, Apr. 2013, doi: 10.1063/1.4801803.

[260] S. R. Forrest, “The path to ubiquitous and low-cost organic electronic appliances on plastic,” *Nature 2004 428:6986*, vol. 428, no. 6986, pp. 911–918, Apr. 2004, doi: 10.1038/nature02498.

[261] F. C. Chen, M. K. Chuang, S. C. Chien, J. H. Fang, and C. W. Chu, “Flexible polymer solar cells prepared using hard stamps for the direct transfer printing of polymer blends with self-organized interfaces,” *Journal of Materials Chemistry*, vol. 21, no. 30, pp. 11378–11382, Jul. 2011, doi: 10.1039/C1JM11336D.

[262] L. Polavarapu and L. M. Liz-Marzán, “Towards low-cost flexible substrates for nanoplasmonic sensing,” *Physical Chemistry Chemical Physics*, vol. 15, no. 15, pp. 5288–5300, Mar. 2013, doi: 10.1039/C2CP43642F.

[263] D. Zhai, R. Zhao, Z. Geng, B. Cui, and Y. Yang, “A high-selectivity THz band-stop filter based on a flexible polyimide film,” *https://doi.org/10.1117/12.2500900*, vol. 10826, pp. 189–195, Nov. 2018, doi: 10.1117/12.2500900.

[264] S. Seok and J. Kim, “Design, fabrication, and characterization of a wideband 60 ghz bandpass filter based on a flexible permx polymer substrate,” *IEEE Transactions on Components, Packaging and Manufacturing Technology*, vol. 3, no. 8, pp. 1384–1389, 2013, doi: 10.1109/TCPMT.2013.2240040.

[265] S. Aksu *et al.*, “Flexible Plasmonics on Unconventional and Nonplanar Substrates,” *Advanced Materials*, vol. 23, no. 38, pp. 4422–4430, Oct. 2011, doi: 10.1002/ADMA.201102430.

[266] H. Tao *et al.*, “Terahertz metamaterials on free-standing highly-flexible polyimide substrates,” *Journal of Physics D: Applied Physics*, vol. 41, no. 23, p. 232004, Nov. 2008, doi: 10.1088/0022-3727/41/23/232004.

[267] A. Mitchell *et al.*, “Flexible terahertz metamaterials for dual-axis strain sensing,” *Optics Letters, Vol. 38, Issue 12, pp. 2104-2106*, vol. 38, no. 12, pp. 2104–2106, Jun. 2013, doi: 10.1364/OL.38.002104.

[268] S. Aksu *et al.*, “Flexible Plasmonics on Unconventional and Nonplanar Substrates,” *Advanced Materials*, vol. 23, no. 38, pp. 4422–4430, Oct. 2011, doi: 10.1002/ADMA.201102430.

[269] E. Ekmekci and G. Turhan-Sayan, “Metamaterial sensor applications based on broadside-coupled SRR and V-Shaped resonator structures,” *IEEE Antennas and Propagation Society, AP-S International Symposium (Digest)*, pp. 1170–1172, 2011, doi: 10.1109/APS.2011.5996492.

[270] G. Kenanakis *et al.*, “Microwave and THz sensing using slab-pair-based metamaterials,” *Physica B: Condensed Matter*, vol. 407, no. 20, pp. 4070–4074, Oct. 2012, doi: 10.1016/J.PHYSB.2012.04.050.

[271] O. Paul *et al.*, “Highly Selective Terahertz Bandpass Filters Based on Trapped Mode Excitation,” *Optics Express, Vol. 17, Issue 21, pp. 18590-18595*, vol. 17, no. 21, pp. 18590–18595, Oct. 2009, doi: 10.1364/OE.17.018590.

[272] Y. Lin *et al.*, “Free-standing double-layer terahertz band-pass filters fabricated by femtosecond laser micro-machining,” *Optics Express, Vol. 25, Issue 21, pp. 25125-25134*, vol. 25, no. 21, pp. 25125–25134, Oct. 2017, doi: 10.1364/OE.25.025125.

[273] A. E. Lange, D. D. Nolte, and P. L. Richards, “Far-infrared dichroic bandpass filters,” *Applied Optics, Vol. 24, Issue 10, pp. 1541-1545*, vol. 24, no. 10, pp. 1541–1545, May 1985, doi: 10.1364/AO.24.001541.

[274] A. Ahmadivand *et al.*, “Rapid Detection of Infectious Envelope Proteins by Magnetoplasmonic Toroidal Metasensors,” *ACS Sensors*, vol. 2, no. 9, pp. 1359–1368, Sep. 2017, doi: 10.1021/ACSSENSORS.7B00478.

[275] “Terahertz Technology for the Identification of the COVID-19,” 2020. Accessed: Jun. 22, 2021. [Online]. Available: www.tera.group

[276] A. Ahmadivand, B. Gerislioglu, Z. Ramezani, A. Kaushik, P. Manickam, and S. A. Ghoreishi, “Functionalized terahertz plasmonic metasensors: Femtomolar-level

detection of SARS-CoV-2 spike proteins," *Biosensors and Bioelectronics*, vol. 177, p. 112971, Apr. 2021, doi: 10.1016/j.bios.2021.112971.

[277] N. Akter, M. M. Hasan, and N. Pala, "A Review of THz Technologies for Rapid Sensing and Detection of Viruses including SARS-CoV-2," *Biosensors 2021, Vol. 11, Page 349*, vol. 11, no. 10, p. 349, Sep. 2021, doi: 10.3390/BIOS11100349.

[278] J. H. Son, "Terahertz bio-sensing techniques," *Handbook of Terahertz Technology for Imaging, Sensing and Communications*, pp. 217–230, Jan. 2013, doi: 10.1533/9780857096494.2.217.

[279] M. Nagel, M. Först, and H. Kurz, "THz biosensing devices: fundamentals and technology," *Journal of Physics: Condensed Matter*, vol. 18, no. 18, p. S601, Apr. 2006, doi: 10.1088/0953-8984/18/18/S07.

VITA

NAZNIN AKTER
Email: nakte001@fiu.edu
Phone: +1-786 867 5858
LinkedIn: https://www.linkedin.com/in/nazninpmp/

2017-2022 PhD. Electrical and Computer Engineering
Florida International University
Miami, Florida, USA

2017-2020 M.Sc. Electrical Engineering
Florida International University
Miami, Florida, USA

2012-2014 M.Sc. Applied Physics, Electronics & Communication Engineering
University of Dhaka
Dhaka, Bangladesh

2007-2012 B.Sc. Applied Physics, Electronics & Communication Engineering
University of Dhaka
Dhaka, Bangladesh

PUBLICATIONS

1. N. Akter, MM.Hasan, and N. Pala. "A Review of THz Technologies for Rapid Sensing and Detection of Viruses including SARS-CoV-2." Biosensors 11, no. 10 (2021): 349.
2. N. Akter, M. R. Siddiquee, M. Shur, and N. Pala, "AI-Powered THz VLSI Testing Technology for Ensuring Hardware Security and Reliability", IEEE Access, (April 2021) DOI: 10.1109/ACCESS.2021.3075429
3. N. Akter, A. Legacy, F. Alam, N. Pala, "Hybrid Toroidal Resonance Response in Planar Core-Shell THz Metasurfaces", Plasmonics (March 2021) DOI: 10.1007/s11468-021-01427-4
4. N. Akter, J. J. Becerril-Gonzalez, M. Karabiyik, F. Alam, N. Pala, G. Oskam, O. Arés-Muzio, "FDTD Modeling of Sputtered Mo-Al2O3 Nanocomposites", Solar Energy Materials & Solar Cells, 225 111027 (June 2021) DOI: 10.1016/j.solmat.2021.111027
5. F. Alam, S. Roy Choudhury, A. H Jalal, Y. Umasankar, S. Forouzanfar, N. Akter, S. Bhansali, and N. Pala, "Lactate Biosensing: The Emerging Point-of-Care and Personal Health Monitoring" Biosensors and Bioelectronics, 117, 818-829 (2018) DOI: 10.1016/j.bios.2018.06.054
6. N. Akter, N. Pala, W. Knap, and M. Shur, "THz Plasma Field Effect Transistor Detectors", Fundamentals of Terahertz Devices and Applications, First Edition.

Edited by Dimitris Pavlidis. Published 2021 by John Wiley & Sons, Ltd, ISBN: 978-1-119-46071-8

7. N. Akter, MM. Hasan, JJ Becerril-Gonzalez, G Oskam, Nezih Pala, and O Ares-Muzio, “Modeling of Sputtered Mo-Al2O3 Nanocomposites Using a Combination of FDTD Method and Maxwell-Garnett Approximation”, IEEE NMDC 2021, 12-15 December 2021, Vancouver, BC, Canada.
8. N. Akter, M. Karabiyik, A. Wright, M. Shur, N. Pala, “AI Powered THz Testing Technology for Ensuring Hardware Cybersecurity”, 2020 IEEE Research and Applications of Photonics in Defense Conference (RAPID), 10 - 12 August 2020, DOI: 10.1109/RAPID49481.2020.9195662
9. N. Akter, M. Karabiyik, M. Shur, J. Suarez, N. Pala, “AI Powered THz VLSI Testing Technology”, 29th North Atlantic Test Workshop, Albany, NY, June 17-24, 2020, DOI: 10.1109/NATW49237.2020.9153077
10. N. Akter, JJ Becerril-Gonzalez, G Oskam, Nezih Pala, and O Ares-Muzio, “Numerical and Experimental Study of Sputtered Mo-Al2O3 Nano Composites for Photothermal Energy Harvesting” 20th International Conference on Numerical Simulation of Optoelectronic Devices (NUSOD 2020).
11. N. Akter, M. Karabiyik, N. Pala, “Highly Tunable, Flexible and Stretchable Frequency Selective Surface-based THz Bandpass Filter” IEEE Photonics Conference, 29 September-3 October 2019, San Antonio, TX, DOI: 10.1109/IPCon.2019.8908502
12. M. Karabiyik, N. Akter, N. Pala, B. Imran Akca, “Raman Signal Amplification in Photonic Crystal Microring Resonators” IEEE Photonics Conference (IPC), 29 September-3 October 2019, San Antonio, TX, USA, pp. 1-2. DOI: 10.1109/IPCon.2019.8908298
13. N. Akter, M. Karabiyik, N. Pala, “On-Chip Spectrometer Using Cascaded Echelle Gratings and Arrayed Waveguide Gratings”, IEEE Research and Applications of Photonics in Defense (RAPID), 19-21 August 2019, Miramar Beach, FL. DOI: 10.1109/RAPID.2019.8864430
14. N. Akter, M. Karabiyik, N. Pala, “Hybrid Toroidal Modes in Planar Core-Shell Metamaterial Structures”, IEEE Photonics Conference (IPC), 30 September - 4 October 2018, Reston, VA, USA, DOI: 10.1109/IPCon.2018.8527265
15. F. Alam, S. Forouzanfar, M. Karabiyik, N. Akter, R. Matos, and N. Pala, “Zinc Oxide Nanostructure Based Noninvasive and Continuous Sweat pH Sensing and Monitoring Platform” ECS Meeting Abstracts